A Computational Study of Cortical Spreading Depression

A DISSERTATION
SUBMITTED TO THE FACULTY OF THE GRADUATE SCHOOL
OF THE UNIVERSITY OF MINNESOTA
BY

Rosemary Anne O'Connell

IN PARTIAL FULFILLMENT OF THE REQUIREMENTS
FOR THE DEGREE OF
DOCTOR OF PHILOSOPHY

YOICHIRO MORI

May, 2016

Acknowledgements

I would like to thank many people for their support and guidance over the course of my time as a graduate student. First and foremost, thank you to Yoichiro Mori for all of your advice and assistance over the last several years. In addition, thank you to Dick McGehee and Mitch Luskin for helping me figure out where I wanted to focus my research, and to all of the professors and fellow students who have helped me along the way.

Dedication

For my parents, who have provided endless support and encouragement throughout my life, and my husband, who has done the same for as long as he has known me.

Abstract

Spreading depression (SD) is a pathological phenomenon of the central nervous system in which normal cellular function is disrupted by a prolonged depolarization, which spreads spatially at a rate of several millimeters per minute. SD is connected to a number of medical conditions, including migraine with aura, traumatic brain injury, and epilepsy. This thesis presents a general framework for modeling spreading depression as a multiphasic continuum that is based on fully incorporating biophysical principles, including electrodiffusion and osmosis. The generality of the model allows us to explore how many different aspects of the physiology may impact the system, which we do through four specific models. In particular, we explore the effects of fluid flow within the extracellular space, adding a glial compartment, and including two neuronal compartments in one spatial dimension. In addition, we explore features of SD propagation in two spatial dimensions. In each of these four specific models, we vary several different parameters to understand the role they have in the initiation and propagation of SD. We find that many aspects of the system affect the speed of propagation and that glial cells play a significant role in the extracellular potential variation seen during SD. Additionally, some parameters affect the relative timing of the various changes that take place during SD.

Contents

List of Tables

List of Figures

Chapter 1

Introduction

Cortical spreading depression (SD) is a phenomenon in the central nervous system during which cells experience a prolonged depolarization, accompanied by a significant change in ionic concentrations and cell swelling [1, 2, 3], which spreads through the brain spatially at rates of approximately 2 to 7 mm/min. SD is recognized as the underlying physiological mechanism of migraine aura [4, 5, 6, 7] and has been shown to be connected to epilepsy, traumatic brain injury, stroke, and cerebral ischemia [1, 8]. Improving our understanding of the mechanisms of SD will improve our understanding of these conditions as well as improve our overall understanding of the central nervous system through insight into the control of the cellular environment [1, 9].

SD was first documented by Leão in 1944, who observed a "spreading depression of activity", a reduction in normal electrical activity which spread slowly and recovery from which took several minutes [10]. Leão further reported a slow voltage variation in the extracellular space of 7 to 15 mV, also lasting several minutes, which is now commonly referred to as the DC shift [11]. Since these initial reports, SD has been frequently studied, both experimentally and theoretically, as summarized in numerous reviews [1, 2, 6, 9, 12, 13, 14, 15, 16, 17, 18, 19, 20]. Chapter 2 (Background) provides a discussion of some of these results.

In spite of these many studies, a full understanding of the mechanisms of SD remains elusive. The triggering of SD under experimental conditions is fairly well understood, but the manner in which it spreads remains unclear. The involvement of many different biophysical behaviors which occur on different time scales likely contributes to this: ion channel properties change quickly while the actual propagation is slow. We present a general model of SD that incorporates ion channel gating, electrodiffusion, and osmotic water flow, and allows for the inclusion of features such as glial K^+ buffering and cell overlap according to biophysical principles. The model is designed to obey conservation laws in one, two, or three spatial dimensions and is detailed in Chapter 3 (Model).

In order to study the propagation of SD, we simulated the model in one and two spatial dimensions while incorporating different cell types and ion channels, exploring the effects of different parameters in each variation of the model. Chapter 4 (Incorporating Fluid Flow) examines the effects of including intracompartmental fluid flow, examining several values for the hydraulic permeability and membrane stiffness. The role of glial cells is examined in Chapter 5. Simulations were run with different values of the glial Na^+/K^+ ATPase strength, K^+ channel density, and gap-junctional coupling strength in order to gain a better understanding of the effects of glial K^+ buffering. Chapter 6 (NMDA Receptors and Cell Overlap) explores how the NMDA receptor and glutamate contribute to SD, looking at different values of the NMDA receptor permeability and glutamate reabsorption as well as the permeability of the persistent Na^+ channel and including two neuronal compartments that overlap. Chapter 7 (Two-Dimensional Results) provides the results of simulations in two spatial dimensions exploring the effects of glial gap junctional coupling and SD being triggered simultaneously at multiple points. Chapter 8 (Conclusion and Discussion) summarizes the insight our model and simulations provide to the understanding of SD.

Chapter 2

Background

The terms spreading depression and spreading depolarization are frequently used interchangeably, but are sometimes used to refer to slightly different phenomena [19]. Spreading depression refers to the suppression of spontaneous electrical activity in neurons seen by Leão [10], whereas spreading depolarization refers to a sustained positive shift in the membrane potential which has been widely observed more recently. When neuronal activity is normal, such a depolarization prevents spontaneous electrical activity, and thus the two coincide. In certain situations, however, depression of neuronal activity may occur prior to the depolarization due to other factors, including hypoxia or ischemia, and therefore the two have historically been identified as distinct phenomena. Recent research and modeling efforts have indicated that the two are extremes of a continuum of related behavior [15, 21, 22], and we will not distinguish between them, using SD as an abbreviation for both.

2.1 Features of Spreading Depression

Following Leão's initial observations of the depression of activity [10], many features of SD have been identified. SD features a rapid depolarization of both neurons and glia, with the membrane potential plateauing for a time. This depolarization is followed

by either a recovery to the resting membrane potential or by cell death. Coinciding with this is a massive redistribution of ions as the transmembrane ion concentration gradients break down. The change in concentrations occurs within seconds and lasts for at least 30 seconds. As a result of the change in concentrations, the cells' overall osmolality changes [23]. In turn, this leads to cell swelling, with water flowing into the cell due to osmotic pressure. Swelling occurs in the neuronal somata and "beading" in the dendrites [24], and the extracellular space decreases from approximately 20% of the volume to approximately 5% [25]. A significant release of neurotransmitters also occurs with the cells' depolarization [26].

In addition to the membrane potential shift, the extracellular space shows a slow voltage variation termed the DC shift. The DC shift is characterized by a decrease in the extracellular voltage that lasts for some time, typically followed by a "positive tail", an overshoot to slightly above the resting voltage before gradually decreasing back to the normal potential. The DC shift is sometimes also preceded by a brief positive shift. The magnitude of the DC shift varies significantly between experiments, with some studies showing a negative variation of 5 to 15 mV [11, 27], while others show an amplitude of 15 to 40 mV [28, 29].

As the original discovery of SD was electrical in nature, a great deal of research has gone into the characteristics of both the DC shift and the depolarization itself. In the 1970s, Somjen [30] hypothesized that sustained extracellular potential shifts were likely heavily influenced by glial cells. Sugaya et al. [29] studied neuronal and glial depolarizations during SD and found that the glial depolarization coincided closely with the DC shift, whereas the neuronal depolarization only sometimes occurred at the same time; at other times, the neuronal depolarization occurred 30 seconds after the DC shift. The shape of the DC shift itself is dependent upon where the recording is and also changes after repeated waves of SD, as shown by Herreras and Somjen [28]. Specifically, they found that the DC shift in the hippocampus had a larger magnitude and longer duration in the stratum radiatum than in the stratum pyramidale, as well

as occurring several seconds earlier in the stratum radiatum. The DC shift in the stratum radiatum also featured a saddle shape with a second, larger and sustained shift, while the DC shift in the stratum pyramidale featured only a single hump that lasted roughly for the period of relative positivity during the saddle in the stratum radiatium. As successive waves of SD happened, the second hump of the DC shift in the stratum radiatum lasted progressively longer, and the DC shift in the stratum pyramidale eventually acquired a single sharp spike after the main event. These changes happened whether the repeated waves of SD were a result of continuous elevation of extracellular K^+ or repeated provoking by brief periods of high K^+ or by electric stimuli in 5 to 20 minute intervals. Blocking NMDA receptors eliminated the second hump in the stratum radiatum locally, an effect that was reversed upon removal of the antagonist. Similarly, the membrane potential changes are dependent on the part of the cell [31], as the membrane potential begins to recover in the soma when the extracellular potential in the stratum pyramidale returns to normal, whereas the dendrites remain depolarized for the extent of the DC shift in the stratum radiatum.

SD can be initiated by a wide range of triggers. Dreier and Reifurth [21] divide these triggers into two types: direct triggers, which cause depolarization by activating sodium or calcium channels, and indirect triggers, which inhibit the Na^+/K^+ ATPase. Examples of direct triggers include glutamate and potassium. Indirect triggers include ouabain, hypoxia, and ischemia, as well as mutations in the ATP1A2 Na^+/K^+ ATPase $\alpha 2$ subunit that have been associated with familial hemiplegic migraine [32, 33].

Several theories have been proposed to explain the propagation of SD. Propagation occurs at a rate of several millimeters per minute, a slow spreading that is indicative of a diffusive mechanism. Grafstein's hypothesis, the first theory, was that the dramatic increase in extracellular potassium was an integral part of the propagation mechanism [34]. Van Harreveld proposed that glutamate, rather than potassium, was a key component [35], and later proposed the dual hypothesis, in which both potassium and glutamate could cause propagation [36]. Several others have proposed that propagation occurs

through gap junctions [37, 38].

Investigations have been made into several different possible mechanisms. Basarsky et al. [39] studied the role of calcium waves in glia. They induced SD using ouabain, elevated extracellular K^+, and electrical stimulation, and found that, while calcium waves propagated several seconds ahead of the SD wave, removing extracellular calcium did not stop either initiation or propagation. Dietz, Weiss, and Shuttleworth examined the effect of Zn^{2+} and found that Zn^{2+} chelation blocked SD induced by ouabain or oxygen and glucose deprivation, while having no effect on SD induced by elevated extracellular K^+. Glutamate's role has been narrowed down to its interactions with the NMDA receptor, as studies have shown that NMDA receptor antagonists will block SD but antagonists of other glutamate receptors have no effect [27, 40, 41].

Studies concerning the involvement of gap junctions have had a variety of results, with some implicating gap junctions as necessary and others suggesting they have an inhibitory role. Nedergaard et al. [42] found that several gap junction inhibitors, including octanol, halothane, and heptanol, blocked SD in chicken retina, both decreasing the velocity of propagation and reducing the size of the region affected. The gap junction blocker tonabersat has also been shown to reduce the number and duration of SD occurrences [43]. On the other hand, Martins-Ferreira and Ribeiro [44] found that low doses of octanol and heptanol increased the velocity, while higher doses blocked SD. Theis et al. [45] looked specifically at the involvement of connexin43, which is prevalent in astrocytes in the central nervous system. Deletion or loss of expression of connexin43 caused an increase in propagation speed, as well as a decrease in the magnitude of the DC shift. Tamura et al. [46] looked at the effect of a different gap junction blocker, carbenoxolone, and found that it caused an increase in the number of occurrences of SD and in the velocity of propagation. They suggest that the effects of gap junction blockers such as octanol, halothane, and heptanol on SD may be due to their effects on membrane function rather than their effects on gap junctions.

2.2 Models of Spreading Depression

Many mathematical models of SD have been developed, at different levels of detail and abstraction. We briefly discuss the features and drawbacks of several other models before introducing our model. The models fall into two main categories: models of a single neuron and continuum models. While models of a single neuron cannot provide information about the propagation of SD, they are useful in developing an understanding of the roles of individual ion channels and can be used to develop continuum models.

2.2.1 Single Point Models

Kager et al. [47, 48, 49] developed a detailed model of a single neuron with a soma and dendrite region, which has different ion channels in different regions. The initial model [47] involved only Na^+ and K^+ and incorporated an abstract buffer for extracellular K^+. A later version of the model [48] incorporated cell swelling and introduced a glial compartment to buffer K^+. A yet later version [49] introduced Cl^- and Ca^{2+}. As a model of a single neuron, the model is unable to fully model K^+ buffering, and the authors made the glial compartment 10 times the volume of the neuron in order to approximate the effects of glial buffering. We find that the approach to cell swelling is rather ad hoc, as it is designed specifically so that the change in the volume fraction of the interstitial space is constrained by the bounds observed in experiments, rather than being based purely on the osmotic forces involved. We also question the validity of using the extracellular K^+ level in the equations governing NMDA receptor activation, as merely the fact that glutamate is released when K^+ is elevated does not mean that NMDA receptor activation is dependent on the extracellular K^+ level. Experimental evidence of NMDA receptor dependence on extracellular K^+ is scarce, with studies mostly showing a correlation between elevated extracellular K^+ and glutamate release that may be an indirect result of the K^+ elevation inducing SD [50, 51]. Kager et al. [47] do reference one source that relates extracellular K^+ directly to NMDA receptor activation, but the

authors suggest that the relationship may be an indirect effect due to changing the rate of repolarization [52]. We believe that the use of extracellular K^+ instead of glutamate in the model of the NMDA receptor mechanics allows a simplification of the system but limits the insight into the role of the NMDA receptor that the model can provide.

Makarova et al. [53, 54] developed a model somewhat similar to the Kager model, but focusing on the membrane resistance. They use a single-cell model with many different regions and a wide range of channels, with different densities in each region. For simplicity, they assume the intra- and extracellular ion concentrations are at steady-state, with different values for the rest state, main part of SD, and ending part of SD. This reduces the number of variables and makes treatment of diffusion and cell swelling unnecessary, allowing for the greater complexity of the model in terms of ion channel mechanics, but unfortunately makes it difficult to expand of the model into a continuum model that might help explain propagation.

A third single neuron model has been used to gain an understanding of the relationships between the different behaviors seen in the brain, including seizures, normoxic SD, and hypoxic SD [22]. Originally developed to study bursting patterns in seizure [55, 56], the model is based on the Hodgkin-Huxley formalism, incorporating a potassium buffer and diffusion away from the extracellular space, which was simplified to perform bifurcation analysis. Further adaptations were made to incorporate more ion channels and oxygen dependence of the Na^+/K^+ ATPase. For different values of the bath K^+ concentration and oxygen concentration, the model displays steady state behavior, seizure firing patterns, tonic firing, SD, and the "wave of death" that is SD without recovery, which results from hypoxic SD if oxygen is not restored. Although this model does a remarkable job of placing SD in the bigger picture of overall neuronal behavior, as a highly simplified model, it does not allow for a detailed understanding of the variety of mechanisms involved in SD itself.

2.2.2 Continuum and Network Models

The first spatial models of SD that incorporated physiological mechanisms were reaction-diffusion type models. The first such model was a continuum model of SD introduced by Tuckwell and Miura [57], who described a reaction-diffusion type model of SD with an intracellular and extracellular compartment. The ion concentrations were governed by extracellular diffusion and transmembrane flow, which was based on ion channel mechanisms. They developed the model with four ions involved, Na^+, K^+, Cl^-, and Ca^{2+}, but only ran computational simulations with K^+ and Ca^{2+} involved. The model successfully displayed the basic one-dimensional wave patterns of SD, with traveling waves and annihilation of two colliding waves. Reggia and Montgomery [58] developed a two-dimensional reaction-diffusion type model of extracellular K^+ dynamics that incorporates synaptic transmission by activating immediate neighbors and inhibiting an annulus around the immediate neighbors. Though the model only abstractly involves ion channels through a polynomial function of K^+ as the reaction term with a generalized reuptake term, it produced wave patterns similar to those seen during the visual aura of migraine. Revett et al. [59] adapted the Reggia and Montgomery model to include Ca^{2+} and glutamate, both with reaction-diffusion equations similar to that of K^+.

Almeida et al. [60, 61] took the basic idea of Tuckwell and Miura's model with all four ions, expanded it to three dimensions, and increased the detail of the physiological mechanisms. Rather than the simplification of pure diffusion, they use electrodiffusion to incorporate the effects of charge differences on the diffusion of ions. In addition, they expand the model to three compartments: the extracellular space, presynaptic terminal, and postsynaptic terminal. Transmembrane ion flux is modeled by a generic GHK current equation (see section 3.2.2 for an explanation of the GHK equations) and pump term, with glial K^+ buffering incorporated into the pump term. The model was then adapted to incorporate a number of specific ion channels, pumps, and cotransporters,

glia, neuronal gap junctions, and neuronal cell swelling [62]. A concern with this model is the manner in which the potentials are calculated. The formula for the extracellular potential is based on the assumption that the total current at each point is zero, and the membrane potential was similarly calculated under the assumption that the sum of the transmembrane ionic currents is zero. They briefly mention using a "membrane equivalent circuit" instead, but they do not provide equations anywhere or discuss the effects beyond necessitating a decrease in time step in the numerical simulation [62].

A thorough computational investigation into NMDA receptors and glutamate mechanics appears in Bennett et al. [63]. The model consists of a lane of neurons adjacent to a lane of astrocytes, which communicate with each other by way of glutamate and ATP. Glutamate released from astrocytes acts on the neighboring neuron by triggering the NMDA receptors, while glutamate released from neurons acts on the next astrocyte by triggering metabotropic receptors. Astrocytes communicate with their neighbors through ATP. In addition, a wide range of ion channels are included in the model, which tracks K^+, Na^+, Cl^-, and Ca^{2+}, as well as gap junctions between astrocytes. However, the model does not include diffusion of any form beyond that inherent to the structure of the glutamate and ATP effects. Further, it incorporates the method used by Almeida et al. [60] to calculate the potentials, adapted to account for the lack of diffusion in the model itself.

Yao et al. [64] introduced a model that was similar to Tuckwell and Miura's, but added intracellular and extracellular volume changes. Additionally, they use a more comprehensive set of ion channels and pumps, basing them off of the single cell model by Kager et al. [47, 48]. Their treatment of the membrane potential, with the capacitance times the change in potential equal to the total current, is consistent with the rest of the model. The model uses diffusion rather than electrodiffusion, and as such ignores both the influence of the potentials on the ionic diffusion and the reciprocal influence of ionic diffusion on the potentials.

Chang et al. [65] presented another continuum model incorporating the same ion

channels and pumps, but distinguishing between the dendritic and somatic parts of neurons. In addition, they incorporate an abstract buffer for glial K^+ buffering and make the Na^+/K^+ ATPase strength dependent on oxygen supply, which is in turn dependent on the blood flow rate. In order for the blood flow rate to be fully involved in the system, they include vasoconstriction and vasodilation with the vessel radius being a function of extracellular K^+. This model also uses diffusion rather than electrodiffusion and assumes that cell volumes stay constant due to simulations in other models showing that including cell swelling has minimal effect.

A significantly different continuum model was proposed by Shapiro [66, 67]. Though based on a similar collection of ion channels and pumps as the previously mentioned models, and incorporating neuronal swelling in much the same way as other models, this model features a neuronal syncytium. In order to represent the gap-junctional coupling, electrodiffusion governs the flow of ions within the neuronal compartment, with the diffusion coefficient being voltage, Ca^{2+}, and pH dependent. This choice is due to known cardiac dependencies, but may have no relation to neuronal gap junctions. The extracellular ion concentrations, however, obey the standard reaction-diffusion equations without involvement of the electrostatic potential except as it affects the transmembrane flow. The computation of the membrane potential is done using the GHK equation rather than being based on current flow. Further information regarding the GHK equation and the drawbacks to using it can be found in section 3.2.2.

Our model develops on a model by Mori [68], which presents a generic framework for fully incorporating electrodiffusion and cell swelling in a model otherwise fairly similar to that of Yao et al. [64]. This model is defined in such a way as to be easily extended to incorporate different aspects of SD or other physiological phenomena, but has previously been simulated with only the neuronal and extracellular compartments and no form of K^+ buffering in one spatial dimension. In this thesis, we present the general model in Chapter 3. We then take this general framework and look at several different specific versions of the model to examine the role various biophysical processes play in SD.

Chapter 3

Model

As in many of the models described in the previous chapter, we model nervous tissue as a homogenized continuum, with multiple compartments which overlap everywhere, using the general framework presented by Mori [68]. In our simulations, we include varying numbers of compartments, though we always have a neuronal and extracellular compartment. In the majority of our simulations, we include a glial compartment as well, and in some we have two neuronal compartments. The model is designed specifically to be thermodynamically consistent, so that it satisfies a free energy identity, regardless of the number or type of compartments used [68]. In all of our compartments, ionic concentrations obey electrodiffusion, rather than just diffusion, with source terms for transmembrane flow, and osmotic water flow determines cell volume. We determine the membrane potentials in a physically consistent manner. Additionally, we include the possibility of fluid flow in our model, though only a few simulations include it due to the dramatic increase in the complexity caused by the inclusion.

We start developing our model by finding the fundamental conservation equations governing the system in 3.1 and then look at the necessary constitutive equations in section 3.2. We present the model first in full generality, and will discuss the variations used in our simulations in sections 3.3–3.5. Section 3.6 gives a full accounting of the ion

channels and transporters used, with a description of the protocol used to trigger SD in section 3.7. The numerical method is presented in section 3.8. Finally, the energy identity is given in section 3.9. The variables of interest are cell volume, intracellular and extracellular concentrations of ions, electrostatic potential, and fluid flow. In order to handle cell volume on a macroscopic level, we treat the intracellular and extracellular space as a multi-phasic continuum and assign volume fractions for each phase. Let α_k denote the volume fraction of the k-th phase, where $k = 1, \cdots, N-1$ represent the intracellular space of different cellular compartments and $k = N$ represents the extracellular space. We then define c_i^k to be the concentration of the ion species i in the k-th phase and ϕ_k to be the electrostatic potential in the k-th phase.

3.1 Conservation Equations

3.1.1 Volume Fractions

Let us begin by looking at the equations governing cell volume. We assume that the fluids in our system are incompressible, so that cell volume changes only as a result of fluid flow, and that each intracellular phase only interacts with itself and the extracellular phase. Then conservation of mass dictates that

$$\frac{\partial \alpha_k}{\partial t} + \nabla \cdot (\alpha_k \mathbf{u}_k) = -\gamma_k w_k, \qquad k = 1, \cdots, N-1, \tag{3.1}$$

$$\frac{\partial \alpha_N}{\partial t} + \nabla \cdot (\alpha_N \mathbf{u}_N) = \sum_{k=1}^{N-1} \gamma_k w_k, \tag{3.2}$$

where $\mathbf{u}_k$ denotes flow within the k-th compartment, w_k denotes outward flow per unit area through the cell membrane, and γ_k is the area of the cell membrane per unit volume, which we will assume to be constant for simplicity. In addition, we must have

$$\sum_{k=1}^{N} \alpha_k = 1 \tag{3.3}$$

to ensure incompressibility. Taking the time derivative of (3.3) and plugging in (3.1) and (3.2) yields the incompressibility condition

$$\sum_{k=1}^{N} \nabla \cdot (\alpha_k \mathbf{u}_k) = 0. \tag{3.4}$$

3.1.2 Ion Concentrations

Next we turn to conservation of ions. For simplicity, we consider only M ion species in detail and assume the remaining species of ions do not move in space or across the membranes, allowing us to collect them into a single immobile ion term. Though the concentrations of the immobile ions will change as the volume fractions change, the overall amount in each compartment a_k will be constant in time, and they contribute a charge density that we will denote ρ_0^k.

For each ion species $i = 1, \cdots, M$ that we do consider to be mobile, each with valence z_i, conservation of ions requires that

$$\frac{\partial(\alpha_k c_i^k)}{\partial t} + \nabla \cdot (\alpha_k c_i^k \mathbf{u}_k) = \nabla \cdot \left(D_i^k \left(\nabla c_i^k + \frac{z_i F c_i^k}{RT} \nabla \phi_k \right) \right) - \gamma_k j_i^k, \ k = 1, \cdots, N-1, \tag{3.5}$$

$$\frac{\partial(\alpha_N c_i^N)}{\partial t} + \nabla \cdot (\alpha_N c_i^N \mathbf{u}_N) = \nabla \cdot \left(D_i^N \left(\nabla c_i^N + \frac{z_i F c_i^N}{RT} \nabla \phi_N \right) \right) + \sum_{k=1}^{N-1} \gamma_k j_i^k, \tag{3.6}$$

where D_i^k is the diffusion coefficient for the i-th ion species in the k-th phase, which may be a function of α_k, j_i^k is the outward flow per unit area through the cell membrane, and R and T are the ideal gas constant and absolute temperature, respectively. The diffusion coefficients are discussed in more detail in sections 3.3–3.5.

3.1.3 Electrostatic Potentials

For the electrostatic potential, we define $\phi_{kN} = \phi_k - \phi_N$ for $k = 1, \cdots, N-1$ and use the algebraic charge-capacitance equations

$$\gamma_k C_{\mathrm{m}}^k \phi_{kN} = \rho_0^k + \sum_{i=1}^{M} z_i F \alpha_k c_i^k \quad k = 1, \cdots, N-1, \tag{3.7}$$

$$-\sum_{k=1}^{N-1} \gamma_k C_{\mathrm{m}}^k \phi_{kN} = \rho_0^N + \sum_{i=1}^{M} z_i F \alpha_N c_i^N. \tag{3.8}$$

Observe that if we add the N electrostatic potential equations, we find the electroneutrality condition

$$0 = \sum_{k=1}^{N} \left(\rho_0^k + \sum_{i=1}^{M} z_i F \alpha_k c_i^k \right).$$

3.1.4 Fluid Flow

For fluid flow, we have the velocity fields $\mathbf{u}_k$, and assume that our flow is a potential flow given by

$$\zeta_k \mathbf{u}_k = -\nabla \left(p_k - RT \frac{a_k}{\alpha_k} \right) - \sum_{i=1}^{M} z_i F c_i^k \nabla \phi_k, \tag{3.9}$$

where ζ_k is the hydraulic resistivity and p_k is the pressure for the k-th phase. In general, ζ_k is a tensor that may vary spatially, but for simplicity we assume that it is a spatially-constant scalar proportional to the volume fraction. We then define the hydraulic permeability to be $\kappa_k = \alpha_k / \zeta_k$, which will be used more often than ζ_k in the computations to follow.

3.2 Constitutive Equations

The system of equations in section 3.1 is not closed, since the flow per unit area of water across the membrane w_k, the flow per unit area of ions across the membrane j_i^k, and the pressure p_k have not yet been specified. To close the system, we must develop constitutive equations for these variables. Because the flow across the membranes will

depend on differences across the membrane, we define two new variables for notational convenience:

$$p_{kN} = p_k - p_N, \tag{3.10}$$

$$\pi_{kN} = RT\left(\frac{a_k}{\alpha_k} + \sum_{i=1}^{M} c_i^k - \frac{a_N}{\alpha_N} - \sum_{i=1}^{M} c_i^N\right). \tag{3.11}$$

Observe that p_{kN} is the mechanical pressure difference across the membrane and π_{kN} is the osmotic pressure difference.

3.2.1 Water Flux

The constitutive equation we choose for w_k is based on assuming that flow of water across the membrane is due to two factors: osmotic pressure and mechanical pressure p_k. If we assume that these two pressures are independent, then w_k should be the proportional to the sum of the two factors. Thus we take, for $k = 1, \cdots, N-1$,

$$w_k = \eta_k(p_{kN} - \pi_{kN}). \tag{3.12}$$

The proportionality constant η_k is the hydraulic permeability of the cell membrane. In general, η_k may be dependent on the volume fraction, for instance if aquaporins opened or closed on the membrane in response to cell swelling, or spatially dependent. For simplicity, however, we assume that η_k is constant.

3.2.2 Ion Flux

The flow of ions across the membrane is a function of the ion channels and transporters that exist on the membrane. Although the overall structure of most channels is similar, the details are highly dependent on the specific channel, and different variations of the model incorporate different channels. Sections 3.3–3.5 will list which channels are used in each variation, and a full explanation of all the channels used can be found in section 3.6. Here we discuss the overall structure of most ion channels and transporters.

We first separate the channels from the transporters, distinguishing "passive" flow from "active" flow. We will denote active flow by h_i^k, representing transporters, which have a general constitutive relation that may depend on the concentrations and membrane potential, as well as possible dependence on position. The passive flow consists of the ion channels, which may have different gating properties as well as some form of current-voltage relationship. The net ion flux per membrane area j_i^k can then be described as the sum of the different channels, pumps, and transporters.

$$j_i^k = \sum_\mu h_i^{k,\mu} + \sum_\mu \hat{g}_i^{k,\mu} J_i^{k,\mu}, \tag{3.13}$$

where $\hat{g}_i^{k,\mu}$ is the proportion of open channels of type μ, and is in turn a function of the gating variables.

Channel Current-Voltage Relationship

The net flow of ions through an open channel is determined by the channel's current-voltage relationship, which has two factors. Those factors are the concentrations on either side of the membrane and the membrane potential. In order to understand the current-voltage relationship, we first look at the basic properties of any flow across the membrane.

If the membrane potential is zero, ions will flow down the concentration gradient, from the side of the membrane with a higher concentration to the side with the lower concentration. If the membrane potential is nonzero, however, electrostatics play a role in the flow of ions. For any set of intracellular and extracellular concentrations, there is a membrane potential such that the electrostatic forces exactly counteract the diffusion, resulting in no net ionic flow across the membrane. To find this membrane potential, called the Nernst potential, we must find a formula for the electrochemical potential on each side of the membrane and find the membrane potential for which the electrochemical potential is equal on the two sides [69].

For the membrane separating compartment k from the extracellular space, we have the intracellular concentration c_i^k and the extracellular concentration c_i^N of ion i, which has valence z_i. We assume that each ion behaves like an ideal gas, so that the ions exert intracellular and extracellular pressures $p_i^k = c_i^k RT$ and $p_i^N = c_i^N RT$. To determine the electrochemical potential, we suppose that we have a solution subjected to an electric field E in the x direction at equilibrium (for the purposes of this discussion, the x direction is along the channel). For simplicity in the derivation of the Nernst potential, we temporarily drop the indices and let c denote the concentration. Then we must have

$$-RT\frac{dc}{dx} + zFcE = 0,$$

where F is Faraday's constant. Letting ϕ be the electrostatic potential along the channel, we have $E = -\frac{d\phi}{dx}$. Substituting that in, we can divide by c and integrate to find that $RT \ln c + zF\phi$ must be constant at equilibrium.

Thus, if the net flow of ions across the cell membrane is zero, then we must have

$$RT \ln c_i^k + z_i F \phi_k = RT \ln c_i^N + z_i F \phi_N.$$

Solving that for the membrane potential, $\phi_k - \phi_N$, we get the Nernst equation for the reversal potential E_i^k for ion species i,

$$E_i^k = \frac{RT}{z_i F} \ln\left(\frac{c_i^N}{c_i^k}\right). \tag{3.14}$$

If we assume a linear current-voltage (or ohmic) relationship for an ion channel and let the current of ion i through channel μ be given by $I_i^{k,\mu}$, we have

$$I_i^{k,\mu} = G_i^{k,\mu}(\phi_{kN} - E_i^k), \tag{3.15}$$

where $G_i^{k,\mu}$ is the conductance through the channel of type μ. The current equation can be converted into ion flux by dividing by $z_i F$:

$$J_i^{k,\mu} = \frac{G_i^{k,\mu}}{z_i F}(\phi_{kN} - E_i^k). \tag{3.16}$$

Since the Nernst potential itself is a function of the concentrations, we may also write this as

$$J_i^{k,\mu} = \frac{G_i^{k,\mu}}{z_i^2 F^2}\left(z_i F \phi_{kN} - RT\left(\frac{c_i^N}{c_i^k}\right)\right). \tag{3.17}$$

This is a common and fairly simple description of ion flow through channels, used in the Hodgkin-Huxley model of action potentials [69].

Suppose we assume instead that the electric field across the membrane is constant, so that ϕ is linear. We can then find a steady state concentration gradient as a function of the membrane potential. From this, we can determine the corresponding flux and current. The steady state current is given by

$$I_i^{k,\mu} = P_i^{k,\mu}\frac{z_i^2 F^2 \phi_{kN}}{RT}\frac{c_i^k \exp(\frac{z_i F \phi_{kN}}{RT}) - c_i^N}{\exp(\frac{z_i F \phi_{kN}}{RT}) - 1}, \tag{3.18}$$

where $P_i^{k,\mu}$, called the permeability, is a function of the diffusion coeffiecient and properties of the ion channel and membrane [69]. This current-voltage relationship, known as the Goldman or GHK current equation, satisfies ion flow from high to low electrochemical potential. Again, we can easily convert this to the ion flux by dividing by $z_i F$ to get

$$J_i^{k,\mu} = P_i^{k,\mu}\frac{z_i F \phi_{kN}}{RT}\frac{c_i^k \exp(\frac{z_i F \phi_{kN}}{RT}) - c_i^N}{\exp(\frac{z_i F \phi_{kN}}{RT}) - 1}. \tag{3.19}$$

We detour briefly from our discussion of ion channels to note how the Goldman current equation gives rise to the GHK formula for the membrane potential. The Goldman-Hodgkin-Katz (GHK) formula, sometimes called the constant field equation, gives the resting membrane potential as a function of the permeabilities and concentrations of the different ions. We can derive the GHK formula by combining the Goldman current equation with the fact that the net current should be zero if the cell is at steady state:

$$\sum_{i,\mu} I_i^{k,\mu} = 0. \tag{3.20}$$

We can then solve for ϕ_{kN} to get

$$\phi_{kN} = \frac{RT}{F}\ln\left(\frac{P_K c_K^{\mathrm{e}} + P_{Na} c_{Na}^{\mathrm{e}} + P_{Cl} c_{Cl}^{\mathrm{i}}}{P_K c_K^{\mathrm{i}} + P_{Na} c_{Na}^{\mathrm{i}} + P_{Cl} c_{Cl}^{\mathrm{e}}}\right), \tag{3.21}$$

where P_i represents the combined permeability of all channels through which ion i flows. Typically, this formula includes only Na^+, K^+, and Cl^-, the three ions with the most significant concentrations and permeabilities, as shown here. It can be extended to include Ca^{2+} and other ions, as well as the activity of electrogenic ion pumps, but solving for ϕ_{kN} may no longer be possible with the inclusion of these terms. We point out that using the GHK formula for computing the membrane potential during SD requires making the assumption that the membrane potential adjusts instantaneously to the resting potential that matches the concentrations and therefore limits the ability of the model to accurately portray the interactions between ion concentrations and membrane potential. Its value is further inhibited by the inability to incorporate any electrogenic pumps or transporters.

Gating Variables

The idea of gating variables appears in the Hodgkin-Huxley model of the action potential. Since channels open and close as a result of changes in their surroundings, whether due to the presence or absence of neurotransmitters or to changes in the membrane potential, we need some way of incorporating these aspects in the channel equations. Gating variables are channel specific, but many share common features, particularly for those dependent on the voltage. Letting s be a generic gating variable for a voltage-dependent channel, we can model s as follows:

$$\frac{ds}{dt} = \frac{s_\infty(\phi_{kN}) - s}{\tau_s(\phi_{kN})} \tag{3.22}$$

where

$$s_\infty(\phi_{kN}) = \frac{\alpha_s(\phi_{kN})}{\alpha_s(\phi_{kN}) + \beta_s(\phi_{kN})},$$
$$\tau_s = \frac{1}{\alpha_s(\phi_{kN}) + \beta_s(\phi_{kN})}.$$

The details of the individual gating variables are given in section 3.6 for each channel included. In addition, an explanation of the gating variables in the NMDA receptor, which includes dependence on glutamate as well as voltage, are discussed in section 6.1.

Transporters

Of the many different ion pumps that serve as active transporters, the ubiquitous Na^+/K^+ ATPase is particularly instrumental in maintaining (or restoring) the concentration gradients for Na^+ and K^+. This transporter uses the energy obtained by converting adenosine triphosphate (ATP) into adenosine diphosphate (ADP) to transport Na^+ out of the cell and K^+ into the cell, moving three Na^+ ions and two K^+ ions with each molecule of ATP [1]. Due to the charge disparity of the ions exiting the cell with those entering, the Na^+/K^+ ATPase is an electrogenic pump, and its contribution to the electric current must be incorporated into calculations of the membrane potential. The transporters that depend on some form of energy have a highly specific set of equations that will depend on the availability of the energy source, but simplifying assumptions may be used to avoid the additional complexity of modeling the energy source.

Additional transporters, commonly called secondary active transporters, use the concentration gradients of one ion, typically Na^+ or K^+, to transport other ions or amino acids across the cell membrane [1]. To model the action of secondary active transporters, we consider a generic transporter that moves L different ion types, $i_1, \cdots, i_L$. If b_{i_j} ions of type i_j are transported out of the cell at a time (note that negative values of b_{i_j} will appear if the transporter moves i_j into the cell), the behavior of the transporter can be modeled by the equations

$$J_k^\mu = P^\mu \ln\left(\frac{(c_{i_1}^k)^{b_{i_1}} \cdots (c_{i_L}^k)^{b_{i_L}}}{(c_{i_1}^N)^{b_{i_1}} \cdots (c_{i_L}^N)^{b_{i_L}}}\right), \tag{3.23}$$

$$h_{i_j}^{k,\mu} = b_{i_j} J_k^\mu. \tag{3.24}$$

Some secondary active transporters may have more complex mechanisms, resulting in modifications to this equation.

3.2.3 Pressure and Fluid Flow

Finally, to determine the pressures p_k, we start by considering p_{kN}. The pressure difference must be due to a force balance, which is dependent on mechanical tension due to the geometry of the cell membrane. Since our model only addresses the geometry of the cell through the volume fraction, the mechanical tension must be a function of volume fraction. We take the simple constitutive relation

$$p_{kN} = S_k(\alpha_k - \alpha_k^0), \tag{3.25}$$

where S_k is a stiffness constant and α_k^0 is the volume fraction that results in the membrane having no tension. We note that this choice of constitutive equation can be derived from the energy function

$$\mathcal{E} = \frac{1}{2}\sum_{k=1}^{N-1} S_k(\alpha_k - \alpha_k^0)^2 \tag{3.26}$$

so that for all $k = 1, \cdots, N-1$, we have

$$p_{kN} = \frac{\partial \mathcal{E}}{\partial \alpha_k}$$

as discussed in [68].

From the constitutive relation on p_{kN} we can compute p_k given α_k and p_N, but we are still missing p_N. We can find an equation for p_N by using the constitutive relation for p_{kN} (3.25) and the incompressibility condition (3.4). Substituting $p_k = S_k(\alpha_k - \alpha_k^0) + p_N$ into the fluid flow equations (3.9) and then plugging the fluid flow equations into equation (3.4) yields

$$\sum_{k=1}^{N} \nabla \cdot \left(-\kappa_k \nabla \left(S_k(\alpha_k - \alpha_k^0) + p_N - RT\frac{a_k}{\alpha_k} \right) - \kappa_k \sum_{i=1}^{M} z_i F c_i^k \nabla \phi_k \right) = 0. \tag{3.27}$$

With equations (3.1)–(3.9), (3.12), (3.13), and (3.25) we have a system of equations that describes the dynamics of volume fractions, ion concentrations, fluid flow, and electrostatic potentials for a general physiological system. Depending on the physiology

in question, the constants involved, as well as the particular constitutive equations, may vary significantly. Additionally, the boundary conditions are highly dependent on the context. Since the pressure and electrostatic potential are only determined up to a constant, we can set both p_N and ϕ_N to be zero at one point.

We now discuss the specific variations on the general model presented in sections 3.1–3.2. We look at four distinct versions. Three of these models are in one spatial dimension, with two, three, and four compartments, over a 1-cm wide domain, and the fourth is a two-dimensional model with three compartments over a 1-cm square domain. For all of these models, we restrict our attention to the three most prevalent ions: Na^+, K^+, and Cl^-. Sections 3.3–3.5 describe the specific parameters used in each of these versions. In all, we assume no-flux boundary conditions for all ions and fluid flow at both edges of the domain, and α_k^0 is equal to the initial condition for α_k. For all one-dimensional simulations, we set p_N and ϕ_N to be 0 at the right edge. In the two-dimensional simulations, ϕ_N is set to be 0 at the point $(10, 10)$, where x and y give the position in mm.

3.3 Two Compartment Models

The two compartment model is used to examine the effects of incorporating fluid flow, discussed in Chapter 4. The two compartments are the neuronal and the extracellular compartments. The specific ion channels and transporters included are the persistent sodium channel, the potassium delayed rectifier, the transient potassium channel, leaks for each of sodium, potassium, and chloride, and the Na^+/K^+ ATPase. The diffusion coefficients in the neuronal compartment were set to be very small, while diffusion in the extracellular compartment was proportional to the extracellular volume fraction,

	Neuronal	Extracellular
α	0.8	0.2
$[Na^+]$ (mM)	9.82	141.6
$[K^+]$ (mM)	133.45	3.86
$[Cl^-]$ (mM)	10	130
ϕ (mV)	-70	0
a (mmol)	0.1066	0.0031
ρ_0 (C)	-10.3	-0.298

Table 3.1: Initial values of the variables in each compartment for the model with two compartments. Values for Na^+ and K^+ match those of [64].

with inclusion of a tortuosity term λ.

$$D_i^{\mathrm{n}} = 10^{-4} D_i^*$$
$$D_i^{\mathrm{e}} = D_i^* \alpha_{\mathrm{e}} / \lambda^2$$

The initial conditions were set according to the values in Table 3.1, and the system was allowed to come to a resting state prior to the excitation protocol. The parameters for this model are given in Table 3.2, and the resting state achieved prior to the excitation given in Table 3.3.

3.4 Three Compartment Models

The three compartment model, in both one and two spatial dimensions, allows us to explore the effects of glial cells, discussed further in Chapter 5, with two-dimensional results in section 7.2. The three compartments are neuronal, glial, and extracellular. The neuronal membrane has the same ion channels and transporters as in the fluid flow model: the persistent sodium channel, the potassium delayed rectifier, the transient potassium channel, leaks for each of sodium, potassium, and chloride, and the Na^+/K^+ ATPase. The glial membrane has the potassium inward rectifier, leak channels for sodium and chloride, the Na^+/K^+ ATPase, and the sodium, potassium, and chloride cotransporter. We leave out the intracompartmental fluid flow terms in this model,

Table 3.2: Parameter values for the model with two compartments

Parameter	Value	Source
C_{m}	0.75 μF/cm^2	[47, 64]
membrane area	1.586×10^{-5} cm^2	[47, 64]
volume	2.484×10^{-9} cm^3	[47, 64]
γ_{n}	6.3849×10^3 1/cm	membrane area/volume
$P_{\mathrm{Na}}^{\mathrm{n,P}}$	2×10^{-5} cm/s	[47, 64]
$P_{\mathrm{K}}^{\mathrm{n,DR}}$	1×10^{-3} cm/s	[47, 64]
$P_{\mathrm{K}}^{\mathrm{n,A}}$	1×10^{-4} cm/s	[47, 64]
$G_{\mathrm{Na}}^{\mathrm{n,L}}$	2×10^{-2} mS/cm^2/s	[64]
$G_{\mathrm{K}}^{\mathrm{n,L}}$	7×10^{-2} mS/cm^2	[64]
$G_{\mathrm{Cl}}^{\mathrm{n,L}}$	20×10^{-2} mS/cm^2	[64]
m_{K}	2×10^{-3} mmol/cm^3	[64]
m_{Na}	7.7×10^{-3} mmol/cm^3	[64]
$\bar{I}_{\mathrm{n}}$	13 μA/cm^2	[64]
η	6×10^{-10} cm/sec/mmHg	[70]
κ_{n}	5×10^{-9} cm^4/dynes/sec [a]	[71]
κ_{e}	5×10^{-9} cm^4/dynes/sec [a]	[71]
S_{n}	2.58×10^6 Pa/cm^3 [a]	[b]
D_{Na}^*	1.33×10^{-5} cm^2/sec	[72]
D_{K}^*	1.96×10^{-5} cm^2/sec	[72]
D_{Cl}^*	2.03×10^{-5} cm^2/sec	[72]
λ	1.6	[73]
T	310.15 K	[47]

[a] Values were varied in some simulations as described in Chapter 4.
[b] We are unaware of any existing values for the stiffness constant and explored a range of values to see the effect. See section 4.2.

	Neuronal	Extracellular	Neuronal	Extracellular
α	0.795	0.205	.80	.20
[Na^+] (mM)	9.56	139.67	9.64	142.29
[K^+] (mM)	134.14	4.05	133.42	3.99
[Cl^-] (mM)	9.67	128.60	9.78	130.83
ϕ (mV)	-69.15	0	-69.31	0

Table 3.3: Resting values of the variables in each compartment for the model with two compartments. The left-hand side is the resting values with the stiffness constant $S_{\mathrm{n}} = 0$ while the right-hand side is with $S_{\mathrm{n}} = 2.58 \times 10^8$ Pa/cm^3.

assuming that the hydraulic permeability κ_k and stiffness constant S_k are zero, so that the pressure is uniform throughout. For the three compartment model, we ran simulations with different values of the glial diffusion coefficient, the potassium inward rectifier permeability on the glial membrane, and the maximum strength of the Na^+/K^+ ATPase.

The diffusion coefficients were calculated differently for each compartment. The neuronal diffusion coefficients were all set to 0. The glial diffusion coefficients were assumed to be independent of volume changes, since diffusion in the glial compartment was assumed to occur through gap junctions, but the resting volume fraction of the glia was used in determining the coefficients. To reflect different possible amounts of gap-junctional coupling, the glial diffusion coefficients were scaled by a factor d, which was 0.25 in the majority of simulations. The extracellular diffusion coefficients were assumed to be proportional to the volume fraction, and all compartments were scaled by the square of the tortuosity term λ.

$$
\begin{aligned}
D_i^{\mathrm{n}} &= 0, \\
D_i^{\mathrm{g}} &= dD_i^* \alpha_{\mathrm{g}}^0 / \lambda^2, \\
D_i^{\mathrm{e}} &= D_i^* \alpha_{\mathrm{e}} / \lambda^2.
\end{aligned}
$$

In two dimensions, we use d_x and d_y instead of d to allow for an anisotropic glial diffusion coefficient.

When exploring the effects of changing the permeabilities of certain parameters, as was done in the three and four compartment simulations, we set the initial conditions and parameter values in such a way that the stationary state of the cell was the same in as many of our simulations as possible. This requires a significant change in how the initial conditions and parameters are set. We set the resting values of the ion concentrations and membrane potentials to be those given in Table 3.4, with the neuronal chlorine concentration dictated by the extracellular chlorine concentration and the membrane potential because chlorine only crossed the neuronal membrane through a leak channel

	Neuronal	Glial	Extracellular
α	0.5	0.3	0.2
$[Na^+]$	10 mM	10 mM	140 mM
$[K^+]$	130 mM	130 mM	3.4 mM
$[Cl^-]$	8.7442 mM*	8.7442 mM*	120 mM
ϕ	-70 mV	-85 mV	0 mV
a (mmol)	58.5779*	35.1468*	.5
ρ_0 (C)	-6.3325×10^3*	-3.7997×10^3*	-0.4508×10^3*

Table 3.4: Equilibrium values of the variables in each compartment for the three compartment models. Values with asterisks were calculated as described in the main text, while those without asterisks were chosen based on values in the literature.

in our model. We set the glial chlorine concentration equal to the neuronal chlorine concentration. Some simulations were also run with $\phi_n = -75$ mV and $\phi_g = -90$ mV. The calculated parameter values varied somewhat with this change, but the method of calculation was the same.

With the volume fraction, concentrations, and electrostatic potentials set, we determined the parameter values as necessary for the system to be at rest. For the neuron, we started by taking the two potassium channel permeabilities, the gating variables, and the leak permeability from the literature [47, 64] and then set the Na^+/K^+ ATPase pump strength so that $\frac{\partial c_K^n}{\partial t} = 0$. We then took the persistent sodium channel permeability from the literature [47, 64] and set the sodium leak permeability so that $\frac{\partial c_{Na}^n}{\partial t} = 0$.

For the glial compartment, we first set the sodium potassium chloride cotransporter permeability so that the glial chloride concentration was at rest. We then set the potassium inward rectifier channel strength, either from the literature [74] or modified for experimental purposes, and calculated the glial Na^+/K^+ ATPase pump strength so that $\frac{\partial c_K^g}{\partial t} = 0$. Since the only other sodium current on the glial membrane in our model is the leak current, we then set the sodium leak permeability so that $\frac{\partial c_{Na}^g}{\partial t} = 0$. We note that the glial Na^+/K^+ ATPase pump strength and leak Na^+ permeability are both dependent on the strength of the glial potassium inward rectifier. Values of all parameters are given in Table 3.5, with those that were affected by the change in resting

Table 3.5: Parameter values for the three compartment model.

Parameter	Value	Source
C_{m}	0.75 μF/cm^2	[47, 64]
membrane area	1.586×10^{-5} cm^2	[47, 64]
volume	2.484×10^{-9} cm^3	[47, 64]
γ_{n}	6.3849×10^3 1/cm	membrane area/volume
γ_{g}	6.3849×10^3 1/cm	[a]
$P_{\mathrm{Na}}^{\mathrm{n,P}}$	2×10^{-5} cm/s	[47, 64]
$P_{\mathrm{K}}^{\mathrm{n,DR}}$	1×10^{-3} cm/s	[47, 64]
$P_{\mathrm{K}}^{\mathrm{n,A}}$	1×10^{-4} cm/s	[47, 64]
$G_{\mathrm{K}}^{\mathrm{g,IR}}$	13×10^{-2} mS/cm^2 [b]	[74]
$G_{\mathrm{Na}}^{\mathrm{n,L}}$	6.2738×10^{-9} mmol/cm^2/s	calculated
$G_{\mathrm{Na}}^{\mathrm{g,L}}$	2.1290×10^{-9} mmol/cm^2/s	calculated
$G_{\mathrm{K}}^{\mathrm{n,L}}$	7×10^{-2} mS/cm^2	[64]
$G_{\mathrm{Cl}}^{\mathrm{n,L}}$	10×10^{-2} mS/cm^2	[47]
$G_{\mathrm{Cl}}^{\mathrm{g,L}}$	5×10^{-2} mS/cm^2	[c]
m_{K}	2×10^{-3} mmol/cm^3	[64]
m_{Na}	7.7×10^{-3} mmol/cm^3	[64]
$\bar{I}_{\mathrm{n}}$	1.5972×10^{-7} mmol/cm^2/s [b]	calculated
$\bar{I}_{\mathrm{g}}$	7.5890×10^{-8} mmol/cm^2/s [b]	calculated
P^{NaKCl}	9.1806×10^{-10} mmol/cm^2/s	calculated
η_{n}	5.4×10^{-5} cm/sec/(mmol/cm^3)	[66]
η_{g}	5.4×10^{-5} cm/sec/(mmol/cm^3)	[66]
D_{Na}^*	1.33×10^{-5} cm^2/sec	[72]
D_{K}^*	1.96×10^{-5} cm^2/sec	[72]
D_{Cl}^*	2.03×10^{-5} cm^2/sec	[72]
λ	1.6 [b]	[73]
T	310.15 K	[47]

[a] Glial area of cell membrane per unit volume taken to be equal to that of the neuron.

[b] Values were varied in simulations. Calculated values are based on the parameters given, but changes to $P_{\mathrm{K}}^{\mathrm{g,IR}}$ will affect $\bar{I}_{\mathrm{g}}$ and $G_{\mathrm{Na}}^{\mathrm{g,L}}$. These values will scale roughly with $P_{\mathrm{K}}^{\mathrm{g,IR}}$.

[c] Glial Cl^- leak value chosen to ensure that other parameter values were always positive.

Parameter	Value
$G_{\mathrm{Na}}^{\mathrm{n,L}}$	5.1774×10^{-9} mmol/cm^2/s
$G_{\mathrm{Na}}^{\mathrm{g,L}}$	7.5693×10^{-10} mmol/cm^2/s
$\bar{I}_{\mathrm{n}}$	1.3299×10^{-7} mmol/cm^2/s
$\bar{I}_{\mathrm{g}}$	3.932×10^{-8} mmol/cm^2/s
P^{NaKCl}	8.4351×10^{-10} mmol/cm^2/s

Table 3.6: Calculated parameter values for the three compartment simulations with resting membrane potentials $\phi_{\mathrm{n}} = -75$ and $\phi_{\mathrm{g}} = -90$ mV.

membrane potential given in Table 3.6.

Finally, to ensure that the volume fractions were at rest and the charge-capacitance relationships were properly satisfied, we set the organic (impermeable) anion amounts and the charge densities they contribute in each compartment. The extracellular organic anion amount was set arbitrarily, and the intracellular amounts were set so that the total osmotic pressure in all compartments was equal, guaranteeing that $\frac{\partial \alpha_k}{\partial t} = 0$ for all k. The charge densities were set in each compartment independently so that the charge-capacitance relationships were satisfied. These values are given in Table 3.4.

For the simulations in which the Na^+/K^+ ATPase strength was varied, the adjustment was made after all parameter values were set as above by multiplying $\bar{I}$, the maximum pump strength, by a constant. The change resulted in the initial condition no longer being a rest state, and the simulation was allowed to approach a rest state prior to introducing the excitatory fluxes that triggered SD. Table 3.7 shows the resulting rest state values for these simulations with $\phi_{\mathrm{n}} = -70$ and $\phi_{\mathrm{g}} = -85$, and Table 3.8 shows the resulting rest state values for the simulations with $\phi_{\mathrm{n}} = -75$ and $\phi_{\mathrm{g}} = -90$.

3.5 Four Compartment Models

We explore neuronal interactions in greater detail with the four compartment model. In addition to the glial and extracellular compartments, this model has two neuronal

Table 3.7: Rest values for different Na^+/K^+ ATPase values with initial membrane potentials $\phi_{\rm n} = -70$ mV and $\phi_{\rm g} = -85$ mV, with b_n and b_g denoting the multiplier for the neuronal and glial membranes. All concentrations are in mM and potentials in mV. For all values, we have $\alpha_{\rm e} = 1 - \alpha_{\rm n} - \alpha_{\rm g}$ and $\phi_{\rm e} = 0$.

b_n	b_g	α_n	α_g	$c^{\rm n}_{Na}$	$c^{\rm g}_{Na}$	$c^{\rm e}_{Na}$	$c^{\rm n}_{K}$	$c^{\rm g}_{K}$	$c^{\rm e}_{K}$	$c^{\rm n}_{Cl}$	$c^{\rm g}_{Cl}$	$c^{\rm e}_{Cl}$	$\phi_{\rm n}$	$\phi_{\rm g}$
0.8	0.8	0.5054	0.3015	11.3	10.86	139.93	128.64	129.09	3.84	10.08	9.36	119.52	-65.75	-82.78
0.9	0.9	0.5021	0.3007	10.5	10.4	139.95	129.47	129.58	3.6	9.27	9.02	119.81	-68.3	-83.99
1	1	0.5	0.3	10	10	140	130	130	3.4	8.74	8.74	120	-70	-85
1.1	1.1	0.4984	0.2994	9.62	9.66	140.06	130.40	130.36	3.23	8.34	8.51	120.14	-71.34	-85.87
1.2	1.2	0.4971	0.2990	9.30	9.36	140.11	130.73	130.67	3.09	8.02	8.31	120.25	-72.47	-86.63
1.3	1.3	0.4960	0.2985	9.04	9.11	140.16	131.01	130.93	2.96	7.74	8.14	120.35	-73.44	-87.30
1.4	1.4	0.4951	0.2982	8.82	8.88	140.21	131.25	131.17	2.85	7.51	7.99	120.43	-74.30	-87.91
1.5	1.5	0.4943	0.2978	8.62	8.68	140.26	131.46	131.38	2.75	7.30	7.85	120.49	-75.06	-88.45
1	0.7	0.5031	0.3008	9.72	12.21	139.91	130.25	127.76	3.68	9.53	9.06	119.73	-67.32	-83.50
1	0.8	0.5018	0.3004	9.81	11.33	139.95	130.17	128.65	3.57	9.20	8.92	119.85	-68.45	-84.12
1	0.9	0.5008	0.3002	9.91	10.60	139.97	130.09	129.39	3.48	8.94	8.82	119.93	-69.31	-84.61
1	1.1	0.4993	0.2999	10.09	9.49	140.02	129.92	130.52	3.34	8.58	8.69	120.05	-70.57	-85.32
1	1.2	0.4988	0.2997	10.17	9.05	140.04	129.84	130.96	3.28	8.44	8.64	120.10	-71.05	-85.58
1	1.3	0.4983	0.2996	10.25	8.66	140.06	129.77	131.35	3.24	8.32	8.60	120.13	-71.46	-85.80
1	1.4	0.4979	0.2996	10.32	8.33	140.08	129.70	131.69	3.20	8.22	8.57	120.16	-71.82	-85.99
1	1.5	0.4976	0.2995	10.39	8.03	140.09	129.64	131.99	3.16	8.13	8.55	120.19	-72.13	-86.15

Table 3.8: Rest values for different Na^+/K^+ ATPase values with initial membrane potentials $\phi_n = -75$ mV and $\phi_g = -90$ mV, with b_n and b_g denoting the multiplier for the neuronal and glial membranes. All concentrations are in mM and potentials in mV. For all values, we have $\alpha_e = 1 - \alpha_n - \alpha_g$ and $\phi_e = 0$.

b_n	b_g	α_n	α_g	c^n_{Na}	c^g_{Na}	c^e_{Na}	c^n_K	c^g_K	c^e_K	c^n_{Cl}	c^g_{Cl}	c^e_{Cl}	ϕ_n	ϕ_g
0.7	0.7	0.5065	0.3027	11.54	11.22	139.66	128.39	128.71	4.18	8.65	8.38	119.43	-69.85	-85.30
0.8	0.8	0.5032	0.3016	10.88	10.74	139.78	129.08	129.21	3.87	8.05	7.93	119.67	-71.99	-87.11
0.9	0.9	0.5014	0.3007	10.39	10.34	139.90	129.59	129.64	3.61	7.61	7.56	119.86	-73.64	-88.65
1	1	0.5	0.3	10	10	140	130	130	3.4	7.25	7.25	120	-75	-90
1.1	1.1	0.4989	0.2994	9.68	9.70	140.09	130.34	130.31	3.22	6.96	6.99	120.12	-76.15	-91.20
1.2	1.2	0.4979	0.2988	9.40	9.45	140.17	130.62	130.58	3.06	6.72	6.75	120.21	-77.14	-92.27
1.3	1.3	0.4971	0.2983	9.17	9.22	140.24	130.87	130.82	2.93	6.51	6.55	120.29	-78.02	-93.24
1.4	1.4	0.4964	0.2979	8.96	9.02	140.30	131.09	131.04	2.81	6.33	6.37	120.36	-78.80	-94.13
1	0.5	0.5048	0.3021	9.20	14.47	139.71	130.75	125.47	4.05	8.45	8.10	119.53	-70.49	-85.62
1	0.6	0.5033	0.3014	9.39	13.17	139.79	130.57	126.79	3.85	8.08	7.83	119.68	-71.87	-86.93
1	0.7	0.5021	0.3009	9.57	12.13	139.86	130.40	127.84	3.70	7.79	7.63	119.80	-72.93	-87.96
1	0.8	0.5013	0.3005	9.73	11.29	139.92	130.25	128.70	3.58	7.57	7.47	119.88	-73.77	-88.78
1	0.9	0.5006	0.3002	9.87	10.59	139.96	130.12	129.41	3.48	7.40	7.35	119.95	-74.44	-89.45
1	1.1	0.4995	0.2998	10.11	9.50	140.03	129.89	130.51	3.33	7.13	7.17	120.04	-75.47	-90.47
1	1.2	0.4991	0.2996	10.22	9.06	140.06	129.80	130.94	3.28	7.03	7.11	120.08	-75.87	-90.86
1	1.3	0.4988	0.2995	10.31	8.69	140.09	129.71	131.33	3.23	6.94	7.05	120.11	-76.22	-91.21
1	1.4	0.4985	0.2994	10.39	8.35	140.11	129.63	131.66	3.18	6.87	7.00	120.14	-76.52	-91.51
1	1.5	0.4982	0.2993	10.47	8.06	140.13	129.56	131.96	3.14	6.80	6.96	120.16	-76.79	-91.77

compartments, which have the same ion channels and transporters. The neuronal volume fractions are each half of the value given in Table 3.4, while all other resting values are the same. We add the NMDA receptor to the channels used in our other models, so that the neuronal membrane contains the persistent sodium channel, the potassium delayed rectifier, the transient potassium channel, leaks for each of sodium, potassium, and chloride, the Na^+/K^+ ATPase, and the NMDA receptor. The glial membrane is restricted to the potassium inward rectifier, leak channels for sodium and chloride, the Na^+/K^+ ATPase, and the sodium, potassium, and chloride cotransporter. As with the three compartment model, the hydraulic permeability κ_k and stiffness constant S_k are zero, so that there is no fluid flow except across the membrane as a result of osmotic pressure. The simulations using this model are discussed in Chapter 6.

As with the three compartment model, the diffusion coefficient is calculated differently in different compartments. The diffusion coefficients for the neuronal compartments are discussed in detail in Chapter 6. The glial diffusion coefficient was assumed to be proportional to the resting glial volume fraction, while the extracellular diffusion coefficient was assumed to be proportional to the actual extracellular volume fraction, and both the glial and extracellular compartments were scaled by the square of the tortuosity term λ. This resulted in a constant glial diffusion coefficient while the extracellular diffusion coefficient changed with time.

$$D_i^{\mathrm{g}} = 0.25 D_i^* \alpha_{\mathrm{g}}^0 / \lambda^2,$$
$$D_i^{\mathrm{e}} = D_i^* \alpha_{\mathrm{e}} / \lambda^2.$$

The method for determining the initial conditions and parameters for the desired rest state is the same as described for the three compartment model, with the only change, aside from the neuronal volume fractions, being the inclusion of the NMDA receptor in the calculation of the neuronal parameters. In the four compartment model, the parameters varied were the permeabilities of the persistent sodium channel and the NMDA receptor. In all cases the Na^+ leak permeability was determined so that

$\frac{\partial c^{\mathrm{n}}_{\mathrm{Na}}}{\partial t} = 0$ for the given initial conditions and parameter values. Parameter values for a specific choice of the permeabilities of these two channels are given in Table 3.9, where the values are identical for the two neuronal compartments.

3.6 Channel Equations

The individual channel and transporter equations used in our models are given here. Units for $P_i^{k,\mu}$ are in cm/s, and units for $G_i^{k,\mu}$ are in mS/cm^2, with the overall ion flux given in mmol/s.

Persistent sodium (neuron) [47, 64]

$$
\begin{aligned}
\hat{g}^{\mathrm{n,P}}_{\mathrm{Na}} &= m^2 h \\
J^{\mathrm{n,P}}_{\mathrm{Na}} &= P^{\mathrm{n,P}}_{\mathrm{Na}} \frac{F\phi_{\mathrm{ne}}}{RT} \frac{c^{\mathrm{n}}_{\mathrm{Na}} \exp(\frac{F\phi_{\mathrm{ne}}}{RT}) - c^{\mathrm{e}}_{\mathrm{Na}}}{\exp(\frac{F\phi_{\mathrm{ne}}}{RT}) - 1} \\
\frac{dm}{dt} &= \alpha_m(1-m) - \beta_m m \\
\frac{dh}{dt} &= \alpha_h(1-h) - \beta_h h \\
\alpha_m &= \frac{1}{(1+\exp(-(0.143\phi_{\mathrm{ne}} + 5.67)))6} \\
\beta_m &= \frac{1}{(1+\exp(0.143\phi_{\mathrm{ne}} + 5.67))6} \\
\alpha_h &= 5.12 \times 10^{-6} \exp(-(0.056\phi_{\mathrm{ne}} + 2.94)) \\
\beta_h &= \frac{1.6 \times 10^{-4}}{1+\exp(-(0.2\phi_{\mathrm{ne}} + 8))}
\end{aligned}
$$

Table 3.9: Parameter values for the four compartment model.

Parameter	Value	Source
C_{m}	$0.75\ \mu\mathrm{F/cm}^2$	[47, 64]
γ_{n}	3.1924×10^3 1/cm	[a]
γ_{g}	6.3849×10^3 1/cm	[a]
$P_{\mathrm{Na}}^{\mathrm{n,P}}$	2×10^{-5} cm/s [b]	[47, 64]
$P_{\mathrm{K}}^{\mathrm{n,DR}}$	1×10^{-3} cm/s	[47, 64]
$P_{\mathrm{K}}^{\mathrm{n,A}}$	1×10^{-4} cm/s	[47, 64]
$P^{\mathrm{n,NMDA}}$	5×10^{-5} cm/s [b]	[c]
$G_{\mathrm{K}}^{\mathrm{g,IR}}$	13×10^{-2} mS/cm^2	[74]
$G_{\mathrm{Na}}^{\mathrm{n,L}}$	6.2737×10^{-9} mmol/cm^2/s	calculated
$G_{\mathrm{Na}}^{\mathrm{g,L}}$	2.1290×10^{-9} mmol/cm^2/s	calculated
$G_{\mathrm{K}}^{\mathrm{n,L}}$	7×10^{-2} mS/cm^2	[64]
$G_{\mathrm{Cl}}^{\mathrm{n,L}}$	10×10^{-2} mS/cm^2	[47]
$G_{\mathrm{Cl}}^{\mathrm{g,L}}$	5×10^{-2} mS/cm^2	[d]
m_{K}	2×10^{-3} mmol/cm^3	[64]
m_{Na}	7.7×10^{-3} mmol/cm^3	[64]
$\bar{I}_{\mathrm{n}}$	1.5972×10^{-7} mmol/cm^2/s	calculated
$\bar{I}_{\mathrm{g}}$	7.5890×10^{-8} mmol/cm^2/s	calculated
P^{NaKCl}	9.1806×10^{-10} mmol/cm^2/s	calculated
η_{n}	5.4×10^{-5} cm/sec/(mmol/cm^3)	[66]
η_{g}	5.4×10^{-5} cm/sec/(mmol/cm^3)	[66]
D_{Na}^*	1.33×10^{-5} cm^2/sec	[72]
D_{K}^*	1.96×10^{-5} cm^2/sec	[72]
D_{Cl}^*	2.03×10^{-5} cm^2/sec	[72]
λ	1.6	[73]
T	310.15 K	[47]

[a] The glial area of cell membrane per unit volume was taken to be equal to that of the neuron in the three compartment model. The neuronal value in the four compartment value was halved since there were two neuronal compartments.

[b] Values were varied. Calculated values are based on the values given here. Changes to $P^{\mathrm{n,NMDA}}$ will affect $\bar{I}_{\mathrm{n}}$ and $G_{\mathrm{Na}}^{\mathrm{n,L}}$, but we observe that the variation across the full range of values only changes $G_{\mathrm{Na}}^{\mathrm{n,L}}$ by no more than 1×10^{-13} mmol/cm^2/s. Similarly, changes to $P_{\mathrm{Na}}^{\mathrm{n,P}}$ will affect $G_{\mathrm{Na}}^{\mathrm{n,L}}$, and in this case we see variation of up to 3×10^{-10} mmol/cm^2/s.

[c] The NMDA receptor permeability was varied widely and the maximum value used is given here, which is approximately 5000 times that in [63].

[d] Glial Cl^- leak value chosen to ensure that other parameter values were always positive.

Potassium delayed rectifier (neuron) [47, 64]

$$\begin{aligned}
\hat{g}_{\mathrm{K}}^{\mathrm{n,DR}} &= m^2 \\
J_{\mathrm{K}}^{\mathrm{n,DR}} &= P_{\mathrm{K}}^{\mathrm{n,DR}} \frac{F\phi_{\mathrm{ne}}}{RT} \frac{c_{\mathrm{K}}^{\mathrm{n}} \exp(\frac{F\phi_{\mathrm{ne}}}{RT}) - c_{\mathrm{K}}^{\mathrm{e}}}{\exp(\frac{F\phi_{\mathrm{ne}}}{RT}) - 1} \\
\frac{dm}{dt} &= \alpha_m(1-m) - \beta_m m \\
\alpha_m &= \frac{0.016(\phi_{\mathrm{ne}} + 34.9)}{1 - \exp(-0.2(\phi_{\mathrm{ne}} + 34.9))} \\
\beta_m &= 0.25 \exp(-(0.025\phi_{\mathrm{ne}} + 1.25))
\end{aligned}$$

Transient potassium (neuron) [47, 64]

$$\begin{aligned}
\hat{g}_{\mathrm{K}}^{\mathrm{n,A}} &= m^2 h \\
J_{\mathrm{K}}^{\mathrm{n,A}} &= P_{\mathrm{K}}^{\mathrm{n,A}} \frac{F\phi_{\mathrm{ne}}}{RT} \frac{c_{\mathrm{K}}^{\mathrm{n}} \exp(\frac{F\phi_{\mathrm{ne}}}{RT}) - c_{\mathrm{K}}^{\mathrm{e}}}{\exp(\frac{F\phi_{\mathrm{ne}}}{RT}) - 1} \\
\frac{dm}{dt} &= \alpha_m(1-m) - \beta_m m \\
\frac{dh}{dt} &= \alpha_h(1-h) - \beta_h h \\
\alpha_m &= \frac{0.02(\phi_{\mathrm{ne}} + 56.9)}{1 - \exp(-0.1(\phi_{\mathrm{ne}} + 56.9))} \\
\beta_m &= \frac{0.0175(\phi_{\mathrm{ne}} + 29.9)}{\exp(0.1(\phi_{\mathrm{ne}} + 29.9)) - 1} \\
\alpha_h &= 0.016 \exp(-(0.056\phi_{\mathrm{ne}} + 4.61)) \\
\beta_h &= \frac{0.5}{\exp(-(0.2\phi_{\mathrm{ne}} + 11.98)) + 1}
\end{aligned}$$

Potassium inward rectifier (glia) [74, 75]

$$\begin{aligned}
\hat{g}_{\mathrm{K}}^{\mathrm{n,IR}} &= \sqrt{\frac{c_{\mathrm{K}}^{\mathrm{e}}}{3}} \frac{1 + \exp(18.5/42.5)}{1 + \exp((\phi_{\mathrm{ge}} - E_{\mathrm{K}}^{\mathrm{g}} + 18.5)/42.5)} \frac{1 + \exp((-118.6 - 85.2)/44.1)}{1 + \exp((-118.6 + \phi_{\mathrm{ge}})/44.1)} \\
J_{\mathrm{K}}^{\mathrm{n,IR}} &= \frac{G_{\mathrm{K}}^{\mathrm{g,IR}}}{F}(\phi_{\mathrm{ge}} - E_{\mathrm{K}}^{g})
\end{aligned}$$

Leak (neuron, glia) [47, 64]

$$\hat{g}_i^{k,\mathrm{L}} = 1$$
$$J_i^{k,\mathrm{L}} = \frac{G_i^{k,\mathrm{L}}}{z_i F}(\phi_{k\mathrm{e}} - E_i^k)$$

$\mathbf{Na^+/K^+}$ ATPase (neuron, glia) [64]

$$J_k^{\mathrm{ATP}} = \frac{\bar{I}_k}{(1 + m_{\mathrm{K}}/c_{\mathrm{K}}^{\mathrm{e}})^2(1 + m_{\mathrm{Na}}/c_{\mathrm{Na}}^k)^3}$$
$$h_{\mathrm{Na}}^{k,\mathrm{ATP}} = 3I_k^{\mathrm{ATP}}$$
$$h_{\mathrm{K}}^{k,\mathrm{ATP}} = -2I_k^{\mathrm{ATP}}$$

Sodium, potassium, chloride cotransporter (glia) [63]

$$J_k^{\mathrm{NaKCl}} = P^{\mathrm{NaKCl}} \ln\left(\frac{c_{\mathrm{Na}}^{\mathrm{g}} c_{\mathrm{K}}^{\mathrm{g}} (c_{\mathrm{Cl}}^{\mathrm{g}})^2}{c_{\mathrm{Na}}^{\mathrm{e}} c_{\mathrm{K}}^{\mathrm{e}} (c_{\mathrm{Cl}}^{\mathrm{e}})^2}\right)$$
$$h_{\mathrm{Na}}^{k,\mathrm{NaKCl}} = J_k^{\mathrm{NaKCl}}$$
$$h_{\mathrm{K}}^{k,\mathrm{NaKCl}} = J_k^{\mathrm{NaKCl}}$$
$$h_{\mathrm{Cl}}^{k,\mathrm{NaKCl}} = 2J_k^{\mathrm{NaKCl}}$$

NMDA receptor (neuron) [63] (with glutamate dynamics adapted from [63])

$$
\begin{aligned}
\hat{g}^{\mathrm{n,NMDA}} &= y(t)G(\phi_{\mathrm{ne}}) \\
J^{\mathrm{n,NMDA}}_{\mathrm{Na}} &= P^{\mathrm{n,NMDA}}\frac{F\phi_{\mathrm{ne}}}{RT}\frac{c^{\mathrm{n}}_{\mathrm{Na}}\exp(\frac{F\phi_{\mathrm{ne}}}{RT})-c^{\mathrm{e}}_{\mathrm{Na}}}{\exp(\frac{F\phi_{\mathrm{ne}}}{RT})-1} \\
J^{\mathrm{n,NMDA}}_{\mathrm{K}} &= P^{\mathrm{n,NMDA}}\frac{F\phi_{\mathrm{ne}}}{RT}\frac{c^{\mathrm{n}}_{\mathrm{K}}\exp(\frac{F\phi_{\mathrm{ne}}}{RT})-c^{\mathrm{e}}_{\mathrm{K}}}{\exp(\frac{F\phi_{\mathrm{ne}}}{RT})-1} \\
\frac{dy}{dt} &= 72\frac{[\mathrm{Glu}]_{\mathrm{e}}}{[\mathrm{Glu}]_{\mathrm{e}}+0.05}(1-y)-6.6y \\
G(\phi) &= \frac{1}{1+0.28e^{-0.062\phi}} \\
\frac{d(\alpha_{\mathrm{e}}[\mathrm{Glu}]_{\mathrm{e}})}{dt} &= \sum_{k=\mathrm{n}_1,\mathrm{n}_2}\left(A\alpha_k\frac{[\mathrm{Glu}]_k}{\epsilon+[\mathrm{Glu}]_k}e^{-0.0044(\phi_{k\mathrm{e}}-8.66)^2}\right)-B\alpha_{\mathrm{e}}[\mathrm{Glu}]_{\mathrm{e}} \\
\frac{d(\alpha_{\mathrm{n}_1}[\mathrm{Glu}]_{\mathrm{n}_1})}{dt} &= -A\alpha_{\mathrm{n}_1}\frac{[\mathrm{Glu}]_{\mathrm{n}_1}}{\epsilon+[\mathrm{Glu}]_{\mathrm{n}_1}}e^{-0.0044(\phi_{\mathrm{n}_1\mathrm{e}}-8.66)^2}+\frac{\nu}{2}B\alpha_{\mathrm{e}}[\mathrm{Glu}]_{\mathrm{e}} \\
\frac{d(\alpha_{\mathrm{n}_2}[\mathrm{Glu}]_{\mathrm{n}_2})}{dt} &= -A\alpha_{\mathrm{n}_2}\frac{[\mathrm{Glu}]_{\mathrm{n}_2}}{\epsilon+[\mathrm{Glu}]_{\mathrm{n}_2}}e^{-0.0044(\phi_{\mathrm{n}_2\mathrm{e}}-8.66)^2}+\frac{\nu}{2}B\alpha_{\mathrm{e}}[\mathrm{Glu}]_{\mathrm{e}} \\
\frac{d(\alpha_{\mathrm{g}}[\mathrm{Glu}]_{\mathrm{g}})}{dt} &= (1-\nu)B\alpha_{\mathrm{e}}[\mathrm{Glu}]_{\mathrm{e}}.
\end{aligned}
$$

3.7 Triggering SD

In all one-dimensional cases, SD was triggered by adding excitatory transmembrane fluxes for all ions to the neuronal compartment at the left-most point, similar to the manner done in [68]. The excitatory fluxes were of the form

$$j_{iE} = G_E(t,x)\left(z_iF\phi_{\mathrm{ne}} - RT\ln\left(\frac{c^{\mathrm{e}}_i}{c^{\mathrm{n}}_i}\right)\right), \tag{3.28}$$

$$G_E(t,x) = \begin{cases} G_{max}\cos^2(\pi x/(2x_E))\sin(\pi t/t_E) & \text{if } 0\le x<x_E \text{ and } 0\le t\le t_E, \\ 0 \quad \text{otherwise.} \end{cases} \tag{3.29}$$

We set $x_E = \triangle x$, $t_E = 2$ s and $G_{max}F^2 = 0.5$ mS/cm^2, where $\triangle x$ is the size of our discretization (see section 3.8). The excitatory fluxes result in a nonselective membrane

conductance that opens at the left edge for two seconds. With $x_E = \triangle x$, only one discretization point is affected by this conductance.

In the two-dimensional simulations, SD was triggered by adding excitatory transmembrane fluxes for all ions to the neuronal compartment in one corner. Similar to the one-dimensional version, the excitatory fluxes were given by

$$j_{iE} = G_E(t,x,y)\left(z_i F\phi_{\rm ne} - RT\ln\left(\frac{c_i^{\rm e}}{c_i^{\rm n}}\right)\right), \tag{3.30}$$

$$G_E(t,x,y) = \begin{cases} G_{max}\cos^2(\pi x/(2x_E))\cos^2(\pi y/(2y_E))\sin(\pi t/t_E) \\ \quad \text{if } 0 \le x < x_E,\ 0 \le y < y_E, \text{ and } 0 \le t \le t_E, \\ 0 \quad \text{otherwise.} \end{cases} \tag{3.31}$$

For the two-dimensional simulations, $t_E = 2$ s, $G_{max}F^2 = 5$ mS/cm^2, and x_E and y_E are each 0.5 mm.

Finally, in some two-dimensional simulations, we also triggered SD in a second region. For this second trigger, centered at $(5,0)$, we have

$$G_E(t,x,y) = \begin{cases} G_{max}\cos^2(\pi(x-5)/(2x_E))\cos^2(\pi y/(2y_E))\sin(\pi t/t_E) \\ \quad \text{if } 5 - x_E \le x < 5 + x_E,\ 0 \le y < y_E, \text{ and } 0 \le t \le t_E, \\ 0 \quad \text{otherwise,} \end{cases} \tag{3.32}$$

with all constants the same as at the corner.

3.8 Numerical Computation

To turn this into a numerical model, we use a finite difference method. We let $\triangle x$ and $\triangle t$ be the width of our spatial and temporal discretizations, respectively, with X and T the total number of points in space and time. For $l = 1, \cdots, X$ we let $z_{k,l}^n$ approximate z_k at $x = (l-1/2)\triangle x$ and $t = n\triangle t$, where z represents any of our dependent variables. In this manner, each region of size $\triangle x$ is given by its approximate value in the center

of the region. For notational simplicity, we let

$$\mathcal{D}_x^+(z_{k,l}^n) = \frac{1}{\triangle x}(z_{k,l+1}^n - z_{k,l}^n), \tag{3.33}$$

$$\mathcal{D}_x^-(z_{k,l}^n) = \frac{1}{\triangle x}(z_{k,l}^n - z_{k,l-1}^n), \tag{3.34}$$

$$\mathcal{D}_t^-(z_{k,l}^n) = \frac{1}{\triangle t}(z_{k,l}^n - z_{k,l}^{n-1}) \tag{3.35}$$

denote our difference operators. In the context of two spatial dimensions, we have $\triangle y$ denoting the width of the spatial discretization in the second dimension, with Y total points, and let $z_{k,l,m}^n$ be our approximation of z_k at $x = (l-1/2)\triangle x$, $y = (m-1/2)\triangle y$, and $t = n\triangle t$, with $\mathcal{D}_y^+$ and $\mathcal{D}_y^-$ the natural parallel to $\mathcal{D}_x^+$ and $\mathcal{D}_x^-$. For this, the approximation is in the center of the rectangular region of size $\triangle x$ by $\triangle y$.

The discretization is designed to be a hybrid of the forward and backward Euler methods, treating the intercompartmental flow implicitly and the intracompartmental flow explicitly. The gating variables are treated explicitly, and the ion flux term is also partially explicit. We define α_k, c_i^k, ϕ_k, and p_k at the midpoints of intervals and u_k at the endpoints of the intervals. We note that since the flow rate u_k and the diffusion coefficient are approximated at the boundary between regions, rather than the center of the region, they are indexed by $l+1/2$ and $m+1/2$. Furthermore, with these definitions, our discretization does not specify α_k, c_i^k, ϕ_k, or p_k at the endpoints of the domain. For simplicity, however, we will refer to the edges of the domain as 0 and 10 (in mm), with the understanding that the discretization uses the closest points, $\triangle x/2$ and $10 - \triangle x/2$ respectively, to represent these points.

3.8.1 One-Dimensional Computations without Fluid Flow

Though much of the discretization is the same with and without fluid flow, we present first the discretization without fluid flow. Noting that (3.2) is an immediate consequence

of (3.3) and (3.4), our discretized equations are

$$\mathcal{D}_t^-(\alpha_{k,l}^n) = -\gamma_k w_{k,l}^n, \quad k = 1, \cdots, N-1, \tag{3.36}$$

$$\sum_{k=1}^{N} \alpha_{k,l}^n = 1, \tag{3.37}$$

with

$$w_{k,l}^n = -\eta_k RT \left(\frac{a_{k,l}}{\alpha_{k,l}^n} - \frac{a_{N,l}}{\alpha_{N,l}^n} + \sum_{i=1}^{M} (c_{i,l}^{k,n} - c_{i,l}^{N,n}) \right). \tag{3.38}$$

For the ions, we have

$$\mathcal{D}_t^-(\alpha_{k,l}^n c_{i,l}^{k,n}) = -\mathcal{D}_x^-(f_{i,l+1/2}^{k,n}) - \gamma_k j_{i,l}^{k,n}, \tag{3.39}$$

$$\mathcal{D}_t^-(\alpha_{N,l}^n c_{i,l}^{N,n}) = -\mathcal{D}_x^-(f_{i,l+1/2}^{N,n}) + \sum_{k=1}^{N-1} \gamma_k j_{i,l}^{k,n}, \tag{3.40}$$

where (3.39) applies for $k = 1, \cdots, N-1$, and

$$f_{i,l+1/2}^{k,n} = -D_{i,l+1/2}^{k,n-1} \frac{c_{i,l+1}^{k,n-1} + c_{i,l}^{k,n-1}}{2} \mathcal{D}_x^+ \left(\ln(c_{i,l}^{k,n}) + \frac{z_i F}{RT} \phi_{k,l}^n \right) \tag{3.41}$$

for all k. To satisfy the no-flux boundary conditions, we define $f_{i,1/2}^{k,n} = 0$ and $f_{i,X+1/2}^{k,n} = 0$ for all k and n. For $j_{i,l}^{k,n}$, we use the equations in section 3.6, treating the active flux and gating variables explicitly, and everything else implicitly, so that

$$j_{i,l}^{k,n} = \sum_{\mu} h_{i,l}^{k,\mu,n-1} + \sum_{\mu} \hat{g}_{i,l}^{k,\mu,n-1} J_{i,l}^{k,\mu,n}. \tag{3.42}$$

Note that, since J is an algebraic function of the concentrations and voltages, $J_{i,l}^{k,\mu,n}$ is $J_i^{k,\mu}(c_{i,l}^{k,n}, c_{i,l}^{N,n}, \phi_{kN,l}^n)$. A similar equation holds for $h_{i,l}^{k,\mu,n-1}$, which is also algebraic and evaluated at $n-1$ for all variables. The computation of the gating variables is discussed in 3.8.4.

The electrostatic potential satisfies

$$\gamma_k C_{\mathrm{m}}^k \phi_{kN,l}^n = \rho_0^k + \sum_{i=1}^{M} z_i F \alpha_{k,l}^n c_{i,l}^{k,n}, \quad k = 1, \cdots, N-1, \tag{3.43}$$

$$-\sum_{k=1}^{N-1} \gamma_k C_{\mathrm{m}}^k \phi_{kN,l}^n = \rho_0^N + \sum_{i=1}^{M} z_i F \alpha_{N,l}^n c_{i,l}^{N,n}. \tag{3.44}$$

In order to implement this model, we use the following algorithm.

For n=1 to EndTime:

Compute $\alpha_{k,l}^n$ $(k = 1, \cdots, N-1)$, $c_{i,l}^{k,n}$, and $\phi_{k,l}^n$ by using Jacobi iterations to approximate the solution to the non-linear system in (3.36), (3.38) and (3.39)–(3.44).

Compute $\alpha_{N,l}^n$ using (3.37).

Compute the gating variables (see section 3.8.4).

If including NMDA receptors, compute the glutamate concentration.

End

For this model, we take $\triangle x = 0.02$ mm and $\triangle t = 0.01$ s.

3.8.2 One-Dimensional Computations with Fluid Flow

Incorporating fluid flow requires a careful treatment to ensure stability, as the system has an advective term that requires upwinding as well as reaction and diffusion. Because of the definition of **u** as a potential flow, the advective terms appear only as a connection between ionic electrodiffusion and volume fraction. Ions travel with the flow as well as through electrodiffusion, so the flow is, in turn, affected by electrodiffusion. Aside from that, however, the effects of fluid flow require implicit treatment as the pressure term has a diffusive effect. To accomplish this, we decouple the ion concentration and electrostatic potential equations from the volume fraction, flow, and pressure. To simplify the discussion, we define

$$a_{i,l}^{k,n} = \alpha_{k,l}^n c_{i,l}^{k,n} \tag{3.45}$$

to be the total amount of each ion. Solving for $a_{i,l}^{k,n}$ and $\alpha_{k,l}^n$ is equivalent to solving for $c_{i,l}^{k,n}$ and $\alpha_{k,l}^n$ as long as $\alpha_{k,l}^n$ is not zero.

We start with the equations for the ions and the electrostatic potential. The ions

satisfy

$$\mathcal{D}_t^-(a_{i,l}^{k,n}) + v_{i,l}^{k,n-1} = -\mathcal{D}_x^-(f_{i,l+1/2}^{k,n}) - \gamma_k j_{i,l}^{k,n}, \tag{3.46}$$

$$\mathcal{D}_t^-(a_{i,l}^{N,n}) + v_{i,l}^{N,n-1} = -\mathcal{D}_x^-(f_{i,l+1/2}^{N,n}) + \sum_{k=1}^{N-1} \gamma_k j_{i,l}^{k,n}, \tag{3.47}$$

where (3.46) applies for $k = 1, \cdots, N-1$, and

$$v_{i,l}^{k,n} = \begin{cases} \mathcal{D}_x^-(a_{i,l}^{k,n-1} u_{k,l+1/2}^{n-1}) & \text{if } u_{k,l+1/2}^{n-1} > 0, \\ \mathcal{D}_x^+(a_{i,l}^{k,n-1} u_{k,l-1/2}^{n-1}) & \text{otherwise} \end{cases} \tag{3.48}$$

$$f_{i,l+1/2}^{k,n} = -D_{i,l+1/2}^{k,n-1} \frac{c_{i,l+1}^{k,n-1} + c_{i,l}^{k,n-1}}{2} \mathcal{D}_x^+ \left(\ln\left(\frac{a_{i,l}^{k,n}}{\alpha_{k,l}^{n-1}} \right) + \frac{z_i F}{RT} \phi_{k,l}^n \right) \tag{3.49}$$

for all k. To satisfy the no-flux boundary conditions, we define $f_{i,1/2}^{k,n} = 0$ and $f_{i,X+1/2}^{k,n} = 0$ for all k and n. For $j_{i,l}^{k,n}$, we use the equations in section 3.6, where we treat the active flux and gating variables explicitly, and everything else implicitly, so that

$$j_{i,l}^{k,n} = \sum_{\mu} h_{i,l}^{k,\mu,n-1} + \sum_{\mu} \hat{g}_{i,l}^{k,\mu,n-1} J_{i,l}^{k,\mu,n}. \tag{3.50}$$

The definitions of $J_{i,l}^{k,\mu,n}$ and $h_{i,l}^{k,\mu,n-1}$ are the same as without fluid flow, as are the gating variables, which are further discussed in section 3.8.4.

The electrostatic potential is

$$\gamma_k C_{\mathrm{m}}^k \phi_{kN,l}^n = \rho_0^k + \sum_{i=1}^{M} z_i F a_{i,l}^{k,n}, \quad k = 1, \cdots, N-1, \tag{3.51}$$

$$-\sum_{k=1}^{N-1} \gamma_k C_{\mathrm{m}}^k \phi_{kN,l}^n = \rho_0^N + \sum_{i=1}^{M} z_i F a_{i,l}^{N,n}. \tag{3.52}$$

With these discretizations, the ions and electrostatic potential only depend on the volume fraction, pressure, and flow explicitly.

We then discretize the equations for the volume fraction and pressure. For volume fraction, we have

$$\mathcal{D}_t^-(\alpha_{k,l}^n) - \mathcal{D}_x^- \left(\kappa_k \mathcal{D}_x^+ \left(p_{k,l}^n - RT \frac{a_{k,l}}{\alpha_{k,l}^n} \right) \right) + \sigma_{k,l}^n - \kappa_k \sum_{i=1}^{M} z_i F \frac{a_{i,l}^{k,n}}{\alpha_{k,l}^n} \mathcal{D}_x^- \mathcal{D}_x^+ \phi_{k,l}^n = -w_{k,l}^n, \tag{3.53}$$

$$\sum_{k=1}^{N} \alpha_{k,l}^{n} = 1, \tag{3.54}$$

where

$$\sigma_{k,l}^{n} = \begin{cases} D_x^- \left(-\kappa_k \sum_{i=1}^{M} z_i F \frac{a_{i,l}^{k,n}}{\alpha_{k,l}^{n-1}} \right) D_x^-(\phi_{k,l}^n) & \text{if } \bar{\sigma}_{k,l}^n > 0, \\ D_x^+ \left(-\kappa_k \sum_{i=1}^{M} z_i F \frac{a_{i,l}^{k,n}}{\alpha_{k,l}^{n-1}} \right) D_x^+(\phi_{k,l}^n) & \text{otherwise,} \end{cases} \tag{3.55}$$

$$\bar{\sigma}_{k,l}^{n} = D_x^- \left(-\kappa_k \sum_{i=1}^{M} z_i F \frac{a_{i,l}^{k,n}}{(\alpha_{k,l}^{n,}-1)^2} \right) D_x^-(\phi_{k,l}^n) \tag{3.56}$$

and

$$w_{k,l}^{n} = \gamma_k \eta_k \left(S_k(\alpha_{k,l}^n - \alpha_k^0) - RT \left(\frac{a_{k,l}}{\alpha_{k,l}^n} - \frac{a_{N,l}}{\alpha_{N,l}^n} + \sum_{i=1}^{M} \left(\frac{a_{i,l}^{k,n}}{\alpha_{k,l}^n} - \frac{a_{i,l}^{N,n}}{\alpha_{N,l}^n} \right) \right) \right). \tag{3.57}$$

The pressure equations are, for $k = 1, \cdots, N-1$,

$$p_{k,l}^n = S_k(\alpha_{k,l}^n - \alpha_{k,l}^0) + p_{N,l}^n, \tag{3.58}$$

and the incompressibility condition for $k = N$

$$\sum_{k=1}^{N} \left(\mathcal{D}_x^- \left(-\kappa_k \mathcal{D}_x^+ \left(p_{k,l}^n - RT \frac{a_{k,l}}{\alpha_{k,l}^n} \right) \right) + \sigma_{k,l}^n - \kappa_k \sum_{i=1}^{M} z_i F \frac{a_{i,l}^{k,n}}{\alpha_{k,l}^n} \mathcal{D}_x^- \mathcal{D}_x^+ \phi_{k,l}^n \right) = 0. \tag{3.59}$$

For fluid flow, we have

$$u_{k,l+1/2}^{n} = -\frac{2\kappa_k}{\alpha_{k,l+1}^n + \alpha_{k,l}^n} \left(\mathcal{D}_x^+ \left(p_{k,l}^n - RT \frac{a_{k,l}}{\alpha_{k,l}^n} \right) + \sum_{i=1}^{M} z_i F \frac{c_{k,l+1}^n + c_{k,l}^n}{2} \mathcal{D}_x^+ \phi_{k,l}^n \right). \tag{3.60}$$

In order to implement this model, we use the following algorithm.

For n=1 to EndTime:

Compute $a_{i,l}^{k,n}$ and $\phi_{k,l}^n$ by using Jacobi iterations to approximate the solution to the non-linear system in (3.46)–(3.52).

Compute $\alpha_{k,l}^n$ ($k = 1, \cdots, N-1$) and $p_{k,l}^n$ by using Jacobi iterations to approximate

the solution to the non-linear system in (3.53) and (3.55)–(3.59).

Compute $\alpha^n_{N,l}$ using (3.54) and $c^{k,n}_{i,l}$ using (3.45).

Compute $u^n_{k,l+1/2}$ $(k = 1, \cdots, N)$ using (3.60).

Compute the gating variables (see section 3.8.4).

End

For this model, we take $\triangle x = 0.02$ mm and $\triangle t = 0.01$ s.

3.8.3 Two-Dimensional Computations

The two-dimensional discretization is the natural analog of the one-dimensional discretization.

$$\mathcal{D}^-_t(\alpha^n_{k,l,m}) = -\gamma_k w^n_{k,l,m}, \quad k = 1, \cdots, N-1, \tag{3.61}$$

$$\sum_{k=1}^{N} \alpha^n_{k,l,m} = 1, \tag{3.62}$$

with

$$w^n_{k,l,m} = -\eta_k RT \left(\frac{a_{k,l,m}}{\alpha^n_{k,l,m}} - \frac{a_{N,l,m}}{\alpha^n_{N,l,m}} + \sum_{i=1}^{M} (c^{k,n}_{i,l,m} - c^{N,n}_{i,l,m}) \right). \tag{3.63}$$

For the ions, we have

$$\mathcal{D}^-_t(\alpha^n_{k,l,m} c^{k,n}_{i,l,m}) = -\mathcal{D}^-_x(f^{k,n}_{i,l+1/2,m}) - \mathcal{D}^-_y(f^{k,n}_{i,l,m+1/2}) - \gamma_k j^{k,n}_{i,l,m}, \tag{3.64}$$

$$\mathcal{D}^-_t(\alpha^n_{N,l} c^{N,n}_{i,l}) = -\mathcal{D}^-_x(f^{N,n}_{i,l+1/2,m}) - \mathcal{D}^-_y(f^{N,n}_{i,l,m+1/2}) + \sum_{k=1}^{N-1} \gamma_k j^{k,n}_{i,l,m}, \tag{3.65}$$

where (3.64) applies for $k = 1, \cdots, N-1$, and

$$f^{k,n}_{i,l+1/2,m} = -D^{k,n-1}_{i,l+1/2,m} \frac{c^{k,n-1}_{i,l+1,m} + c^{k,n-1}_{i,l,m}}{2} \mathcal{D}^+_x \left(\ln(c^{k,n}_{i,l,m}) + \frac{z_i F}{RT} \phi^n_{k,l,m} \right), \tag{3.66}$$

$$f^{k,n}_{i,l,m+1/2} = -D^{k,n-1}_{i,l,m+1/2} \frac{c^{k,n-1}_{i,l,m+1} + c^{k,n-1}_{i,l,m}}{2} \mathcal{D}^+_y \left(\ln(c^{k,n}_{i,l,m}) + \frac{z_i F}{RT} \phi^n_{k,l,m} \right) \tag{3.67}$$

for all k. To satisfy the no-flux boundary conditions, we define $f^{k,n}_{i,1/2,m} = 0$ and $f^{k,n}_{i,X+1/2,m} = 0$ for all m, k, and n, and $f^{k,n}_{i,l,1/2} = 0$ and $f^{k,n}_{i,l,Y+1/2} = 0$ for all l, k, and n. For $j^{k,n}_{i,l,m}$, we again use the equations in section 3.6, treating the active flux and gating variables explicitly, and everything else implicitly, so that

$$j^{k,n}_{i,l,m} = \sum_{\mu} h^{k,\mu,n-1}_{i,l,m} + \sum_{\mu} \hat{g}^{k,\mu,n-1}_{i,l,m} J^{k,\mu,n}_{i,l,m}. \tag{3.68}$$

Here, $J^{k,\mu,n}_{i,l,m}$, $h^{k,\mu,n-1}_{i,l,m}$ and the gating variables are the natural extension of those described in the one dimensional model.

The electrostatic potential satisfies

$$\gamma_k C^k_{\mathrm{m}} \phi^n_{kN,l,m} = \rho^k_0 + \sum_{i=1}^{M} z_i F \alpha^n_{k,l,m} c^{k,n}_{i,l,m}, \quad k = 1, \cdots, N-1, \tag{3.69}$$

$$-\sum_{k=1}^{N-1} \gamma_k C^k_{\mathrm{m}} \phi^n_{kN,l,m} = \rho^N_0 + \sum_{i=1}^{M} z_i F \alpha^n_{N,l,m} c^{N,n}_{i,l,m}. \tag{3.70}$$

The algorithm used to solve the two-dimensional simulations is the same as the one used to solve the one-dimensional simulations without fluid flow.

For this model, we take $\triangle x = \triangle y = 0.1$ mm and $\triangle t = 0.01$ s.

3.8.4 Gating Variables and Glutamate

For the gating variables which satisfy the ordinary differential equation (ODE) given in 3.22, we use the same method for all computational routines. Since the gating variables are incorporated into the ion flux equations explicitly, we leave their computation at each time step until after everything else has been computed. We therefore use the backward Euler discretization:

$$\mathcal{D}^-_t(s^n_{k,l}) = \frac{s_\infty(\phi^n_{kN,l}) - s^n_{k,l}}{\tau_s(\phi^n_{kN,l})} \tag{3.71}$$

The gating variable for the potassium inward rectifier is governed by an algebraic

equation that is a function of the intracellular and extracellular potassium concentrations and the membrane potential, and is thus given by

$$\hat{g}_{\mathrm{K},l}^{\mathrm{n,IR},n} = \hat{g}_{\mathrm{K}}^{\mathrm{n,IR}}(c_{\mathrm{K},l}^{\mathrm{g},n}, c_{\mathrm{K},l}^{\mathrm{e},n}, \phi_{\mathrm{ge},l}^{n}) \tag{3.72}$$

The NMDA receptor has two gating variables, one of which is governed by an ODE dependent on the glutamate concentration. The other is an algebraic equation that is a function of the membrane potential. We discretize the differential equation using forward Euler:

$$\mathcal{D}_t^-(y_l^n) = 72\frac{[\mathrm{Glu}]_{\mathrm{e},l}^{n-1}}{[\mathrm{Glu}]_{\mathrm{e},l}^{n-1} + 0.05}(1 - y_l^{n-1}) - 6.6y_l^{n-1} \tag{3.73}$$

$$G_l^n = G(\phi_{\mathrm{ne,l}}^n) \tag{3.74}$$

It is also necessary to discretize the equations governing the glutamate dynamics. Since we ignore the diffusion of glutamate, these equations are ODEs, and we use the following discretization to determine the values. Note that $\phi_{k\mathrm{e}}^n$ and α_k^n are known when $[\mathrm{Glu}]_k^n$ is computed.

$$\mathcal{D}_t^-(\alpha_{\mathrm{e}}^n[\mathrm{Glu}]_{\mathrm{e}}^n)) = \sum_{k=\mathrm{n}_1,\mathrm{n}_2}\left(A\alpha_k^n\frac{[\mathrm{Glu}]_k^n}{\epsilon + [\mathrm{Glu}]_k^{n-1}}e^{-0.0044(\phi_{k\mathrm{e}}^n - 8.66)^2}\right) - B\alpha_{\mathrm{e}}^n[\mathrm{Glu}]_{\mathrm{e}}^{\mathrm{n}} \tag{3.75}$$

$$\mathcal{D}_t^-(\alpha_{\mathrm{n}_1}^n[\mathrm{Glu}]_{\mathrm{n}_1}^n) = -A\alpha_{\mathrm{n}_1}^n\frac{[\mathrm{Glu}]_{\mathrm{n}_1}^n}{\epsilon + [\mathrm{Glu}]_{\mathrm{n}_1}^{n-1}}e^{-0.0044(\phi_{\mathrm{n}_1\mathrm{e}}^n - 8.66)^2} + \frac{\nu}{2}B\alpha_{\mathrm{e}}^n[\mathrm{Glu}]_{\mathrm{e}}^{\mathrm{n}} \tag{3.76}$$

$$\mathcal{D}_t^-(\alpha_{\mathrm{n}_2}^n[\mathrm{Glu}]_{\mathrm{n}_2}^n) = -A\alpha_{\mathrm{n}_2}^n\frac{[\mathrm{Glu}]_{\mathrm{n}_2}^n}{\epsilon + [\mathrm{Glu}]_{\mathrm{n}_2}^{n-1}}e^{-0.0044(\phi_{\mathrm{n}_2\mathrm{e}}^n - 8.66)^2} + \frac{\nu}{2}B\alpha_{\mathrm{e}}^n[\mathrm{Glu}]_{\mathrm{e}}^{\mathrm{n}} \tag{3.77}$$

$$\mathcal{D}_t^-(\alpha_{\mathrm{g}}^n[\mathrm{Glu}]_{\mathrm{g}}^n) = (1-\nu)B\alpha_{\mathrm{e}}^n[\mathrm{Glu}]_{\mathrm{e}}^{\mathrm{n}}. \tag{3.78}$$

3.9 Energy Identity

The system given by equations (3.1)–(3.13) and (3.25)–(3.27) satisfies a free energy identity [68], where the free energy is the sum of several kinds of energy. Each cell type

has an elastic energy, related to the pressure and stiffness of the cell membrane, and an electrical energy from the membrane serving as a capacitor. In addition, the ions contribute entropic free energy. The rate of change in energy is given by electrodiffusive dissipation and flow within each compartment and the transmembrane flux of both water and ions.

Specifically, the solutions to these equations satisfy the following free energy identity [68], under no-flux boundary conditions on the domain Ω:

$$\begin{aligned}
\frac{dG}{dt} &= -I_{\text{bulk}} - I_{\text{mem}}, \\
G &= \int_\Omega \left(\mathcal{E} + \sum_{k=1}^{N} \left(RT \left(a_k \ln\left(\frac{a_k}{\alpha_k}\right) + \sum_{i=1}^{M} \alpha_k c_i^k \ln c_i^k \right) \right) + \sum_{k=1}^{N-1} \frac{1}{2} \gamma_k C_{\text{m}} \phi_{kN}^2 \right) d\mathbf{x}, \\
I_{\text{bulk}} &= \int_\Omega \left(\sum_{k=1}^{N} \left(\alpha_k \zeta_k |\mathbf{u}_k|^2 + \sum_{i=1}^{M} \frac{D_i^k c_i^k}{RT} |\nabla \mu_i^k|^2 \right) \right) d\mathbf{x}, \\
I_{\text{mem}} &= \int_\Omega \left(\sum_{k=1}^{N-1} \gamma_k \left(\psi_k w_k + \sum_{i=1}^{M} \mu_i^{k\text{N}} j_i^k \right) \right) d\mathbf{x},
\end{aligned} \tag{3.79}$$

where

$$\begin{aligned}
\mu_i^k &= RT(\ln c_i^k + 1) + z_i F \phi_k, \\
\mu_i^{kN} &= \mu_i^k - \mu_i^N, \\
\psi_{kN} &= p_{kN} - \pi_{kN}.
\end{aligned} \tag{3.80}$$

Note that in this, G is the free energy, and the rate of free energy change is split into a bulk term I_{bulk} and the membrane term I_{mem}. The bulk term consists of energy dissipation through ionic electrodiffusion and intracompartmental fluid flow, while the membrane term is a combination of dissipation of elastic energy through transmembrane water flow and both dissipation and input of energy through ion channels and pumps. A related energy inequality exists for the discretization without fluid flow [68].

Chapter 4

Incorporating Fluid Flow

As discussed in section 3.3, we consider two compartments, with $k = \mathrm{n}$ representing the intracellular compartment and $k = \mathrm{e}$ the extracellular compartment, and three ion species, namely Na^+, K^+, and Cl^-, over a 1 cm-wide domain. We examine the effects of the hydraulic permeability κ_k of both compartments and the stiffness constant S_n on the propagation speed of SD and the shape of the wave, with SD triggered at the left edge as described in section 3.7.

The results of the simulations have a propagating wave of concentration changes, with extracellular K^+ increasing abruptly and Na^+ and Cl^- decreasing, followed by gradual relaxation of all three ions to their original values. These changes are a result of flow across the membrane and correspond to changes in the opposite direction within the cell. The changes in concentration result in depolarization followed by hyperpolarization, with ϕ_ne shifting rapidly from near -70 mV to close to 0 mV, then dropping back more gradually to near its original value. Additionally, the concentration changes lead to a change in osmotic pressure, resulting in temporary cell swelling. The changes are similar to those discussed in Chapter 2. Furthermore, we see slight overshoots of the extracellular potential and extracellular K^+ concentration during the recovery phase, with the potential reaching 0.36 mV and extracellular K^+ dropping past 4.05 mM to

2.83 mM. Such overshoots have been seen in many experiments [13, 28, 29, 31, 76, 77].

4.1 Hydraulic Permeability

The significance of adding fluid flow to this system will, of course, depend on the flow rate. If κ_k is small, we expect slow flow, which will likely not significantly impact the dynamics of the system relative to that of no flow. For sufficiently high values of κ_k, we expect that the speed of the propagation might change as the flow may either carry or slow the wave. We ran simulations with the hydraulic permeability in each compartment equal to 0, 5×10^{-9}, and 5×10^{-7} cm^4/dynes/sec and with the stiffness constant S_n set to 0. We found that in order for any significant intracompartmental flow to occur, both compartments must have a non-zero hydraulic permeability. This is an immediate consequence of the incompressibility condition and no-flux boundary conditions in one dimension. If one compartment has no hydraulic permeability, any change in volume fraction can only occur through transmembrane flux. If we assume incompressibility, the only way for flow to happen in one dimension without changing the volume fraction is if it is constant in the compartment. With no-flux boundary conditions, this requires no flow at all. Mathematically, if $\kappa_k = 0$ for one compartment, we will have $\frac{\partial(\alpha_k \mathbf{u}_k)}{\partial x} = 0$ for the other compartment, and therefore $\alpha_k \mathbf{u}_k$ is constant, and the no-flux condition forces $\alpha_k \mathbf{u}_k = 0$. Finally, since $\alpha_k \neq 0$, $\mathbf{u}_k = 0$. Note that this may not be true in higher spatial dimensions, as $\nabla \cdot (\alpha_k \mathbf{u}_k) = 0$ does not necessarily mean that $\alpha_k \mathbf{u}_k = 0$.

As expected, with $\kappa_\mathrm{n} = \kappa_\mathrm{e} = 5 \times 10^{-9}$ cm^4/dynes/sec, fluid flow had minimal impact on the system. We compare the results with no flow and $\kappa_\mathrm{n} = \kappa_\mathrm{e} = 5 \times 10^{-9}$, and in both cases the propagation speed was 3.8 mm/min. Differences in the voltages were on the order of 0.1 mV, while differences in the concentrations were on the order of 1 mM. Volume fractions were within 1×10^{-4} of each other. Fig. 4.1 shows the concentrations, voltages, and volume fractions for the simulation with $\kappa_\mathrm{n} = \kappa_\mathrm{e} = 0$, while Fig. 4.2 shows the concentrations, voltages, volume fractions, pressures, and flow

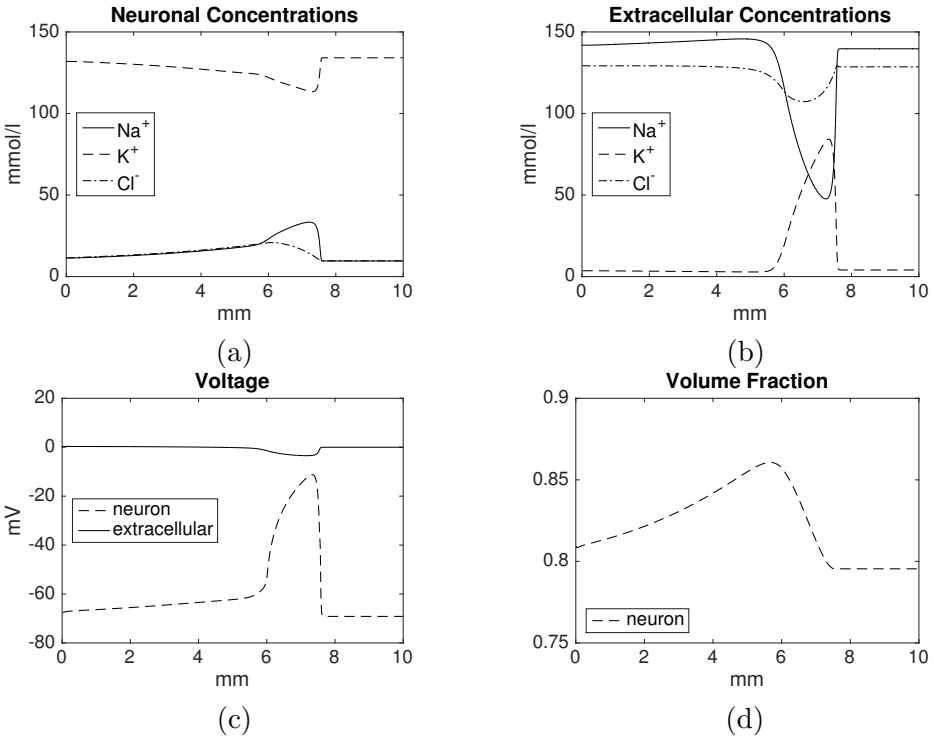

Figure 4.1: The model without fluid flow ($\kappa_{\mathrm{n}} = 0$ or $\kappa_{\mathrm{e}} = 0$) after 240 seconds of simulated time. (a) Concentrations in the neuronal compartment are Na^+ (solid line), K^+ (dashed line), and Cl^- (dashed and dotted line). (b) Concentrations for the same ion species in the extracellular space. (c) The voltage for both compartments, with the solid line showing the neuronal and dashed the extracellular. (d) The volume fraction graph shows the neuronal volume fraction only. The extracellular volume fraction is one minus the neuronal volume fraction.

rates for $\kappa_{\mathrm{n}} = \kappa_{\mathrm{e}} = 5 \times 10^{-9}$ cm^4/dynes/sec, both after two minutes of simulated time. We observe that flow occurs at a rate of up to slightly more than 3×10^{-9} cm/sec in the neuronal compartment and up to 13×10^{-9} cm/sec in the extracellular compartment. We make the additional observation that the two flows are always in opposite direction and that the ratio of the flow rates in the two compartments is the inverse of the ratio of volume fractions. This is, again, an immediate consequence of the incompressibility condition in one dimension.

We observe that the direction of flow follows a logical pattern. During cell swelling,

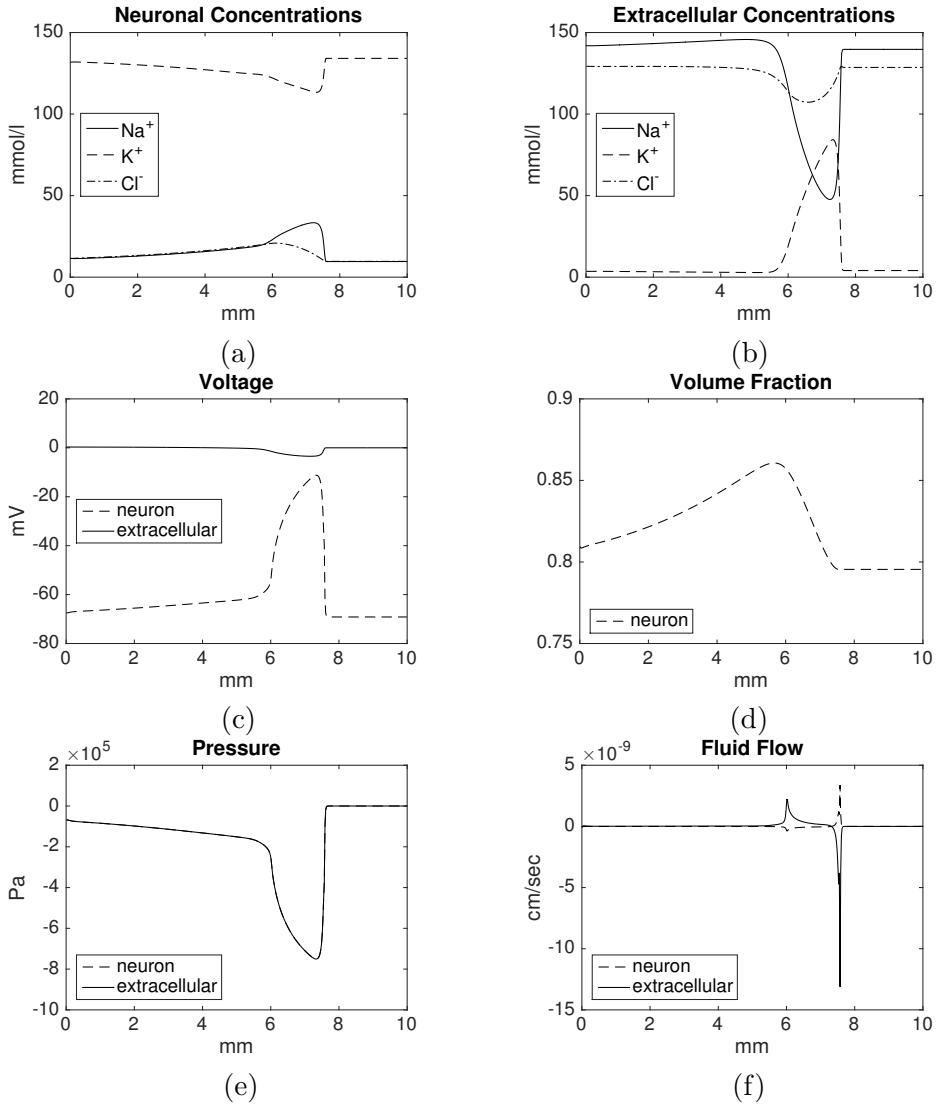

Figure 4.2: The model with $\kappa_{\mathrm{n}} = \kappa_{\mathrm{e}} = 5 \times 10^{-9}$ cm^4/dynes/sec after 240 seconds of simulated time. (a) Concentrations in the neuronal compartment are Na^+ (solid line), K^+ (dashed line), and Cl^- (dashed and dotted line). (b) Concentrations for the same ion species in the extracellular space. (c) The voltage for both compartments, with the solid line showing the neuronal and dashed the extracellular. (d) The volume fraction graph shows the neuronal volume fraction only. (e) The neuronal and extracellular pressures are approximately the same. (f) The two compartments have flow in the opposite directions. As with the voltage, the neuronal is the dashed line and the extracellular is solid.

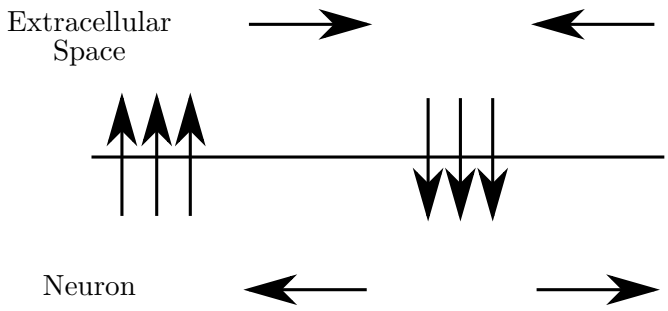

Figure 4.3: Schematic diagram of fluid flow during SD. Arrows indicate the direction of flow, with increasing volume fraction corresponding to flow into the compartment.

fluid is flowing across the membrane into the neuronal compartment. Fluid flow in the neuronal compartment is then away from this region, with positive (rightward) flow to the right of the swelling and negative (leftward) flow to the left of the swelling. In the extracellular compartment, flow is in the opposite direction, toward the area of cell swelling. Fig. 4.3 shows a schematic of the flow, with arrows indicating direction of flow.

With $\kappa_{\mathrm{n}} = \kappa_{\mathrm{e}} = 5 \times 10^{-7}$ cm^4/dynes/sec, fluid flow has a small effect on the propagation speed, increasing it to 4.0 mm/min. The only other significant effect of increasing the hydraulic permeability was an increase in the flow rate, which was uniformly greater than the flow rate with $\kappa_{\mathrm{n}} = \kappa_{\mathrm{e}} = 5 \times 10^{-9}$ by the expected factor of 100. The concentrations, voltages, volume fractions, pressures, and flow rates for the simulation with $\kappa_{\mathrm{n}} = \kappa_{\mathrm{e}} = 5 \times 10^{-7}$ cm^4/dynes/sec after two minutes are in Fig. 4.4.

We also ran simulations where one compartment had $\kappa_k = 5 \times 10^{-7}$ cm^4/dynes/sec and the other had 5×10^{-9} cm^4/dynes/sec. In these simulations, we found that the flow rate was limited by κ_{e}. Specifically, when $\kappa_{\mathrm{e}} = 5 \times 10^{-9}$ and $\kappa_{\mathrm{n}} = 5 \times 10^{-7}$, the system was essentially identical to $\kappa_{\mathrm{e}} = \kappa_{\mathrm{n}} = 5 \times 10^{-9}$. When $\kappa_{\mathrm{e}} = 5 \times 10^{-7}$ and $\kappa_{\mathrm{n}} = 5 \times 10^{-9}$, however, the system was essentially identical to $\kappa_{\mathrm{e}} = \kappa_{\mathrm{n}} = 5 \times 10^{-7}$. Given this, we theorize that there is a specific ratio of κ_{e} to κ_{n} for which increasing either one will have

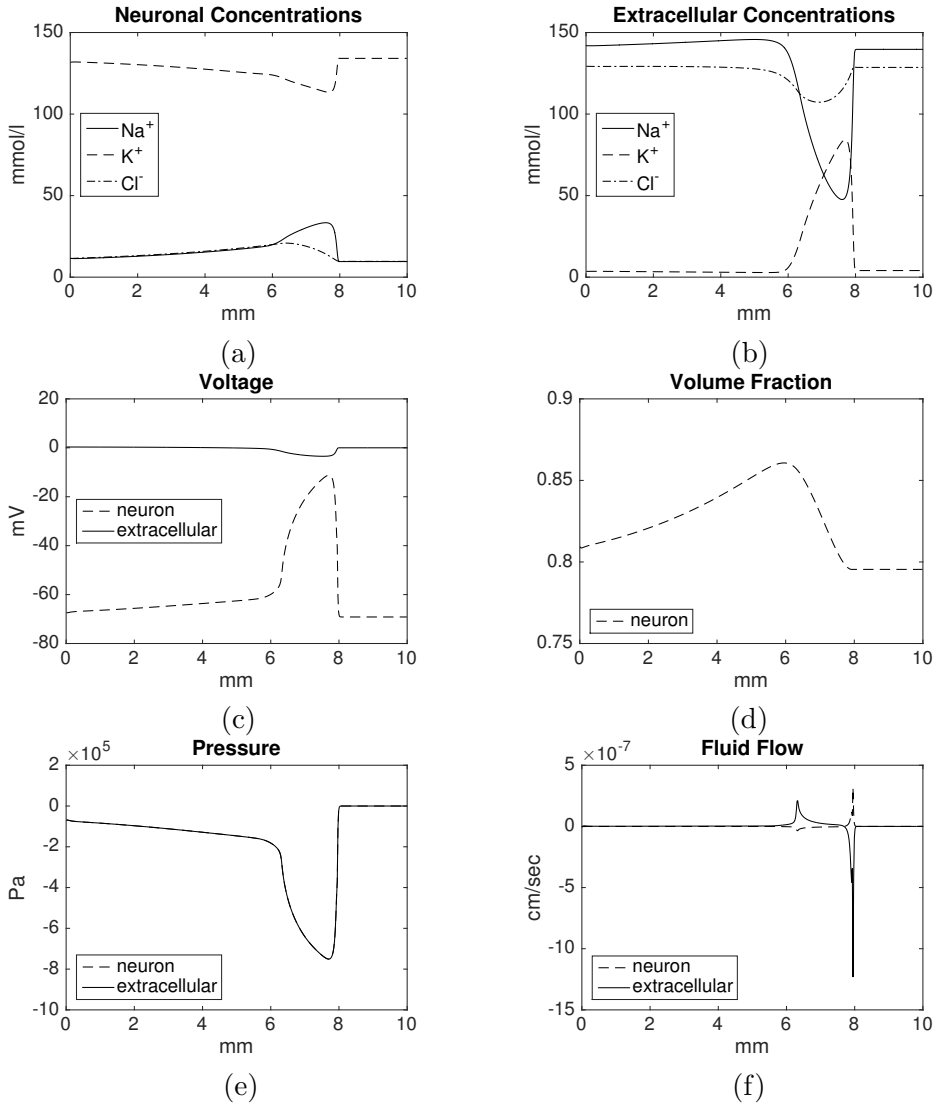

Figure 4.4: The model with $\kappa_{\mathrm{n}} = \kappa_{\mathrm{e}} = 5 \times 10^{-7}$ cm^4/dynes/sec after 240 seconds of simulated time. (a) Concentrations in the neuronal compartment are Na^+ (solid line), K^+ (dashed line), and Cl^- (dashed and dotted line). (b) Concentrations for the same ion species in the extracellular space. (c) The voltage for both compartments, with the solid line showing the neuronal and dashed the extracellular. (d) The volume fraction graph shows the neuronal volume fraction only. (e) The neuronal and extracellular pressures are approximately the same. (f) The two compartments have flow in the opposite directions. As with the voltage, the neuronal is the dashed line and the extracellular is solid.

no effect on the system, but increasing both will change the flow rate and, potentially, propagation speed. If so, this ratio must be greater than 100.

4.2 Membrane Stiffness

The introduction of a nonzero stiffness constant S_{n} should, again, have varying effect based on its value. If S_{n} is small enough, we expect only slight changes in the system, as the osmotic terms will dominate fluid flow. For larger S_{n}, we expect that the change in α_k will be of smaller magnitude, as some of the osmotic pressure differences that caused the change are balanced by increasing mechanical pressure as the cells swell. With that difference in the volume fractions, there will be accompanying changes in the concentrations of ions, which may in turn affect other aspects of SD.

The simulations show that there is indeed no change for small enough S_{n}. The difference between $S_{\mathrm{n}} = 0$ and $S_{\mathrm{n}} = 2.58 \times 10^4$ Pa/cm^3 is negligible, with the neuronal volume fraction increasing by 6.5% of the total volume in both cases and no change in the propagation speed. For $S_{\mathrm{n}} = 2.58 \times 10^6$ Pa/cm^3, however, the neuronal volume fraction only increases by 4.3% of the total volume. The change in volume fraction has the anticipated effect on the concentrations, but we find that the primary impact is on the recovery, since the initial changes in membrane potential and concentrations occur prior to the change in volume fraction. Fig. 4.5 shows the concentrations, voltages, volume fractions, pressures, and flow rates with $\kappa_{\mathrm{e}} = \kappa_{\mathrm{n}} = 5 \times 10^{-7}$ cm^4/dynes/sec and $S_{\mathrm{n}} = 2.58 \times 10^6$ Pa/cm^3. We note that the overshoot during recovery of the extracellular K^+ concentration is not as significant with $S_{\mathrm{n}} = 2.58 \times 10^6$ Pa/cm^3, as the concentration drops to a minimum of 3.00 mM instead of 2.83 mM. This corresponds to an overshoot of 1.02 mM, while the simulation with $S_{\mathrm{n}} = 0$ had an overshoot of 1.22 mM. In contrast, the magnitude of the positive tail to the DC shift was greater with $S_{\mathrm{n}} = 2.58 \times 10^6$ Pa/cm^3, reaching 0.60 mV, while it only reached 0.36 mV with $S_{\mathrm{n}} = 0$.

For $S_{\mathrm{n}} = 2.58 \times 10^8$ Pa/cm^3, however, there is only a minimal volume change for

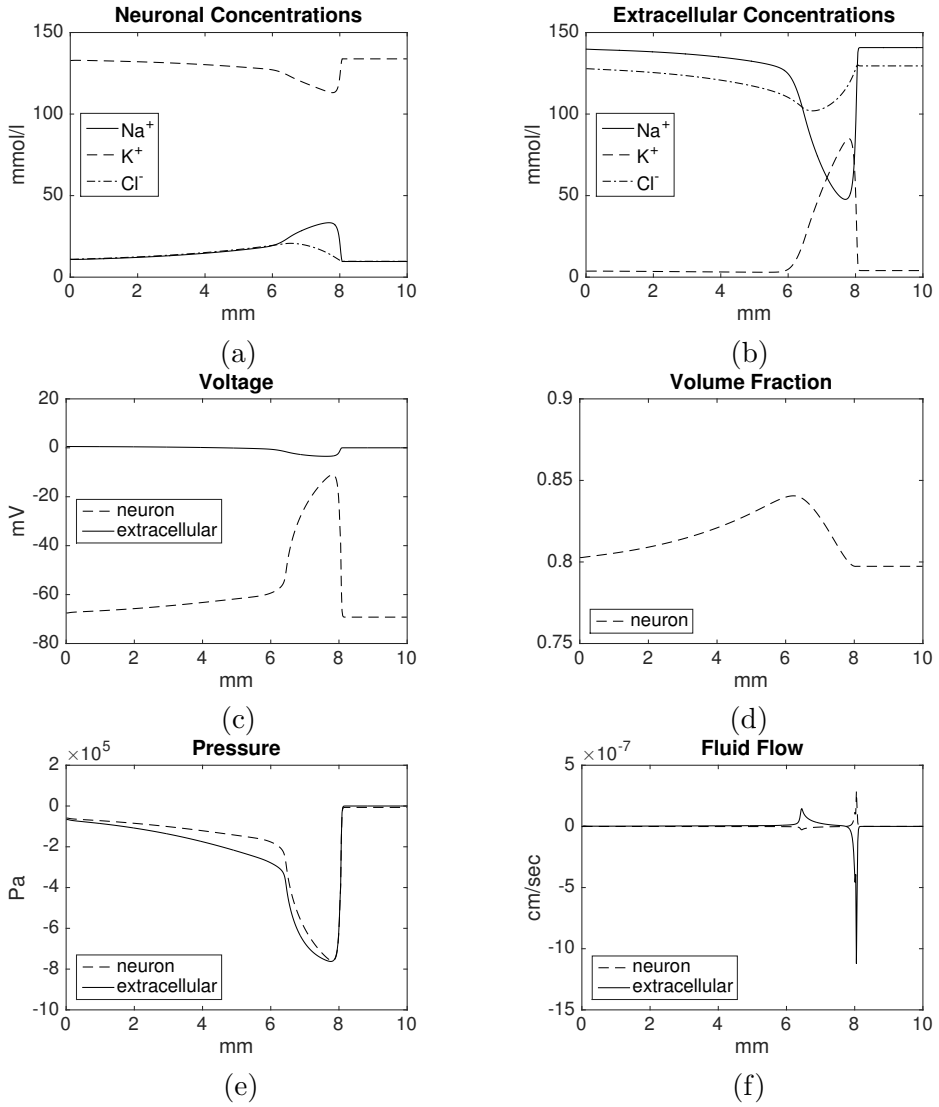

Figure 4.5: The model with intermediate stiffness, with hydraulic permeability $\kappa_{\mathrm{n}} = \kappa_{\mathrm{e}} = 5 \times 10^{-7}$ cm^4/dynes/sec and stiffness constant $S_{\mathrm{n}} = 2.58 \times 10^6$ Pa/cm^3 after 240 seconds of simulated time. (a) Concentrations in the neuronal compartment are Na^+ (solid line), K^+ (dashed line), and Cl^- (dashed and dotted line). (b) Concentrations for the same ion species in the extracellular space. (c) The voltage for both compartments. (d) The volume fraction graph shows the neuronal volume fraction only. (e) The neuronal and extracellular pressures are different. (f) The two compartments have flow in the opposite directions. For (c)–(f), the neuronal is the dashed line and the extracellular is solid.

the neuron, an increase of 0.1% of the total volume. Again, most of the changes as a result of increasing S_{n} appear in the recovery, but this change in S_{n} is also accompanied by a slight increase in propagation speed of approximately 0.1 mm/min. This change occurred across all values of κ_k for both compartments. Additionally, the DC shift was of a slightly larger magnitude, at 3.51 mV instead of 3.45 mV for $\kappa_k = 0$ and 3.49 mV instead of 3.46 mV for $\kappa_k = 5 \times 10^{-7}$ cm^4/dynes/sec, and the positive tail reached 1.02 mV. The effects of $S_{\mathrm{n}} = 2.58 \times 10^8$ Pa/cm^3 on the shape of the wave are shown in Fig. 4.6. We note that although we show only the results for $\kappa_{\mathrm{n}} = \kappa_{\mathrm{e}} = 5 \times 10^{-7}$ cm^4/dynes/sec, these effects were independent of κ_k.

Again, we find that increasing S_{n} decreases the degree of overshoot in the extracellular K^+ concentration, with a minimum of 3.31 mM and a net overshoot of 0.69 mM. The implication of these results is that the extracellular K^+ dropping below its resting value is partially, though not entirely, due to cell swelling. Since the overshoot of K^+ corresponds in time roughly to the recovery of the volume fraction, this makes intuitive sense. The recovery of the volume fraction corresponds to an increase in extracellular space, which in turn reduces the concentration of all ions in the extracellular space.

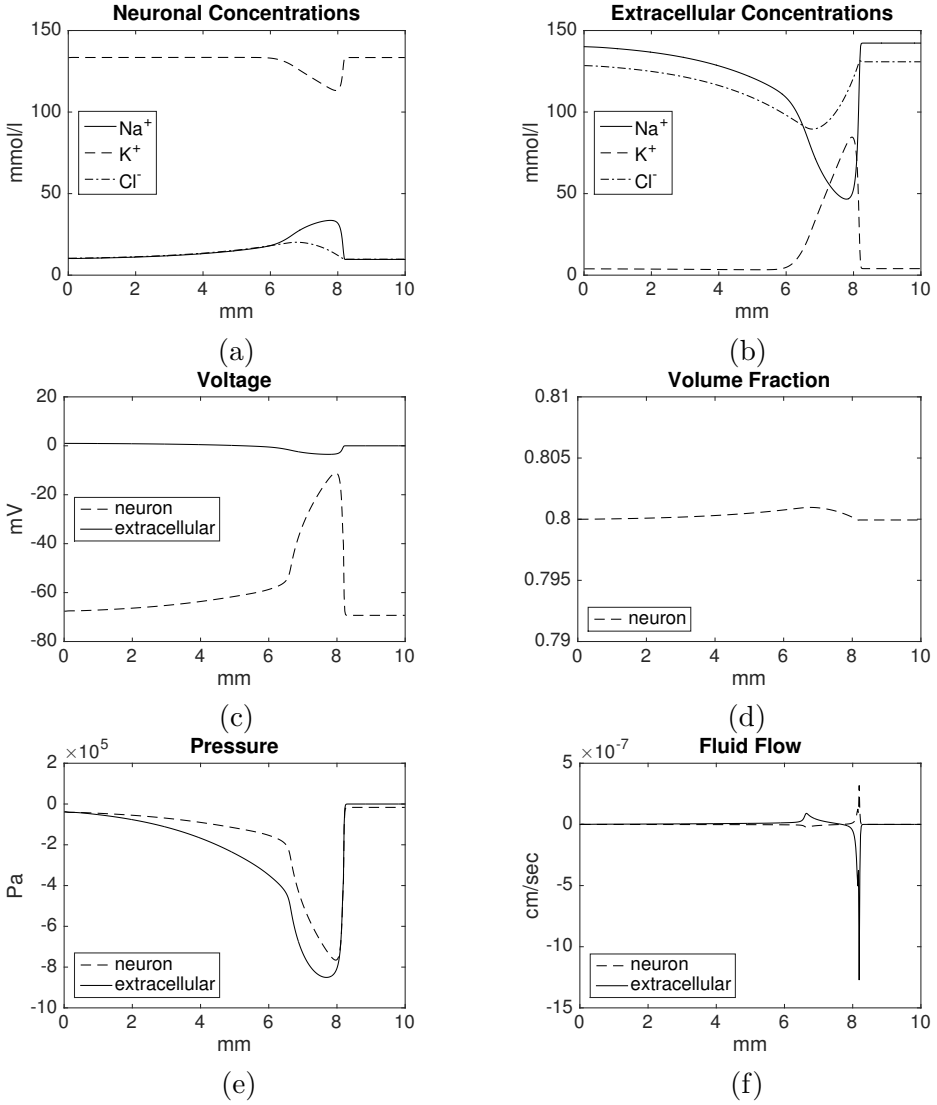

Figure 4.6: The model with high stiffness after 240 seconds of simulated time. The hydraulic permeability is $\kappa_{\mathrm{n}} = \kappa_{\mathrm{e}} = 5 \times 10^{-7}$ cm^4/dynes/sec and stiffness constant $S_{\mathrm{n}} = 2.58 \times 10^8$ Pa/cm^3. (a) Concentrations in the neuronal compartment are Na^+ (solid line), K^+ (dashed line), and Cl^- (dashed and dotted line). (b) Concentrations for the same ion species in the extracellular space. (c) The voltage for both compartments. (d) The volume fraction graph shows the neuronal volume fraction only. (e) The neuronal and extracellular pressures are different. (f) The two compartments have flow in the opposite directions. For (c)–(f), the neuronal is the dashed line and the extracellular is solid.

Chapter 5

Incorporating Glia

In the one-dimensional three-compartment model, our focus was the role of the glial syncytium as a K^+ buffer. Several parameters which affect K^+ in glial cells were systematically varied, allowing us to see the effects on the speed of propagation and relative timing of the changes which occur during SD. As in the two-compartment model, we used a domain that was 1 cm wide and triggered SD at the left edge (see section 3.7).

The speed of propagation was calculated by setting a threshold of 10 mV and recording when the change in the neuronal membrane potential reached the threshold at each point in our discretization. We looked at the points between 2.5 and 7.5 mm from the left edge to ensure edge effects resulting from the triggering of SD did not affect the calculation, and used linear regression on these data points to determine the propagation speed. For all of the simulations, the R^2 value was within 10^{-7} of 1.

In studying the relationship in the timing of different events, we looked at the times at which different variables reached a threshold at a specific point. The point in question was the closest discretization point to 5 mm ($X/2$, which is $5 - \triangle x/2$ as discussed in 3.8), and for simplicity will henceforth be referred to as simply 5 mm. The thresholds were a change of 2 mV from the resting values for the extracellular potential and the membrane potentials and of 1 mM in the extracellular potassium concentration.

5.1 General Results

The simulated wave shares many features with experimentally recorded traces, including a DC shift, membrane depolarization for both neurons and glia, ionic concentration changes, and cell swelling as shown in Fig. 5.1. Comparing these simulations to the simulations with only two compartments and no fluid flow discussed in Chapter 4 (see Fig. 4.1), we see that the neuronal features of SD are only minimally affected by the inclusion of glia. We note that the initial conditions of these simulations are not identical, making an exact comparison difficult, but the simulations share the same general shape and magnitude for the neuronal concentration changes. The extracellular concentrations also share the same general shape, though the role of glia as a buffer is apparent, as the magnitudes of the changes are reduced. For the volume fractions, a direct comparison is even more difficult, but we see a similar amount of overall swelling across the two intracellular compartments as occurs in the neuronal compartment of the two-compartment model, and the ratio of maximum volume fraction to resting volume fraction is similar across all three. The neuronal membrane potential, though not shown explicitly in either Fig. 4.1 or Fig. 5.1, is also very similar, but the extracellular potential shows a significant increase in magnitude with the inclusion of the glial compartment. The DC shift is discussed in detail in section 5.2.

The propagation speeds of all our simulations lie within the range of experimentally observed speeds, which are 1–15 mm/min [9], with specific values ranging from 2.5–8 mm/min and the majority of the simulations between 3 and 5 mm/min. All of our simulations showed a lingering positive tail to the DC shift after the primary negative shift, which was also observed in the simulations of Chapter 4 and is a feature present in many experiments [13, 28, 29, 31, 76, 77]. The magnitude of both the DC shift and the positive tail varied across the simulations, but in all cases the magnitude of the tail was much smaller than the negative shift, and the magnitude of the tail increased monotonically with the magnitude of the negative shift. As in the simulations in Chapter 4, we

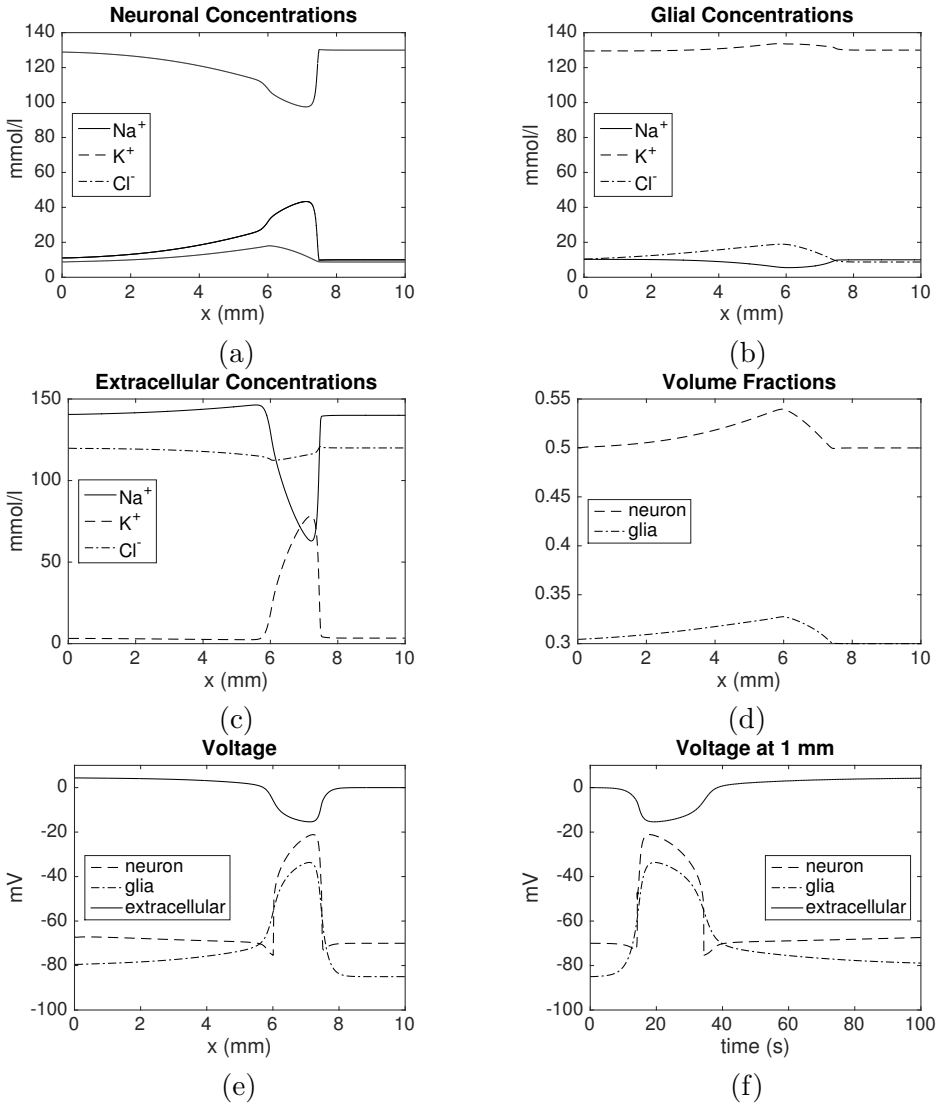

Figure 5.1: Sample simulation of SD with glial gap junction strength $d = 0.25$ and glial potassium permeability $G_{\mathrm{K}}^{\mathrm{g,IR}} = 13 \times 10^{-2}$ mS/cm^2, with a snapshot after about 103 seconds of simulated time shown in (a)–(e) and a trace in time at 1 mm in (f). Concentrations of Na^+ (solid), K^+ (dashed) and Cl^- (dashed and dotted) for the neurons are in (a), glia (b), and extracellular space (c). The volume fractions for neurons (dashed) and glia (dashed and dotted) are in (d), and voltages for neurons (dashed), glia (dashed and dotted), and the extracellular space (solid) are in (e) and (f).

observed an overshoot in the extracellular potassium concentrations in our simulations. Although the extent of the overshoot varied in the simulations involving fluid flow, it was approximately the same for all of the simulations with three compartments, falling past the resting value of 3.4 mM to a minimum of 2.9 mM before a gradual recovery to the resting value.

5.2 Glial Gap Junctions and K^+ Channel Density

To study how the glial syncytium affects SD through its capacity as a potassium buffer, we ran simulations with different degrees of glial gap-junctional coupling and densities of inward-rectifying K^+ channels on the glial membrane. To incorporate gap junctions in our model, we view the glial gap-junctional coupling strength as a modifier of the glial diffusion coefficient. The diffusion coefficients for all ions in the glial compartment were adjusted by a factor d, which we shall refer to as the gap junction strength:

$$D_i^{\mathrm{g}} = dD_i^* \alpha_{\mathrm{g}}^0 / \lambda^2,$$

where D_i^* is the diffusion coefficient in water, α_{g}^0 is the initial volume fraction of the glial compartment, and λ is the tortuosity. We adjust the density of inward-rectifying K^+ channels by changing the permeability of the channel, $G_{\mathrm{K}}^{\mathrm{g,IR}}$. Note that, as described in section 3.4, this change affects other parameters as well in order to maintain the same resting potential and concentrations for all simulations.

DC shift

The DC shift in the extracellular space was highly dependent on the gap junction strength but was minimally affected by the glial K^+ permeability. We observe an increase in the magnitude of the DC shift as gap-junctional coupling in the glial compartment increases. For small values of d, below about $d = 0.03$, the DC shift was between 3 and 5 mV, increasing with d. As d increased further, the magnitude of the DC shift

increases more dramatically, with values near 10 mV for $d = 0.125$, 16 mV for $d = 0.25$, and 25 mV for $d = 0.5$. Fig. 5.2 shows the magnitude of the DC shift for different values of d. The figure shows the values with $G_{\mathrm{K}}^{\mathrm{g,IR}} = 26 \times 10^{-2}$ mS/cm^2, but the values are relatively independent of $G_{\mathrm{K}}^{\mathrm{g,IR}}$.

This variation in the DC shift is a result of electrotonic effects in the interactions of the glial syncytium and the extracellular space. The electrical resistance in the glial syncytium is reduced when the gap junction strength is high, which leads to a smaller voltage deflection in the glia when the glia depolarize, with a corresponding larger voltage deflection through the extracellular space. When $d = 1$, the glial and extracellular diffusion coefficients are nearly the same, with differences only as a result of the difference in volume fractions. As a result, the electrical resistance is approximately the same in both compartments and the voltage deflection is split nearly equally across them. In our model, this is clearly evident, as the glial voltage increases by 33.4 mV while the extracellular voltage decreases by 34.8 mV. As d decreases from 1, the electrical resistance in the glia increases and the change in voltage is increasingly limited to the glial compartment, with smaller DC shifts. With either very low or no gap-junctional coupling, the DC shift is no longer significantly affected by the glial compartment, instead being primarily a result of the diffusion potential created by the concentration gradients in the extracellular space. Comparing with the DC shift in the simulations with no glial compartment discussed in Chapter 4, we find that the DC shift for simulations with $d < 0.03$ have similar magnitudes. These results provide computational support for glial involvement in sustained variation in extracellular potentials as discussed in [30]. They also are in agreement with the variation in the DC shift observed in mice with astrocyte-directed inactivation of gap junctions [45].

Speed

The effects of the glial gap-junctional coupling and the glial K^+ permeability on the propagation speed of SD are shown in Fig. 5.3. We find that the behavior as a function

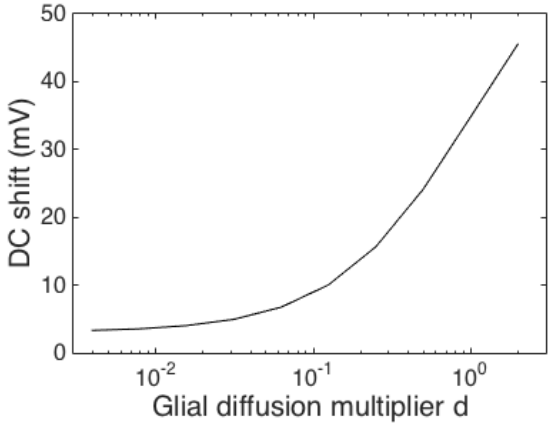

Figure 5.2: The magnitude of the DC shift was minimally affected by the glial potassium permeability, but significantly affected by the glial gap-junctional coupling. The DC shift was computed when the SD wave reached 7.5mm.

of the K^+ permeability is dependent on the gap-junctional coupling. If the gap junction strength is low, increasing the K^+ permeability decreases the propagation speed. For high values of the gap junction strength, an increase in the K^+ permeability increases the propagation speed. For intermediate values of the gap junction strength, the propagation speed shows biphasic behavior as a function of the K^+ permeability, reaching a maximum at an intermediate value of K^+ permeability. For any fixed K^+ permeability, however, increasing the gap junction strength results in increasing propagation speed, though the rate of increase is dramatically higher for larger K^+ permeabilities.

We performed the same simulations with a resting neuronal membrane potential of -75 mV and glial membrane potential of -90 mV and no tortuosity term ($\lambda = 1$) and found similar results for low or intermediate values of the two parameters. However, if both the gap junction strength and the K^+ permeability were high with these initial conditions, the SD event failed to propagate through the domain, corresponding to the cut off of the traces in Fig. 5.4. Values of d and $G_K^{g,IR}$ (given in mS/cm^2) for which propagation failed were $(d, G_K^{g,IR}) = (0.5, 2.19)$, $(1, 1.47)$, and $(2, 1.04)$, as well as all values for which one or both parameters were higher.

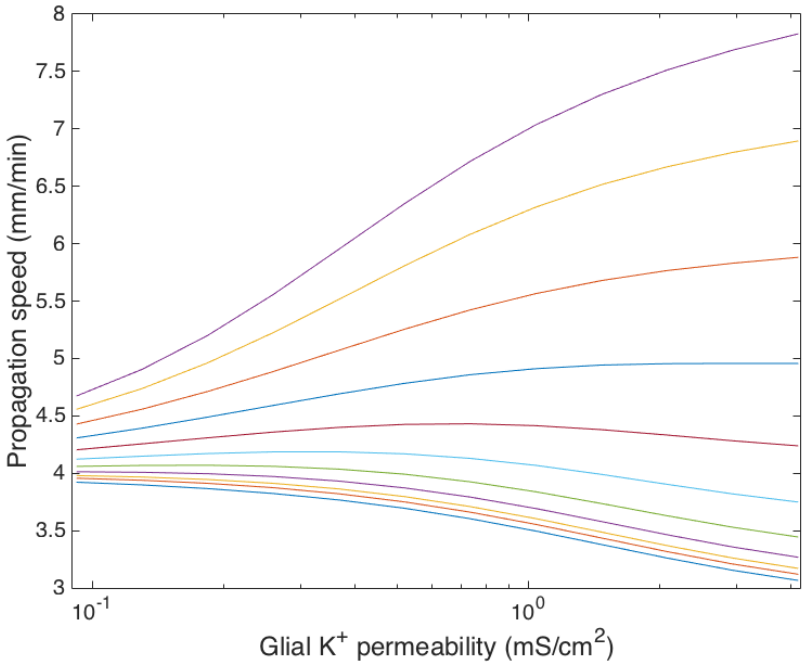

Figure 5.3: Effects of glial gap-junctional coupling and potassium permeability on the propagation speed of SD. The lowest curve shows $d = 0$ and the remaining curves show d equal to powers of 2 from 2^{-8} to 2, with increasing values of d corresponding to higher curves. Both parameters affected the propagation speed, with lowest speeds corresponding to low gap-junctional coupling and high potassium permeability and highest speeds corresponding to high gap-junctional coupling and high potassium permeability.

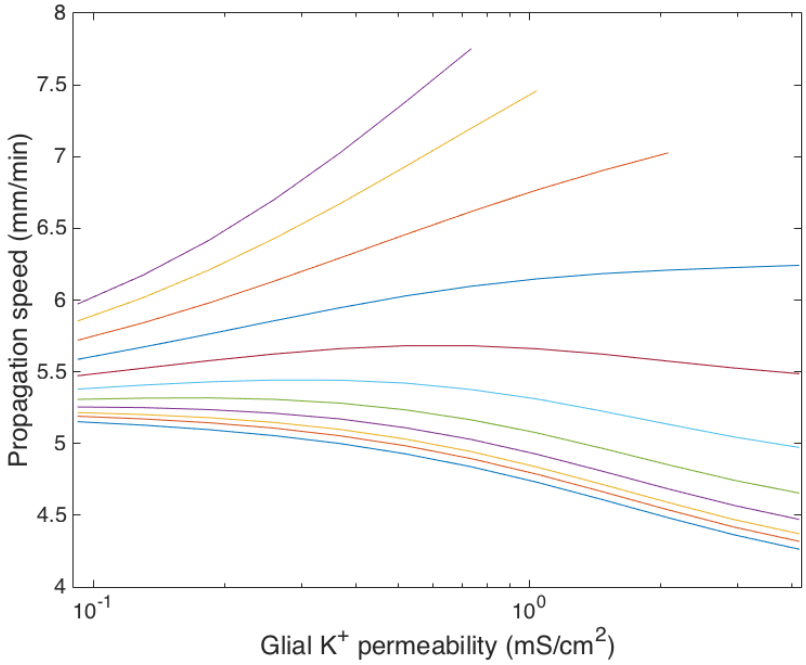

Figure 5.4: Effects of glial gap-junctional coupling and potassium permeability on the propagation speed of SD when the resting neuronal membrane potential is -75 mV and the tortuosity is $\lambda = 1$. The lowest curve shows $d = 0$ and the remaining curves show d equal to powers of 2 from 2^{-8} to 2, with increasing values of d corresponding to higher curves. Both parameters affected the propagation speed, with lowest speeds corresponding to low gap-junctional coupling and high potassium permeability and highest speeds corresponding to high gap-junctional coupling and high potassium permeability. The cut-off corner corresponds to a range of values where SD was triggered but did not propagate through the domain. Compare to Fig. 5.3 where the resting membrane potential is -70 mV and $\lambda = 1.6$.

These results indicate that glial cells play a subtle role in controlling the extracellular K^+ concentration. The glia may either buffer or broadcast K^+ in the extracellular space, depending on the values of the gap junction strength and K^+ permeability. When the gap junction strength is low but the glia have high K^+ permeability, they act as a K^+ buffer, with K^+ passing into the glial cells and remaining there until the extracellular K^+ decreases again. As a result, there is a relatively low propagation speed. In contrast, if the gap junction strength is high but the K^+ permeability is low, the glia broadcast K^+, as K^+ entering the glial cells leads to a release of K^+ into the extracellular space away from the SD event, which in turn leads to a faster increase in the K^+ away from the initial point and a faster speed of propagation. We believe this is the first computational support of K^+ broadcasting, which has been considered a likely feature of the K^+ buffering system [1]. A further increase in glial gap-junctional coupling, however, leads to propagation failure when the resting neuronal membrane potential is -75 mV and the tortuosity is $\lambda = 1$. We suggest that this is due to the glial cells providing sufficient potassium buffering with these scenarios. The glial syncytium is able to keep the extracellular K^+ concentration low enough that SD is not triggered nearby. We believe that such a feature may appear with higher values when the resting membrane potential is -70 mV and tortuosity is included. The halt of propagation at high values of gap-junctional coupling is in agreement with experimental evidence that SD is induced more easily in mice whose glial gap junctions are inactivated [45].

The results involving gap-junctional coupling are similar to the effect of intercellular or intracellular resistance on action potential propagation and initiation in cardiac and neuronal physiology. Reducing the intracellular (for action potentials) or intercellular, (for cardiac tissue) resistance leads not only to an increase in propagation speed but also to a higher threshold current for excitation, thus increasing the possibility for propagation failure [69]. The role of glial gap-junctional coupling in SD is more subtle, however, since the glia are not directly involved in the neuronal depolarization that is fundamental to SD.

Timing of the DC shift

In order to gain a better understanding of the mechanisms of SD propagation, the relative timing of the DC shift and the extracellular K^+ increase that accompany SD has been studied frequently [78]. We use our simulation results to compare the timing of the DC shift, the neuronal and glial depolarizations, and the extracellular K^+ increase.

We found that the neuronal depolarization and the increase in extracellular K^+ were the most closely correlated, with the two occurring at nearly the same time for the majority of simulations, as shown in Fig. 5.5a. The two were separated by less than one-tenth of a second except for when the gap junction strength was high and the K^+ permeability low, in which case the extracellular K^+ came after the neuronal depolarization by less than 2 seconds. This suggests that the depolarization and extracellular K^+ increase are very closely linked, with a feedback loop of depolarization and increasing K^+ levels.

In contrast, the DC shift was not as correlated with the neuronal depolarization. When the gap junction strength was low, with $d \leq 0.0625$, the DC shift was largely independent of the glial K^+ permeability and occurred up to 1.5 seconds after the neuronal depolarization and the extracellular K^+ increase. We note that these values were when the extracellular K^+ increase was closest to the neuronal depolarization. When d was between 0.125 and 0.25, the DC shift occurred before the neuronal depolarization for low glial K^+ permeability and after for high permeability, as shown in Fig. 5.5b. If d was greater than 0.25, the DC shift occurred before the neuronal depolarization for all amounts of glial K^+ permeability by up to 9 seconds, with greater differences for lower permeabilities.

The timing of the glial depolarization relative to the neuronal depolarization was also highly dependent on the parameters (Fig. 5.5c). Unlike the DC shift and the extracellular K^+ increase, the glial depolarization always began before the neuronal depolarization, and in fact was always before both the DC shift and the extracellular K^+

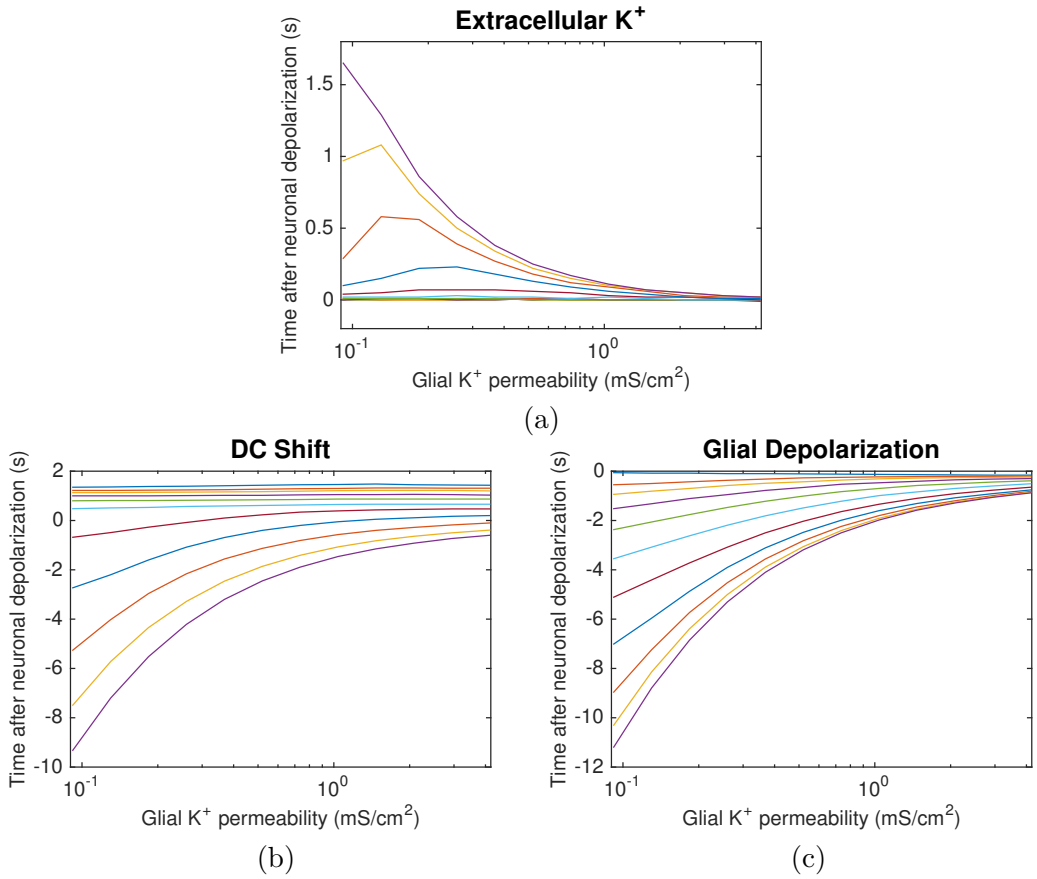

Figure 5.5: Effects of glial gap-junctional coupling and potassium permeability on the relative timing of the DC shift, extracellular potassium increase, and neuronal and glial depolarizations. The timing of a 1 mM change in the $[K^+]_e$ (a), a 2 mV change in the extracellular potential (DC shift) (b), and a 2 mV change in the glial membrane potential (c) are shown relative to a 2 mV change in the neuronal membrane potential. For (a), the highest line shows $d = 2$, with each lower line showing d equal to half the line above, and values between 2^{-4} and 0 nearly indistinguishable. In (b) and (c) the order is reversed, with the lowest line representing $d = 2$ and the highest line $d = 0$.

increase as well. If the gap junction strength was very low or the glial K^+ permeability very high, the glial depolarization began less than a second before the neuronal depolarization. However, for low permeability and high gap-junctional coupling, the glial depolarization began up to 11 seconds before the neuronal depolarization. This early depolarization is related to the electrotonic effects that contribute to the magnitude of the DC shift, as increased gap-junctional coupling allows the glial depolarization to spread ahead of the SD wavefront. The relationship between the DC shift and the neuronal depolarization, which shows similar behavior, is likely also a result of these electrotonic effects. We note that for the majority of the simulations, the glial depolarization is only a second or two earlier than the DC shift, with the most significant differences occurring for low glial K^+ permeability and intermediate gap-junctional coupling. Both the connection between the timing of the DC shift and the glial depolarization and the variation in the relative timing of the neuronal depolarization relative to the DC shift have been seen experimentally [29].

5.3 Na^+/K^+ ATPase

In addition to exploring the effects of the glial K^+ permeability, we looked at different strengths of the Na^+/K^+ ATPase. Unlike the glial gap-junctional coupling and the potassium inward rectifier, which are both energetically passive, the Na^+/K^+ ATPase is an active transporter that uses chemical energy. We let the Na^+/K^+ ATPase strength vary from 0.5 to 1.5 times the value given in Table 3.5, with three different gap junction strengths, $d = 0.0625$, 0.125, and 0.25. We performed two sets of simulations, one in which the Na^+/K^+ ATPase strength was varied for both membranes, and one in which it was varied for only the glial membrane. Varying the strength on both membranes can be viewed as a reduction in the available energy (depletion of ATP) or other inhibitors of the Na^+/K^+ ATPase, while varying only the strength on the glial membrane reflects mutations specific to glial Na^+/K^+ ATPase. In either case, changing the Na^+/K^+

ATPase changes the resting membrane potentials and concentrations and we allowed the system to come to the rest state before triggering SD, with the new rest states given in Table 3.7. When the Na^+/K^+ ATPase strength was less than 0.8 times the original value for both membranes, or less than 0.7 for just the glial membrane, no rest state was achieved, as the system experienced recurring spontaneous SD events. This mimics the effects of ouabain, which is an inhibitor of Na^+/K^+ ATPase sometimes used as a trigger for SD in experimental studies [2, 39, 79]. For these values, no propagation speed can be determined, since SD occurs at all points simultaneously.

We also ran simulations with initial resting membrane potentials of -75 mV for the neuron and -90 mV for the glia. The results were similar, but for these rest states, SD occurred spontaneously only when the Na^+/K^+ ATPase was adjusted on both membranes and the multiplier was less than 0.7. In addition, when the Na^+/K^+ ATPase strength was multiplied by 1.5 on both membranes, the excitation protocol was insufficient to trigger SD.

The propagation speed of SD increased with decreasing pump strength for both rest states and all gap junction strengths, whether or not the change was made to both membranes or just the glial membrane, as shown in Fig. 5.6. Speeds were faster when the initial potentials were higher, consistent with the increased likelihood that SD would occur spontaneously with reduced Na^+/K^+ ATPase strength. The simulations with Na^+/K^+ ATPase changed only on the glial membrane are consistent with a subtype of familial hemiplegic migraine in which mutations occur in the gene encoding the $\alpha 2$ subunit of the Na^+/K^+ ATPase [32, 33], which is expressed on glia [80].

The relative timing of the membrane depolarizations, DC shift, and extracellular K^+ increase, all measured as changes from the rest state values, was minimally affected by the Na^+/K^+ ATPase strength. The order of all events was dictated by the gap junction strength as described in section 5.2, with a slight increase in the amount of time between events as the Na^+/K^+ ATPase strength increased.

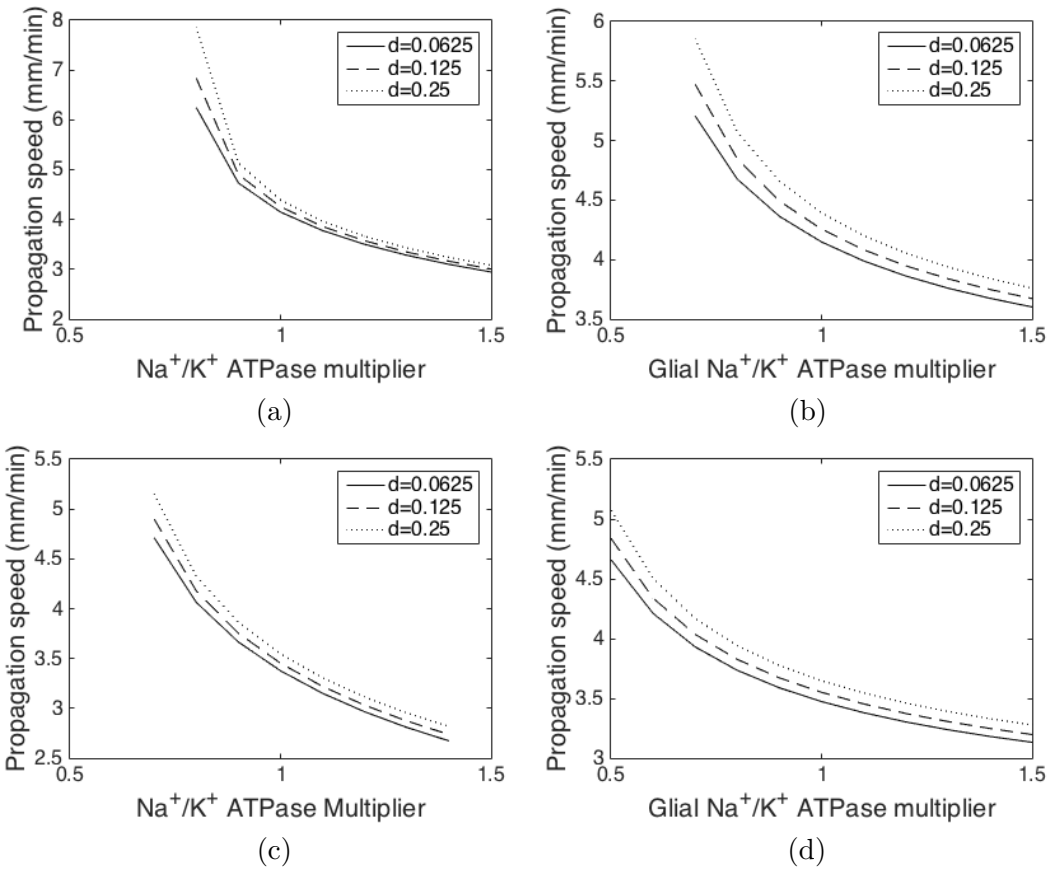

Figure 5.6: Effects of Na^+/K^+ ATPase on the propagation speed of SD, affecting both membranes ((a), (c)), and only the glial membrane ((b), (d)). The conditions prior to changing the strength of the Na^+/K^+ ATPase for (a) and (b) were -70 mV and -85 mV for the neuronal and glial membrane potentials, respectively, while those conditions for (c) and (d) were -75 mV and -90 mV. Increasing the pump strength decreased the propagation speed in both cases. Solid lines indicate $d = 0.0625$, dashed lines $d = 0.125$, and dotted lines $d = 0.25$. Missing values at the left of (a)–(c) correspond to values of the Na^+/K^+ ATPase multiplier for which SD occurred spontaneously at all points, and missing values at the right of (c) correspond to failure of the excitation protocol to trigger SD.

Chapter 6

NMDA Receptors and Cell Overlap

Since NMDA receptor antagonists have been shown to block the propagation of SD, we introduced NMDA receptors to our model. The equations governing the NMDA receptor are explained in detail in section 6.1. In addition, we modified the model to explore the potential effects of cells being close neighbors.

We begin by adapting the model to incorporate the spatial extent of neurons. We let cells have a size of 40 μm, while our discretization was $\triangle x = 20$ μm. To represent an individual cell, two neighboring points in the neuronal compartment were connected through diffusion. Thus the diffusion coefficient in the neuronal compartment was of the form

$$D^{\mathrm{n}}_{i,l+1/2} = \begin{cases} D^*_i \frac{\alpha_{\mathrm{n},l}+\alpha_{\mathrm{n},l+1}}{2} & \text{if } l \text{ is odd} \\ 0 & \text{if } l \text{ is even,} \end{cases} \tag{6.1}$$

where $D_{i,l+1/2}$ denotes the diffusion coefficient between discretization points l and $l+1$ as described in section 3.8.

To explore the effects of overlapping cells, we developed two variations of the model, both using two neuronal compartments for a total of four compartments. The first

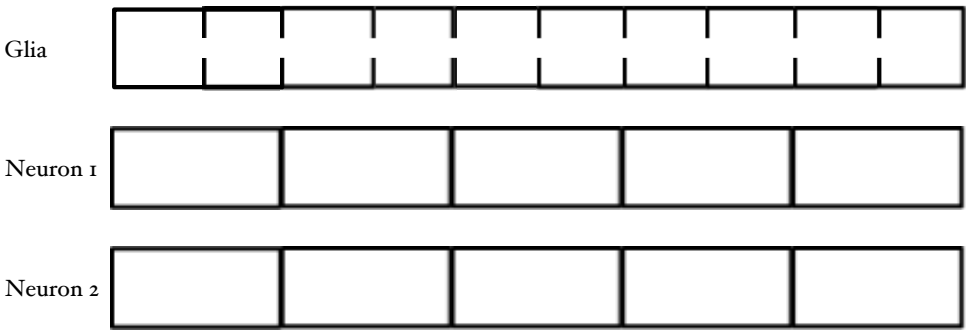

Figure 6.1: Schematic diagram of the stacked model involving two neuronal compartments and a glial compartment. Diffusion is allowed within cells in the neuronal compartments but not across the membranes, while glia have reduced diffusion through gap junctions.

variation, which we call the stacked model, was developed by splitting the neuronal compartment into two identical compartments, each with a resting volume fraction that was half that of the neuronal compartment in the three compartment model. The parameter γ, which represents the cell surface area per unit volume, was halved for each of the two neuronal compartments. In combination with the dependence of the diffusion coefficient on the volume fraction, this adjustment to γ results in the stacked four compartment model being equivalent to the three compartment model. Due to the equivalence between the stacked model and the three compartment model, most of our simulations for the stacked model were done using the three compartment model to reduce computational time. Some simulations involving the stacked model were done to confirm that the implementation in four compartments was equivalent. A schematic diagram of the stacked model is shown in Fig. 6.1.

The second variation, called the staggered model, is identical to the stacked model in all ways except for the diffusion coefficient. In the stacked model, the two neuronal compartments both satisfy Eq. (6.1), so that the cells are stacked directly on top of each other. In the staggered model, one neuronal compartment ($n = n_1$) satisfies Eq. (6.1),

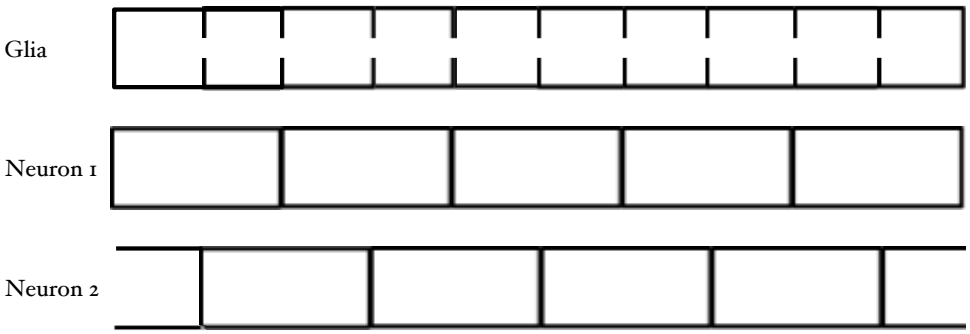

Figure 6.2: Schematic diagram of the staggered model involving two neuronal compartments and a glial compartment. Diffusion is allowed within cells in the neuronal compartments but not across the membranes, while glia have reduced diffusion through gap junctions.

while the other satisfies

$$D^{\mathrm{n}_2}_{i,l+1/2} = \begin{cases} 0 & \text{if } l \text{ is odd} \\ D^*_i \frac{\alpha_{\mathrm{n},l}+\alpha_{\mathrm{n},l+1}}{2} & \text{if } l \text{ is even.} \end{cases} \tag{6.2}$$

The effect of the staggered model is that each cell overlaps halfway with two cells in the other compartment. A schematic diagram of the staggered model appears in Fig. 6.2.

Since the only difference between the two neuronal compartments is the diffusion coefficient, we will continue to use $k = \mathrm{n}$ to refer to all other neuronal parameters. For the stacked model, all values are identical between the two neuronal compartments, and we may use $k = \mathrm{n}$ or $k = \mathrm{n}_1$ and $k = \mathrm{n}_2$ interchangeably to refer to them. For the variables that may be different between the two compartments in the staggered model, we will refer to them as $k = \mathrm{n}_1$ and $k = \mathrm{n}_2$.

We will, at times, look at only the left part or right part of the cells. For the stacked model, this requires looking at every other discretization point, whereas for the staggered model, the values we consider will alternate between $k = \mathrm{n}_1$ and $k = \mathrm{n}_2$.

6.1 NMDA Receptor Equations

Recall that the flow of ions across a specific channel of type μ is given by

$$j_i^{k,\mu} = \hat{g}_i^{k,\mu} J_i^{k,\mu}, \tag{6.3}$$

where $\hat{g}_i^{k,\mu}$ is the proportion of open channels, which is a function of the gating variables, and $J_i^{k,\mu}$ is a function of the current-voltage relationship. The equations governing glutamate and the NMDA receptor were adapted from the model given in [63]:

$$\hat{g}^{\mathrm{n,NMDA}} = y(t)G(\phi_{\mathrm{ne}}) \tag{6.4}$$

$$J_{\mathrm{Na}}^{\mathrm{n,NMDA}} = P^{\mathrm{n,NMDA}} \frac{F\phi_{\mathrm{ne}}}{RT} \frac{c_{\mathrm{Na}}^{\mathrm{n}} \exp(\frac{F\phi_{\mathrm{ne}}}{RT}) - c_{\mathrm{Na}}^{\mathrm{e}}}{\exp(\frac{F\phi_{\mathrm{ne}}}{RT}) - 1} \tag{6.5}$$

$$J_{\mathrm{K}}^{\mathrm{n,NMDA}} = P^{\mathrm{n,NMDA}} \frac{F\phi_{\mathrm{ne}}}{RT} \frac{c_{\mathrm{K}}^{\mathrm{n}} \exp(\frac{F\phi_{\mathrm{ne}}}{RT}) - c_{\mathrm{K}}^{\mathrm{e}}}{\exp(\frac{F\phi_{\mathrm{ne}}}{RT}) - 1} \tag{6.6}$$

$$\frac{dy}{dt} = 72[\mathrm{Glu}]_{\mathrm{e}}(1-y) - 6.6y \tag{6.7}$$

$$G(\phi) = \frac{1}{1 + 0.28e^{-0.062\phi}} \tag{6.8}$$

$$\frac{d[\mathrm{Glu}]_{\mathrm{e}}}{dt} = Ae^{-0.0044(\phi_{\mathrm{ne}}-8.66)^2} - B[\mathrm{Glu}]_{\mathrm{e}} \tag{6.9}$$

In these equations, $y(t)$ is the probability of channels being open as a function of the glutamate concentration, and $G(\phi)$ is the voltage gating. The extracellular glutamate concentration is governed by the membrane potential as well as a release rate A and a decay rate B, with $A = 600$ mM/s and $B = 10$ s^{-1} in [63]. With these equations, the interactions between the glutamate concentration and the membrane potential results in a feedback loop that yields an extracellular concentration of glutamate which is not physiologically reasonable. In order to limit the concentration of glutamate, we introduced an intracellular glutamate concentration in all neuronal compartments and adjusted the glutamate release rate to reflect the effect of glutamate depletion in each cell. Eq. (6.9) was modified to

$$\frac{d[\mathrm{Glu}]_{\mathrm{e}}}{dt} = A\frac{[\mathrm{Glu}]_{\mathrm{n}}}{\epsilon + [\mathrm{Glu}]_{\mathrm{n}}} e^{-0.0044(\phi_{\mathrm{ne}}-8.66)^2} - B[\mathrm{Glu}]_{\mathrm{e}}, \tag{6.10}$$

where ϵ is small. In turn, the intracellular glutamate concentration satisfies

$$\frac{d[\mathrm{Glu}]_{\mathrm{n}}}{dt} = -A\frac{[\mathrm{Glu}]_{\mathrm{n}}}{\epsilon + [\mathrm{Glu}]_{\mathrm{n}}}e^{-0.0044(\phi_{\mathrm{ne}}-8.66)^2} + \nu B[\mathrm{Glu}]_{\mathrm{e}}, \tag{6.11}$$

where $0 \leq \nu \leq 1$ represents a reabsorption rate, with the remainder of the extracellular glutamate "decay" assumed to enter the glial cells, where it remains for the duration of the simulation. Unless otherwise specified, our simulations have $\nu = 0.2$.

In addition, we modified the equation governing $y(t)$, the open probability based on extracellular glutamate, so that the probability of a channel opening was no longer a linear function of the glutamate concentration, and instead had a maximum possible rate. Specifically, we set

$$\frac{dy}{dt} = 72\frac{[\mathrm{Glu}]_{\mathrm{e}}}{[\mathrm{Glu}]_{\mathrm{e}} + 0.05}(1-y) - 6.6y. \tag{6.12}$$

The equations governing the glutamate dynamics must be further adapted to maintain conservation of glutamate while accounting for changes in volume fraction. We shift our perspective from a differential equation governing the concentration to one governing the total amount of glutamate in each compartment, yielding

$$\frac{d(\alpha_{\mathrm{e}}[\mathrm{Glu}]_{\mathrm{e}})}{dt} = A\alpha_{\mathrm{n}}\frac{[\mathrm{Glu}]_{\mathrm{n}}}{\epsilon + [\mathrm{Glu}]_{\mathrm{n}}}e^{-0.0044(\phi_{\mathrm{ne}}-8.66)^2} - B\alpha_{\mathrm{e}}[\mathrm{Glu}]_{\mathrm{e}} \tag{6.13}$$

$$\frac{d(\alpha_{\mathrm{n}}[\mathrm{Glu}]_{\mathrm{n}})}{dt} = -A\alpha_{\mathrm{n}}\frac{[\mathrm{Glu}]_{\mathrm{n}}}{\epsilon + [\mathrm{Glu}]_{\mathrm{n}}}e^{-0.0044(\phi_{\mathrm{ne}}-8.66)^2} + \nu B\alpha_{\mathrm{e}}[\mathrm{Glu}]_{\mathrm{e}} \tag{6.14}$$

$$\frac{d(\alpha_{\mathrm{g}}[\mathrm{Glu}]_{\mathrm{g}})}{dt} = (1-\nu)B\alpha_{\mathrm{e}}[\mathrm{Glu}]_{\mathrm{e}}. \tag{6.15}$$

For the four compartment model, the equations are as follows:

$$\frac{d(\alpha_{\mathrm{e}}[\mathrm{Glu}]_{\mathrm{e}})}{dt} = \sum_{k=\mathrm{n}_1,\mathrm{n}_2}\left(A\alpha_k\frac{[\mathrm{Glu}]_k}{\epsilon + [\mathrm{Glu}]_k}e^{-0.0044(\phi_{k\mathrm{e}}-8.66)^2}\right) - B\alpha_{\mathrm{e}}[\mathrm{Glu}]_{\mathrm{e}} \tag{6.16}$$

$$\frac{d(\alpha_{\mathrm{n}_1}[\mathrm{Glu}]_{\mathrm{n}_1})}{dt} = -A\alpha_{\mathrm{n}_1}\frac{[\mathrm{Glu}]_{\mathrm{n}_1}}{\epsilon + [\mathrm{Glu}]_{\mathrm{n}_1}}e^{-0.0044(\phi_{\mathrm{n}_1\mathrm{e}}-8.66)^2} + \frac{\nu}{2}B\alpha_{\mathrm{e}}[\mathrm{Glu}]_{\mathrm{e}} \tag{6.17}$$

$$\frac{d(\alpha_{\mathrm{n}_2}[\mathrm{Glu}]_{\mathrm{n}_2})}{dt} = -A\alpha_{\mathrm{n}_2}\frac{[\mathrm{Glu}]_{\mathrm{n}_2}}{\epsilon + [\mathrm{Glu}]_{\mathrm{n}_2}}e^{-0.0044(\phi_{\mathrm{n}_2\mathrm{e}}-8.66)^2} + \frac{\nu}{2}B\alpha_{\mathrm{e}}[\mathrm{Glu}]_{\mathrm{e}} \tag{6.18}$$

$$\frac{d(\alpha_{\mathrm{g}}[\mathrm{Glu}]_{\mathrm{g}})}{dt} = (1-\nu)B\alpha_{\mathrm{e}}[\mathrm{Glu}]_{\mathrm{e}}. \tag{6.19}$$

6.2 Similar Role for Persistent Na^+ Channel and NMDA Receptors

The persistent Na^+ channel and NMDA receptor are both opened by depolarization. To compare the roles of the two channels, we ran simulations with a range of values for both $P_{\mathrm{Na}}^{\mathrm{n,P}}$ and $P^{\mathrm{n,NMDA}}$. To implement this, we multiplied the parameter values given in Table 3.9 by different values. The final parameter values ranged from $P_{\mathrm{Na}}^{\mathrm{n,P}} = 0$ to $P_{\mathrm{Na}}^{\mathrm{n,P}} = 2 \times 10^{-5}$ cm/s for the persistent sodium channel, and from $P^{\mathrm{n,NMDA}} = 0$ to $P^{\mathrm{n,NMDA}} = 5 \times 10^{-5}$ cm/s. We turn our attention first to the stacked model. The results of our simulations show that the two channels play a similar role in SD. If the permeability of either channel is sufficiently high, SD occurs even if the other channel's permeability is zero. The boundary of SD initiation, as a function of the two permeabilities, is roughly linear between these two points, as shown in Fig. 6.3.

Furthermore, increasing the permeability of either channel results in an increase in the propagation speed. The propagation speed is determined in a similar manner as in the simulations described in Chapter 5, but adapted due to the spatial extent of cells. To compute the propagation speed in the four-compartment models, we look at only the timing of the wave reaching the first point in each cell. Thus, for the stacked model, we compute the propagation speed by determining when the neuronal membrane potential at odd discretization points between 2.5 mm and 7.5 mm reaches the threshold of a 10 mV difference from the resting voltage. From there, we use linear regression to determine the speed. For the staggered model, the approach is the same except that we look at the membrane potential in n_1 at odd discretization points and n_2 at even discretization points. We find that the value of $P_{\mathrm{Na}}^{\mathrm{n,P}}$ has a slightly greater effect on the propagation speed, but increasing either increases the speed. Specifically, we see an increase from 2.7 to 4.9 mm/min as $P_{\mathrm{Na}}^{\mathrm{n,P}}$ goes from 1.2×10^{-5} to 2×10^{-5} cm/sec with no NMDA recepter permeability, and an increase from 1.9 to 2.5 mm/min as $P^{\mathrm{n,NMDA}}$ goes from 3×10^{-5} to 5×10^{-5} cm/sec with no persistent Na^+ permeability. Similar

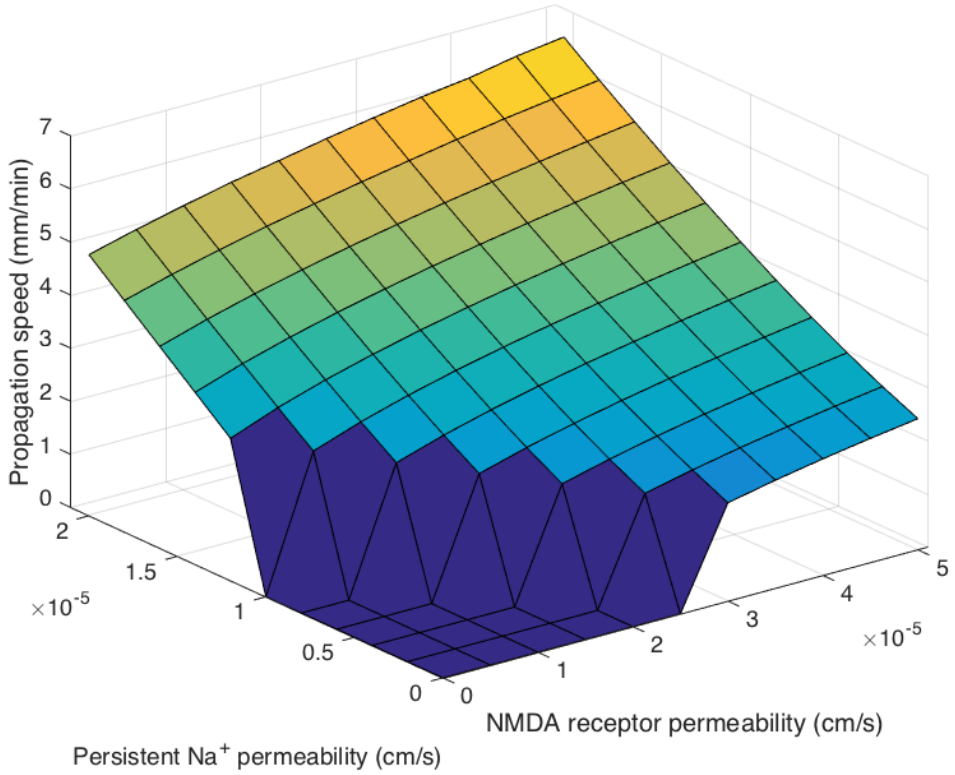

Figure 6.3: Propagation speeds of SD in the stacked model with different permeabilities for the persistent Na^+ channel and the NMDA receptor. Propagation speeds of 0 indicate that SD did not occur.

behavior is seen for each permeability while holding the other permeability constant at any value. Fig. 6.3 shows the propagation speeds of the stacked model for the whole range of values in our simulations.

We suggest that increasing the permeabilities of either channel makes it easier for SD to be triggered at any point. In turn, propagation is faster, as the threshold for triggering SD is reached sooner relative to its arrival at the neighboring point.

6.3 Effect of Cell Overlap on Propagation

The propagation speeds of the stacked and staggered models were significantly different, particularly for the simulations with higher values of $P^{\mathrm{n,NMDA}}$. Propagation speeds for the staggered model are shown in Fig. 6.4 for the whole range of values in our simulations. For the simulations with $P^{\mathrm{n,NMDA}} = 0$, the propagation speeds increased by a factor of approximately 1.1 for the staggered model for all values of $P_{\mathrm{Na}}^{\mathrm{n,P}}$ for which propagation occurred, with speeds of 2.9 mm/min when $P_{\mathrm{Na}}^{\mathrm{n,P}} = 1.2\times10^{-5}$ cm/sec to 5.3 mm/min when $P_{\mathrm{Na}}^{\mathrm{n,P}} = 2\times10^{-5}$ cm/sec. For the simulations with $P_{\mathrm{Na}}^{\mathrm{n,P}} = 0$, however, the speeds were 1.7–1.9 times as fast, with speeds of 3.1 mm/min when $P^{\mathrm{n,NMDA}} = 3\times10^{-5}$ cm/sec to 4.7 mm/min when $P^{\mathrm{n,NMDA}} = 5 \times 10^{-5}$ cm/sec. The difference in speeds between the stacked and staggered models is shown in Fig. 6.5.

We observe that there is a slight variation in the behavior between the left and right parts of the cells. As expected, the depolarization of the left part of the cell precedes that of the right part. Fig. 6.6 shows the change in the membrane potential of both the left and right part of the cell whose left edge is at 2.5 mm as the SD wave arrives, as well as the extracellular voltage at 2.5 mm, for simulations using the stacked model with just persistent Na^+ permeability and with just NMDA receptor permeability. We see that in both, the left part of the cell precedes the right part. With persistent Na^+ permeability only, the right part of the cell begins to catch up with the left part as depolarization progresses, with the two parts of the cell depolarizing nearly simultaneously with each

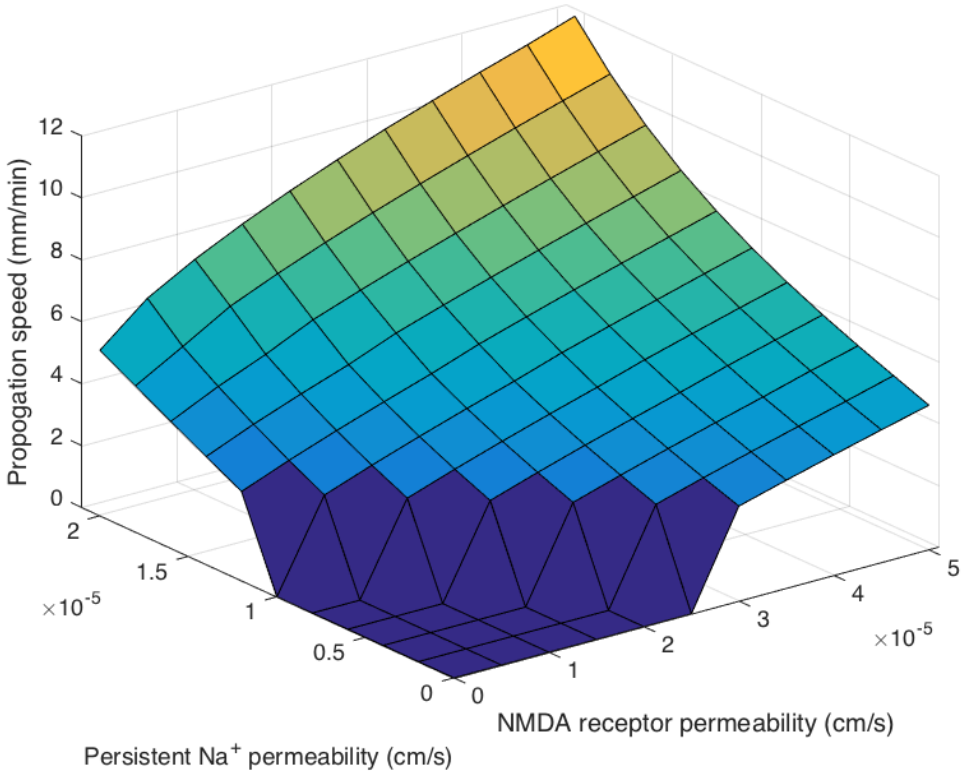

Figure 6.4: Propagation speeds of SD in the staggered model with different permeabilities for the persistent Na^+ channel and the NMDA receptor. Propagation speeds of 0 indicate that SD did not occur.

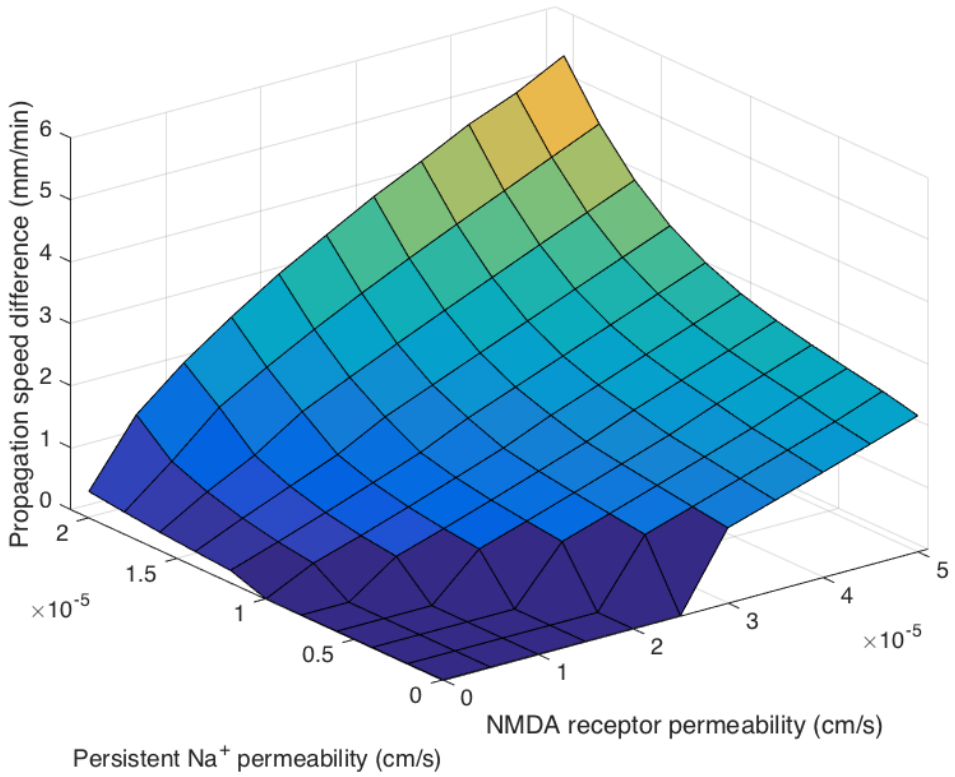

Figure 6.5: The difference in propagation speeds of SD in the staggered model versus the stacked model with different permeabilities for the persistent Na^+ channel and the NMDA receptor. In all cases, the staggered model had faster propagation.

other by the time the left side is approximately 10 mV from the resting potential. With NMDA receptor permeability only, however, the right part does not catch up to the left part until the cell is approximately 20 mV from the resting potential.

This behavior changes with the staggered model. In particular, the right part of the cell catches up to the left part of the cell at approximately the same voltage regardless of the permeabilities. Of particular interest in the staggered model, however, is how the overlap affects the timing. In the stacked model, the two neuronal compartments have identical behavior, but in the staggered model, the point $x = 2.5$ mm has a left part of a neuron and the right part of another neuron. To understand how the two cells interact, we look at the other parts of both of these neurons as well, so that we are looking at two whole cells, with four total values over three points in space. To simplify our discussion, we let n_1^l and n_1^r denote the left and right points, respectively, of the cell extending leftward, while n_2^l and n_2^r denote the left and right points of the cell extending rightward (see Fig. 6.7). In this manner, n_1^r and n_2^l occupy the same point in space. Fig. 6.8 shows the change in membrane potentials of n_1^l, n_1^r, n_2^l, and n_2^r for one such cell pair, along with the extracellular potential at the point in common between the cells. We see that the two cells show matching behaviors, with a delay from one to the next of less than half a second. There is, therefore, a significant difference in the two membrane potentials at any one point.

We observe that the slight depolarization actually begins earlier for n_2^l than it does for n_1^r, so that prior to the actual wave of SD arriving, n_1^l and n_2^l are more similar than n_1^l and n_1^r. We propose that this is due to the gradual change in the extracellular potential leading up to the SD wave. As the extracellular potential decreases, the membrane becomes slightly depolarized. For small variations, the cell remains below the threshold for SD and attempts to adjust back to the resting membrane potential. The right side of each cell reacts to this behavior prior to the arrival of the change in extracellular potential, as the cell has a higher diffusion coefficient than the extracellular space, resulting in the right side of the cell staying closer to the resting potential. Once

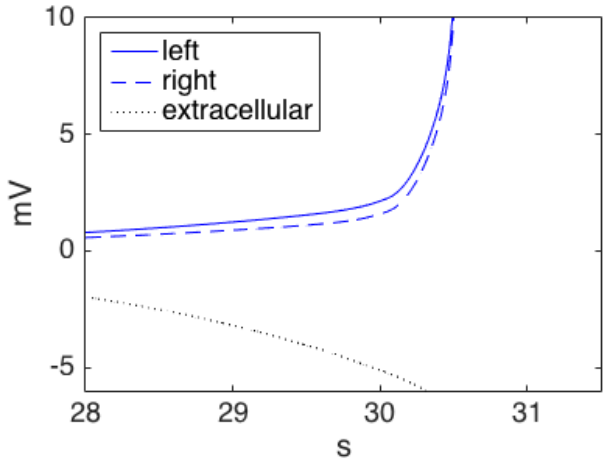

(a)

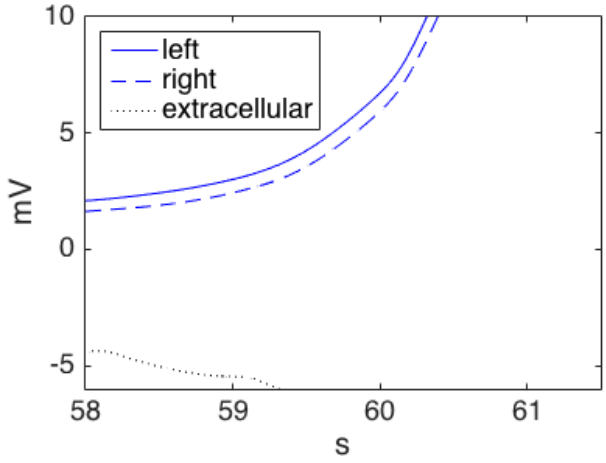

(b)

Figure 6.6: The change in membrane potentials and extracellular potential in the cell at 2.5 mm near the time that the SD wave arrives in the stacked model. (a) shows the potentials for $P_{\mathrm{Na}}^{\mathrm{n,P}} = 2 \times 10^{-5}$ cm/s and $P^{\mathrm{n,NMDA}} = 0$ while (b) shows $P_{\mathrm{Na}}^{\mathrm{n,P}} = 0$ and $P^{\mathrm{n,NMDA}} = 5 \times 10^{-5}$ cm/s. The solid line is the left part of the cell, while the dashed line is the right part of the cell. The dotted line shows the extracellular potential.

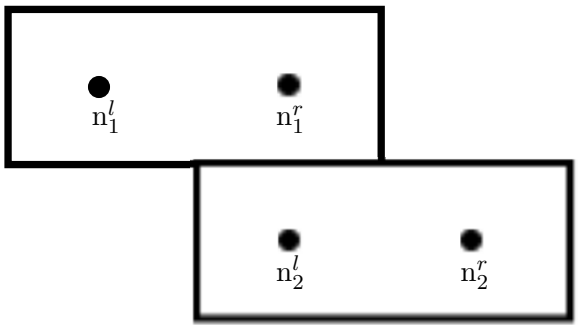

Figure 6.7: One pair of overlapping cells in the staggered model.

the threshold for SD is reached, however, the major changes force both parts of the cell to fully depolarize. We note that the value of this threshold is poorly defined and may be due to any number of factors.

In order to test this theory, we ran simulations with the glial diffusion coefficient set to 0. With the glial diffusion coefficient set to 0, the DC shift has a much smaller magnitude and begins after the depolarization of the membrane (see section 5.2 for details). As expected, the two parts of the cell now show the same behavior, with n_1^l and n_1^r virtually indistinguishable at the start of the depolarization, as shown in Fig. 6.9. We observe, however, that while this explains the difference in depolarization between the two parts of the cell in the staggered model, it does not explain the difference in propagation speed between the stacked and staggered model. In terms of propagation speed, simulations with the glial diffusion coefficient set to 0 showed the same properties as simulations with $d = 0.25$.

6.4 Blocking the NMDA Receptor

To examine the effect of blocking the NMDA receptor on propagation, as opposed to initiation, we ran simulations in which $P^{\mathrm{n,NMDA}}$ was initially non-zero but was changed to zero when the SD wave arrived at 2.5 mm. We then computed the propagation speed, if propagation continued, using the same method as for the other simulations. We found

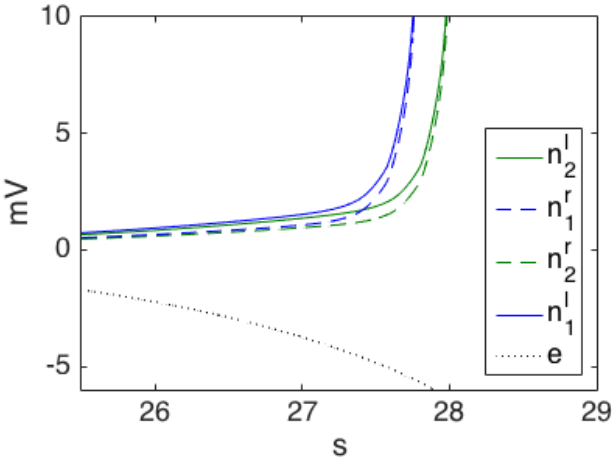

(a)

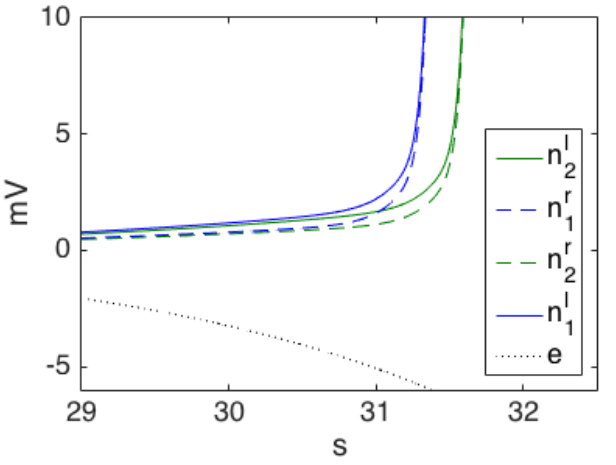

(b)

Figure 6.8: The change in membrane potentials and extracellular potential in the cells at 2.5 mm near the time that the SD wave arrives in the staggered model. (a) shows the potentials for $P_{\mathrm{Na}}^{\mathrm{n,P}} = 2 \times 10^{-5}$ cm/sec and $P^{\mathrm{n,NMDA}} = 0$ while (b) shows $P_{\mathrm{Na}}^{\mathrm{n,P}} = 0$ and $P^{\mathrm{n,NMDA}} = 5 \times 10^{-5}$ cm/sec. The solid lines are the left parts of the cells, while the dashed lines are the right parts of the cells (see Fig. 6.7). The dotted line shows the extracellular potential.

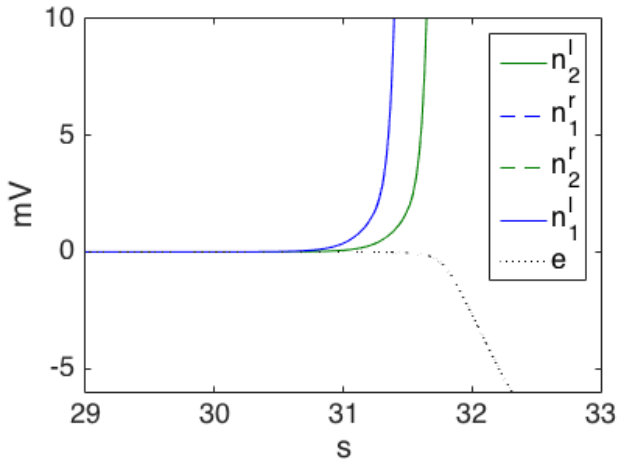

Figure 6.9: The change in membrane potentials and extracellular potential in the cells at 2.5 mm near the time that the SD wave arrives in the staggered model, with $P_{\mathrm{Na}}^{\mathrm{n,P}} = 0$ and $P^{\mathrm{n,NMDA}} = 5 \times 10^{-5}$ cm/sec and the glial diffusion coefficient set to 0. Compare to Fig. 6.8b, where the only difference is that the glial diffusion coefficient is $0.25\alpha_{\mathrm{g}}^0 D_i^*$.

two possible behaviors, depending only on the value of $P_{\mathrm{Na}}^{\mathrm{n,P}}$. For values of $P_{\mathrm{Na}}^{\mathrm{n,P}}$ less than 8×10^{-6} cm/sec, the propagation stopped almost immediately. Several neighboring points were affected by SD, but the time between each successive point reaching the threshold gradually increased until eventually no additional points depolarized. For larger values of $P_{\mathrm{Na}}^{\mathrm{n,P}}$, the propagation speed immediately changed to a slower speed. For those values of $P_{\mathrm{Na}}^{\mathrm{n,P}}$ greater than 1.2×10^{-5} cm/sec, the boundary for SD initiation with only persistent sodium channel permeability, the new propagation speed was equal to the propagation speed when SD was triggered without any NMDA receptors. For the intermediate values, the new propagation speed was an otherwise unseen speed, as the persistent sodium permeability was at an insufficient value to trigger SD in the absence of NMDA receptors. Thus, depending on other parameters, blocking NMDA receptors after SD initiation may either halt or slow down propagation of SD, and the speed after the NMDA receptors are blocked is independent of the original value of $P^{\mathrm{n,NMDA}}$. Fig. 6.10 shows the propagation speeds after blockage for the stacked and staggered

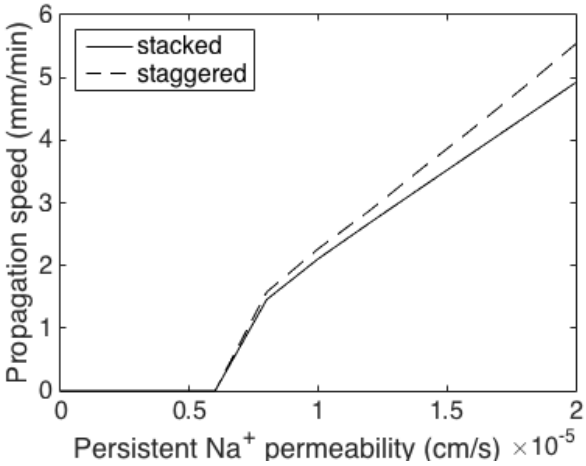

Figure 6.10: Propagation speeds as a function of $P_{\mathrm{Na}}^{\mathrm{n,P}}$ after the NMDA receptor was blocked in the stacked (solid line) and staggered (dashed line) models. Propagation speeds of 0 indicate that SD was halted by NMDA receptor blockage. The propagation speeds were independent of the starting values of $P^{\mathrm{n,NMDA}}$, provided it was sufficient to trigger SD. Compare to the propagation speeds where $P^{\mathrm{n,NMDA}} = 0$ in Fig. 6.3 and Fig. 6.4.

model. Fig. 6.11 shows the two different possible behaviors after the NMDA receptors are blocked.

6.5 Effect of Persistent Na^+ Channel and NMDA Receptors on Recovery Time

In addition to playing a role in the start of SD, the persistent Na^+ channel and NMDA receptor both contribute to the amount of time it takes for the cell to recover. In all of our simulations in which SD occurred, the neuronal membrane potential increased gradually from -70 mV to about -68 mV before spiking to a peak between -10 and 0 mV. The membrane potential then gradually decreased to approximately -40 mV before a sudden drop back slightly past -70 mV. Fig. 6.12 shows the time course of the membrane potentials at 2.5 mm for two example simulations. The shape of the

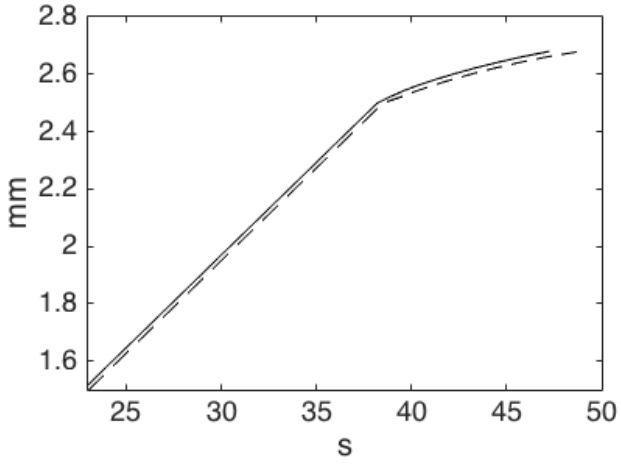

(a)

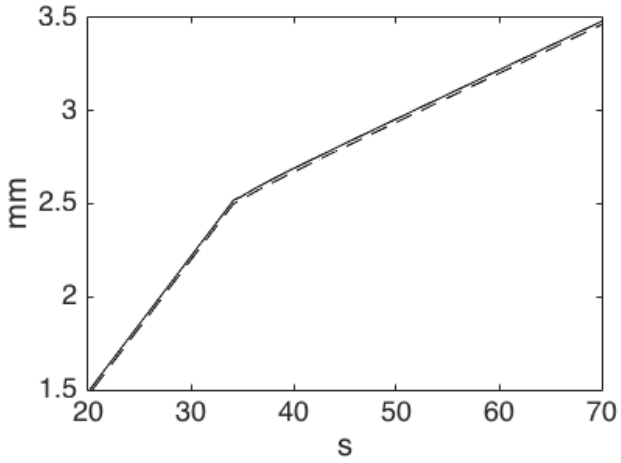

(b)

Figure 6.11: The arrival of the SD wave at each point as a function of time for simulations involving NMDA receptor blockage in the staggered model. For small values of $P_{\mathrm{Na}}^{\mathrm{n,P}}$, the SD wave halts, as shown in (a), while for larger values it continues with a slower speed of propagation, as shown in (b). The change in behavior occurs immediately after the wave hits 2.5 mm, when the NMDA receptors are blocked. The solid line shows the left edge of each cell, while the dashed shows the right edge of each cell.

trace was dependent on the permeabilities of the two channels, but was independent of whether the simulation used the stacked model or the staggered model. To analyze the duration of the depolarization, we examined the time between the spike and the sudden drop back to -70 mV by measuring when $\phi_{\mathrm{n_1e}}$ at 2.5 mm crossed the threshold of -60 mV in each direction. The duration of depolarization was then determined by taking the difference between these two times. We note that, although there is a slight difference in when the two neuronal compartments cross the threshold (see Fig. 6.12), the difference between the durations of the depolarization of the two is on the order of hundredths of a second.

In our simulations with a range of values for both $P_{\mathrm{Na}}^{\mathrm{n,P}}$ and $P^{\mathrm{n,NMDA}}$, we found that the full range of NMDA receptor permeabilities caused a variation in the duration of depolarization of no more than two tenths of a second for fixed values of $P_{\mathrm{Na}}^{\mathrm{n,P}}$, and usually only one tenth of a second. The value of $P_{\mathrm{Na}}^{\mathrm{n,P}}$, on the other hand, significantly affected the length of the depolarization. For $P_{\mathrm{Na}}^{\mathrm{n,P}} = 0$, the depolarization lasted about 9 seconds, whereas for $P_{\mathrm{Na}}^{\mathrm{n,P}} = 2 \times 10^{-5}$ cm/s, it lasted approximately 20 seconds. Fig. 6.13 shows the duration of the depolarization as a function of both permeabilities. The length of the depolarization of the stacked model, in all cases, was between 0.05 and 0.2 seconds shorter than the staggered model.

Increasing the neuronal reabsorption rate ν caused a significant increase in the length of the depolarization for both the stacked and staggered models. In particular, with $\nu = 0.9$, the depolarization lasted approximately 19 seconds for low values of $P_{\mathrm{Na}}^{\mathrm{n,P}}$, while with $\nu = 0.2$, the depolarization lasted only 9 seconds. For high values of $P_{\mathrm{Na}}^{\mathrm{n,P}}$, the change in the length of the depolarization was reduced, but the shape of the depolarization changed. We note that the change in ν had a negligible effect on the propagation speed. Increasing ν can be interpreted as increasing the original glutamate stores within a cell without changing the release rate.

We observe that the variation in the duration of depolarization is primarily a change in how long the membrane is near its peak depolarization, as shown in Fig. 6.14. With

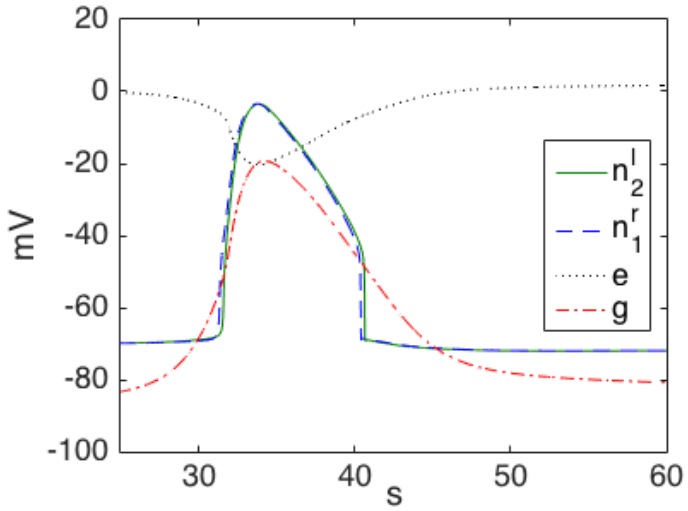

(a)

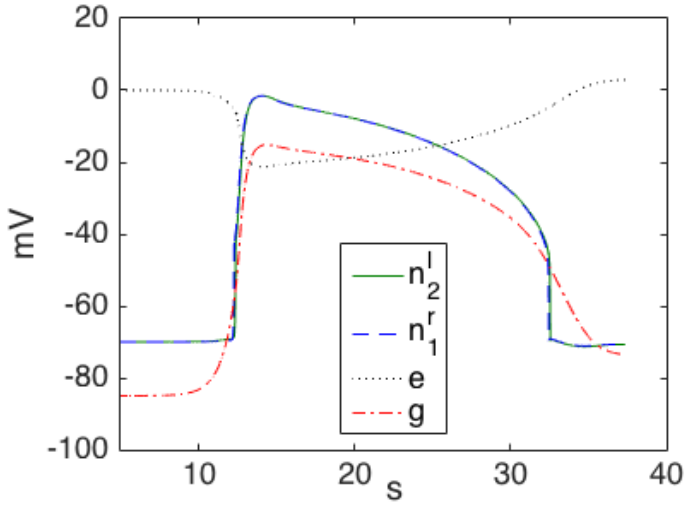

(b)

Figure 6.12: The membrane potentials of all compartments and the extracellular potential recorded through time at 2.5 mm. (a) Staggered model with $P^{\mathrm{n,NMDA}} = 5 \times 10^{-5}$ cm/s and $P_{\mathrm{Na}}^{\mathrm{n,P}} = 0$. (b) Staggered model with $P^{\mathrm{n,NMDA}} = 5 \times 10^{-5}$ cm/s and $P_{\mathrm{Na}}^{\mathrm{n,P}} = 2 \times 10^{-5}$ cm/s. In each, the blue dashed line shows the right edge of one cell (n_1^r) and the green solid line the left edge of the other (n_2^l), while the red dashed and dotted line is the glial membrane potential and the dotted line is the extracellular potential.

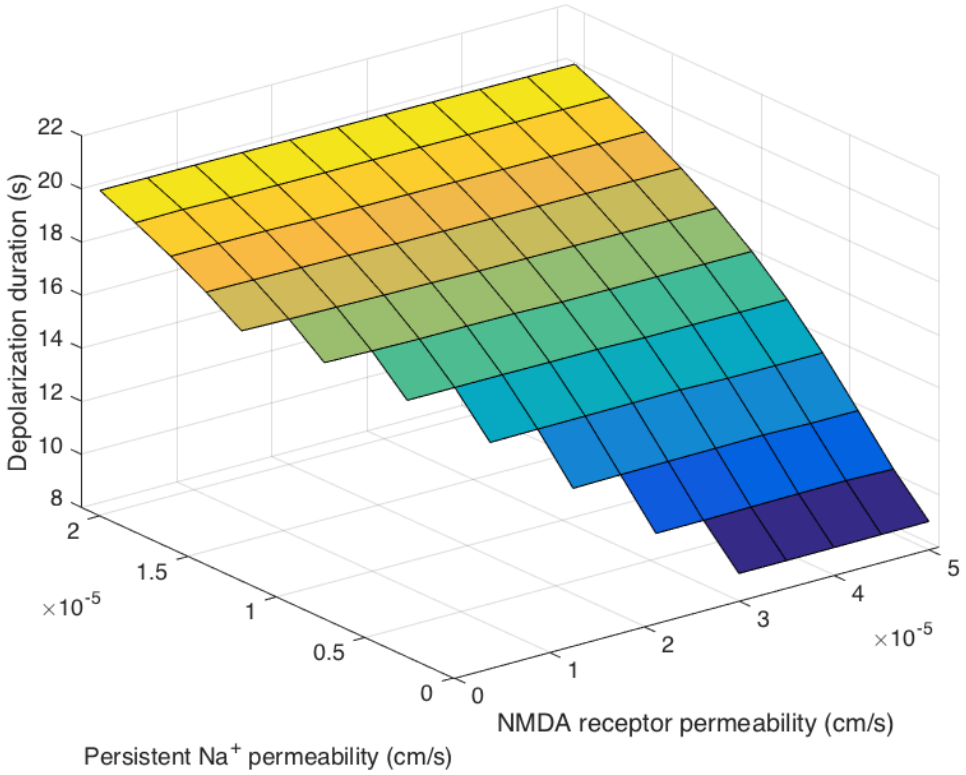

Figure 6.13: The duration of the depolarization as a function of the permeabilities of both the NMDA receptor and the persistent Na^+ channel. The NMDA receptor permeability has negligible effect compared to the persistent Na^+ permeability.

$\nu = 0.2$, the neurons stayed near the peak depolarization only about a second before the membrane potential began to decrease again. With $\nu = 0.9$, however, the membrane potential was near its peak for more than 5 seconds. In conjunction with this, the DC shift maintained its peak for approximately the same amount of time as the membrane depolarization. The DC shift also had a larger magnitude with $\nu = 0.9$ than $\nu = 0.2$, and the overshoot in the extracellular potential following recovery was larger as well. These effects show that the NMDA receptor affects the shape of the DC shift and are in relative agreement with the analysis of the shape of the DC shift by Herreras and Somjen [28], who found that blocking the NMDA receptors eliminated the second hump of the DC shift in the stratus radiatum of the hippocampus.

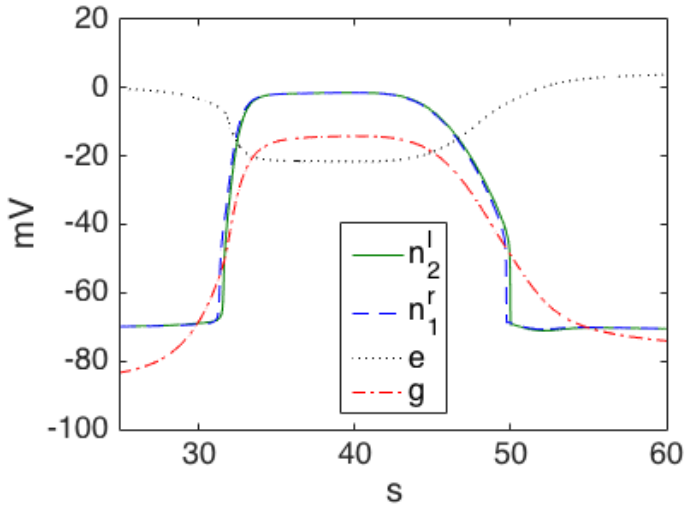

(a)

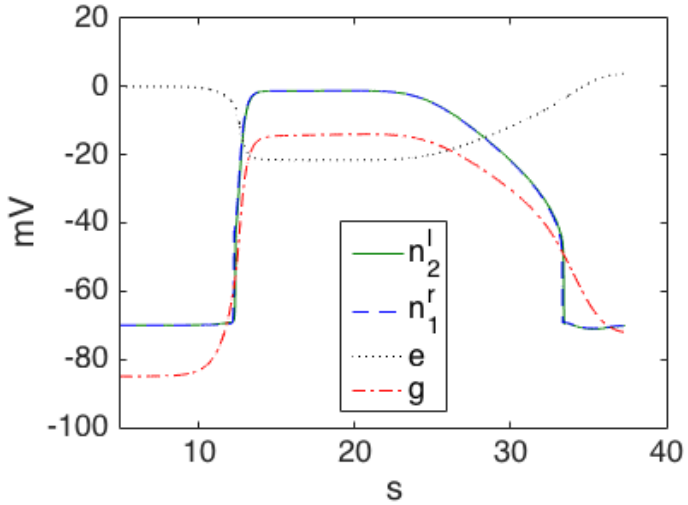

(b)

Figure 6.14: The membrane potentials of all compartments and the extracellular potential recorded through time at 2.5 mm, with a high reabsorption rate of $\nu = 0.9$. (a) Staggered model with $P^{\mathrm{n,NMDA}} = 5 \times 10^{-5}$ cm/s and $P^{\mathrm{n,P}}_{\mathrm{Na}} = 0$. (b) Staggered model with $P^{\mathrm{n,NMDA}} = 5 \times 10^{-5}$ cm/s and $P^{\mathrm{n,P}}_{\mathrm{Na}} = 2 \times 10^{-5}$ cm/s. In each, the blue dashed line shows the right edge of one cell (n_1^r) and the green solid line the left edge of the other (n_2^l), while the red dashed and dotted line is the glial membrane potential and the dotted line is the extracellular potential. Compare to Fig. 6.12.

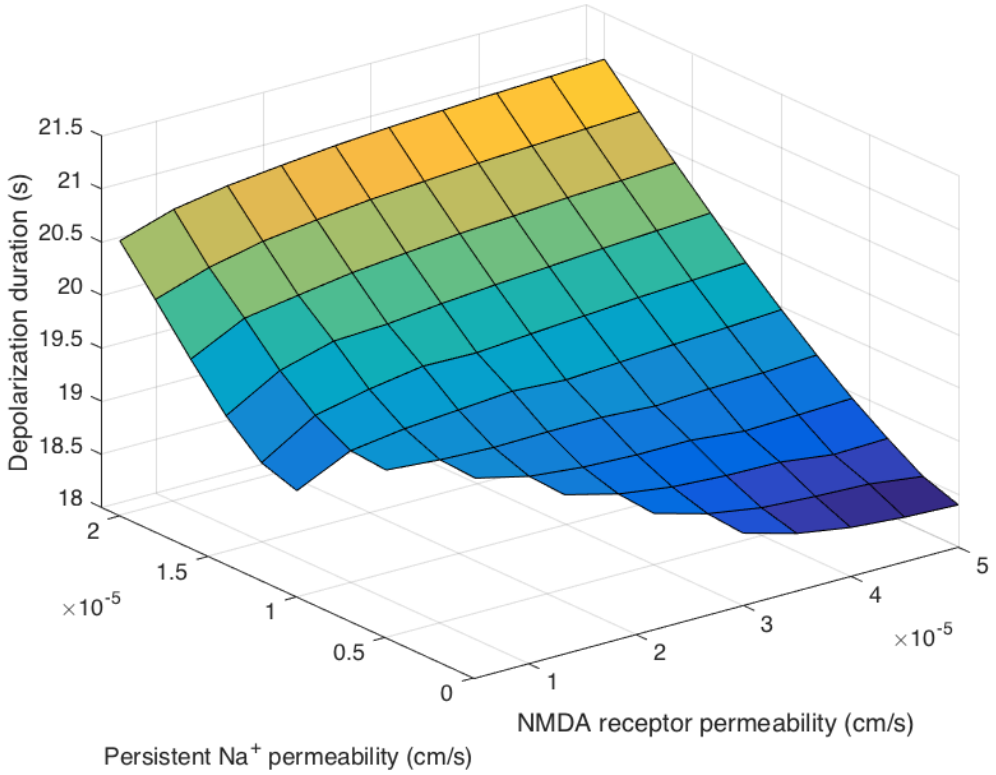

Figure 6.15: The duration of the depolarization as a function of the permeabilities of both the NMDA receptor and the persistent Na^+ channel with $\nu = 0.9$. Compare to Fig. 6.13.

Chapter 7

Two-Dimensional Results

Extending our model into two dimensions allows us to explore some of the spatial patterns that might develop during SD, as well as possible anisotropies in certain variables. We look specifically at the effect of triggering SD in more than one location and anisotropies in the glial gap-junctional coupling. We find that, as in the one-dimensional case, the glial coupling has a significant impact on the DC shift. The basic results of our isotropic two-dimensional simulations and the effects of triggering SD from more than one location are discussed in section 7.1, and the effects of anisotropic glial coupling in section 7.2.

7.1 Triggering SD from One or Two Points

Our basic simulations in two spatial dimensions involve triggering SD at one corner of a one centimeter square region, as described in section 3.7, around $(x, y) = (0, 0)$. The basic simulations are completely isotropic, with all diffusion coefficients equal in both directions and spatially uniform initial conditions. As would be expected, we find a circular expansion of SD away from the corner at which SD was triggered. SD propagates uniformly in all directions, and each point shows the same behavior as any given point in our one-dimensional simulations. Fig. 7.1 shows the extracellular potentials in the

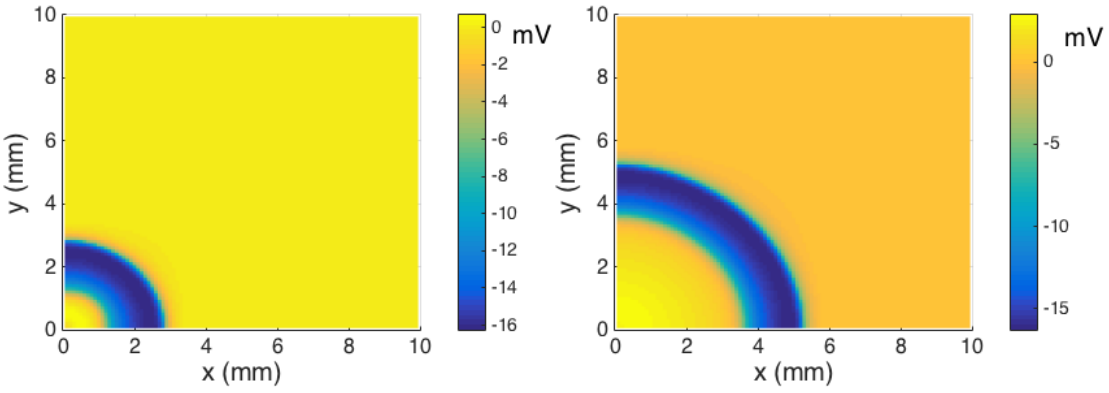

Figure 7.1: The extracellular potential during a basic two-dimensional simulation, (a) 30 seconds and (b) 60 seconds after SD was triggered. The negative DC shift is evident in both, spreading outward, and the positive tail has appeared by the 60 second mark.

region 30 seconds and 60 seconds after SD was first triggered. We can see both the negative DC shift, reaching approximately -16 mV, and the positive tail that goes slightly above 2 mV.

We point out that since the changes in concentration and membrane potentials occur at roughly the same time as the DC shift, the patterns shown by these are the same as the DC shift, so looking at the DC shift is sufficient to understand the general behavior in two dimensions.

When we trigger SD in a region around $(5, 0)$ as well as $(0, 0)$, we find that the initial behavior is a circular expansion around both points. After some time, the two SD waves meet halfway between the starting points, at $(2.5, 0)$, and begin to merge. Fig. 7.2 shows the waves as they meet and merge. After the waves merge, they continue to expand out, as shown in Fig. 7.3. We note that where the two waves merge appears as a sharp bump that travels along $x = 2.5$ at a faster speed than the leading edge of the wave and the curve smoothes out. This is easily understood, as SD is arriving from multiple directions along this line, instead of one direction everywhere else.

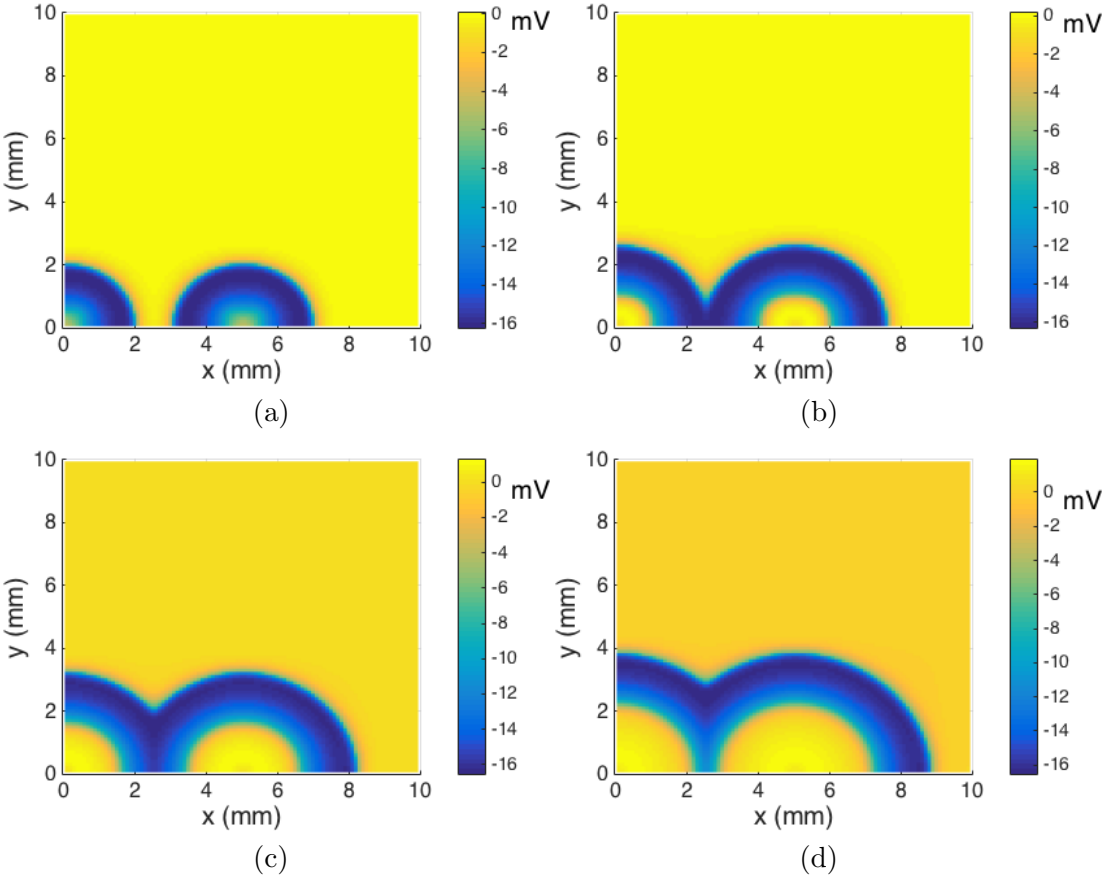

Figure 7.2: The extracellular potential during a two-dimensional simulation in which SD was triggered at two points, (a) 20 seconds, (b) 27.5 seconds, (c) 35 seconds, and (d) 42.5 seconds after SD was triggered. The two waves are both circular at first before meeting, and the intersection of the two curves gradually smoothes out as time passes.

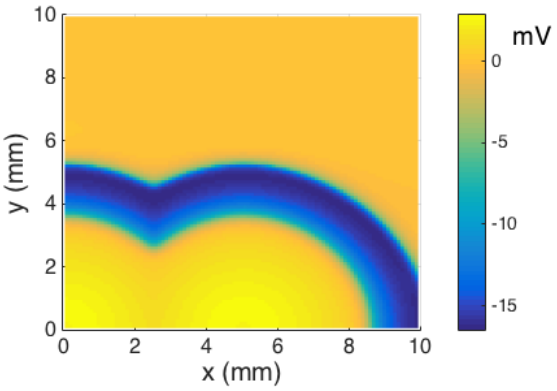

Figure 7.3: The extracellular potential during a two-dimensional simulation in which SD was triggered at two points, 60 seconds after SD was triggered.

7.2 Anisotropic Glial Coupling

For some simulations, we adjusted the glial diffusion coefficient in different directions to simulate anisotropic glial gap-junctional coupling. Simulations were run with the glial diffusion coefficients in the x-direction being multiplied by a different factor d_x than in the y-direction, d_y. A similar factor could be introduced for the extracellular diffusion coefficients to account for anisotropy there as well, or the diffusion coefficients in general could be viewed as a tensor. Such changes could introduce interesting patterns in the SD wave but are not investigated here. We set

$$D_i^{\mathrm{n}} = 0,$$
$$D_i^{\mathrm{e}} = D_i^* \alpha_{\mathrm{e}} / \lambda^2$$

in both directions and

$$D_{i,x}^{\mathrm{g}} = d_x D_i^* \alpha_{\mathrm{g}}^0 / \lambda^2,$$
$$D_{i,y}^{\mathrm{g}} = d_y D_i^* \alpha_{\mathrm{g}}^0 / \lambda^2.$$

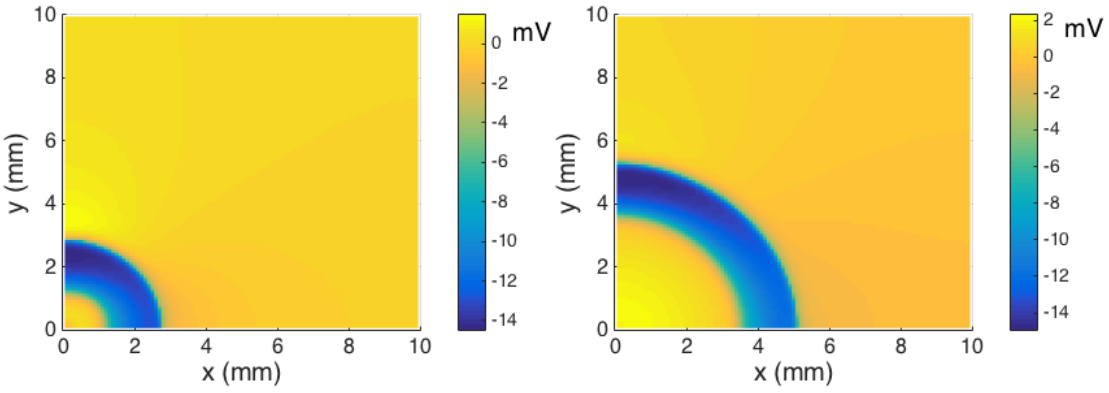

Figure 7.4: The extracellular potential during a two-dimensional simulation (a) 30 and (b) 60 seconds after SD was triggered in one corner, with $d_x = 0.125$ and $d_y = 0.25$. The direction with larger glial coupling shows a greater DC shift magnitude, as evidenced by the darker region near the y-axis.

The isotropic simulations had $d_x = d_y = 0.25$. The various anisotropic simulations we ran had $d_x = 0$ and $d_y = 0.25$, $d_x = 0.125$ and $d_y = 0.25$, and $d_x = 0.25$ and $d_y = 0.125$.

As in the one-dimensional case discussed in section 5.2, changing glial gap-junctional coupling in this manner has a significant effect on the DC shift and the speed of propagation, but a much smaller effect on other aspects of SD. In particular, with anisotropic glial coupling, the magnitude of the DC shift varies depending on what area of the wave we look at, as shown in Fig. 7.4 for $d_x = 0.125$ and $d_y = 0.25$. The leading edge in the direction with the larger diffusion coefficient has a larger magnitude than the direction with the smaller DC shift, shown by the darker region along the y-axis than the x-axis. In addition, a slight difference in propagation speed in the two directions can be detected, as after 60 seconds, the potential at $(5, 0)$ is just beginning to decrease, while at the same time the potential at $(0, 5)$ is already near its minimum. We note that the effect of $d_x = 0.25$ and $d_y = 0.125$ is identical with the x and y-axes switched, as that is the only asymmetry of the system in our simulations where SD is triggered only around $(0, 0)$.

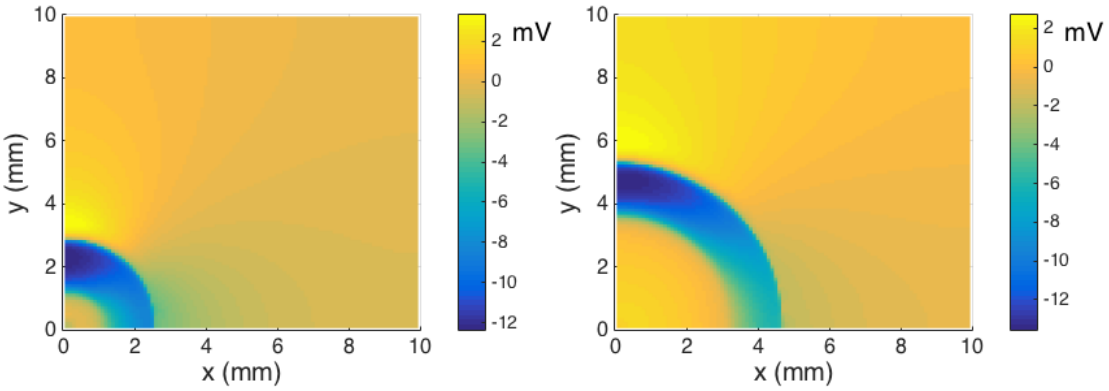

Figure 7.5: The extracellular potential during a two-dimensional simulation (a) 30 and (b) 60 seconds after SD was triggered in one corner, with $d_x = 0$ and $d_y = 0.25$. The direction with larger glial coupling shows a greater DC shift magnitude, as evidenced by the darker region near the y-axis, and the speed of propagation is faster in that direction as well.

The same features exist for the simulation with $d_x = 0$ and $d_y = 0.25$, with more dramatic differences. Here, the difference in the magnitude of the DC shift in different directions is greater, and the different propagation speeds are much easier to see. Fig. 7.5 shows the extracellular potential in this simulation after 30 and 60 seconds.

In addition, the extracellular potential across the entire 1 cm square domain is affected in the anisotropic case. In the isotropic case, the extracellular potential is uniform away from the propagating wave, whereas in the anisotropic case, the extracellular potential varies radially. We first consider $d_x = 0.125$ and $d_y = 0.25$ (Fig. 7.4). Since the extracellular potential at $(10, 10)$ is always set to 0, the extracellular potential near the diagonal is close to 0, but decreases slightly toward the x-axis and increases slightly toward the y-axis. Thus in the direction of smaller glial coupling, the extracellular potential has a gradual decrease prior to the arrival of SD, while in the direction of greater glial coupling, the extracellular potential has a positive shift prior to the negative shift when SD arrives. Again, the simulation with $d_x = 0$ and $d_y = 0.25$ (Fig. 7.5) shows the

same behavior with greater differences in the two directions.

To understand this phenomenon, we look more closely at the simulation with $d_x = 0$ and $d_y = 0.25$. The entire extracellular space is affected at least slightly by the DC shift almost immediately after the start of the simulation. After six seconds of simulated time, $\phi_e(10, 0)$ is approximately -0.06 mV and $\phi_e(0, 10)$ is approximately 0.11 mV. By ten seconds, these are -0.12 and 0.19 mV, respectively, even though the main part of the SD wave has not yet reached even $(1.5, 0)$ or $(0, 1.5)$. By comparison, in the isotropic case, these values are approximately 1×10^{-5} mV after six seconds and 1×10^{-4} mV after ten seconds. We suggest that there is some small degree of extracellular potential change that propagates very quickly through the entire space. In the isotropic case, if this occurs at all, the change is indetectable because our equations for the extracellular potential are algebraic and fix $\phi_e(10, 10) = 0$. In the anisotropic case, the difference between the two spatial dimensions results in these changes being detectable, as propagation occurs more swiftly in the direction with increased coupling than in the direction with decreased coupling.

This hypothesis fits in with the discussion in section 5.2 of glial coupling creating an electrotonic effect that behaves somewhat similarly to action potential propagation, as the speeds necessary for such propagation are closer to the speed of action potential propagation, which is on the order of mm/ms, than to diffusion [69].

We note that the DC shift is the only feature which shows the directional variation in magnitude and overall spatial variation. The membrane potentials and concentrations all reach approximately the same extremes in both directions, as shown in Fig. 7.6, which has the extracellular and membrane potentials and extracellular concentrations through time at two points, $(3, 0)$ and $(0, 3)$, with $d_x = 0$ and $d_y = 0.25$. The extracellular potentials show the dramatic differences expected based on Fig. 7.5, with the addition of a slight oscillation due to the fast propagation of small waves of potential change. The neuronal membrane potential and extracellular concentrations are virtually identical except for the arrival time. The glial membrane potential is the only

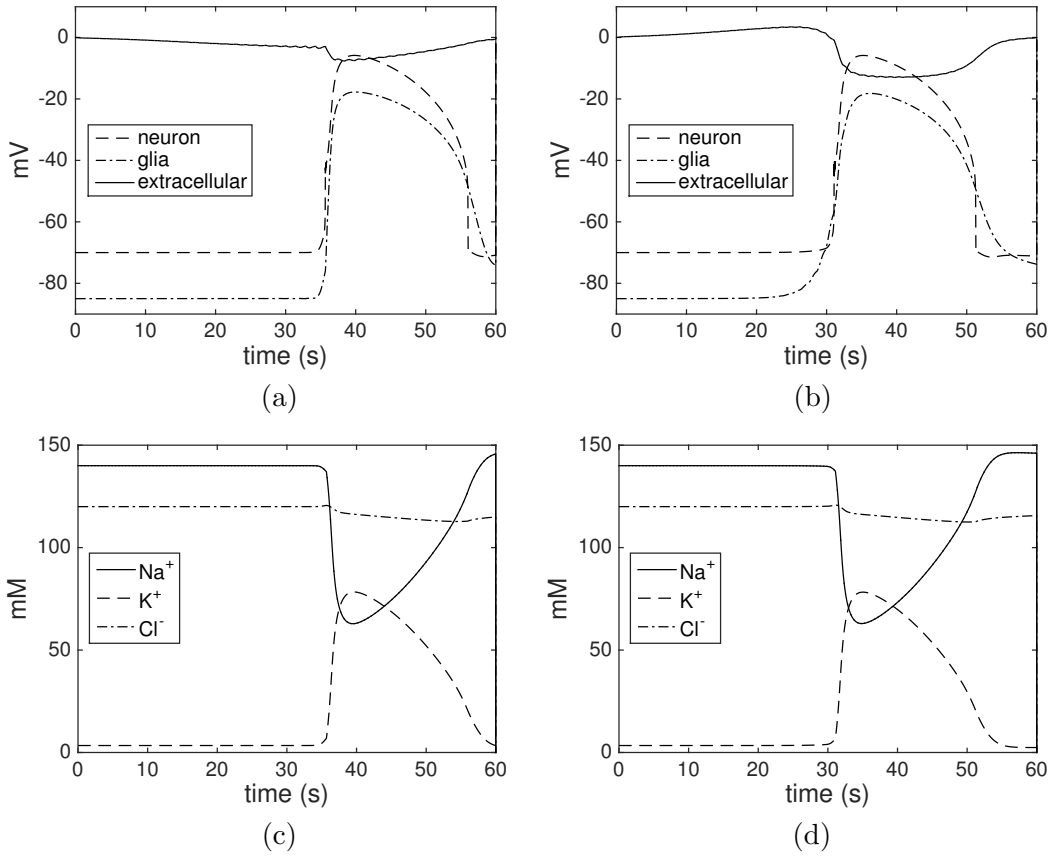

Figure 7.6: The extracellular and membrane potentials ((a), (b)) and extracellular concentrations ((c), (d)) at two points through time when $d_x = 0$ and $d_y = 0.25$.. The two points are $(3, 0)$ ((a), (c)) and $(0, 3)$ ((b), (d)). For the potentials, in (a) and (b), the extracellular potential is the solid line, the neuronal membrane potential is the dashed line, and the glial membrane potential is the dashed and dotted line. We see that the extracellular potential begins to change immediately, decreasing for $(3, 0)$ and increasing for $(0, 3)$, and the glial depolarization begins more gradually for $(0, 3)$, but otherwise the only significant difference between the two points is that SD arrives earlier at $(0, 3)$. For the extracellular concentrations, in (c) and (d), the solid line is the Na^+ concentration, the dashed line the K^+ concentration, and the dashed and dotted line the Cl^- concentration. Here the only difference is when SD arrives.

other feature that depends significantly on the direction, as the glia begin to depolarize several seconds prior to the neuronal depolarization in the direction with greater glial coupling. However, even that does not begin to change immediately after the start of the simulation as the extracellular potential does. In addition, we note that the amount of time it takes to recover is largely independent of the direction, with about 20 seconds between the initial neuronal depolarization and the start of hyperpolarization during recovery.

Further simulations were done in which SD was triggered at two points and the glial coupling was anisotropic. Again, the general behavior is similar, with a greater DC shift and faster propagation in the direction of greater glial coupling. Recall that the meeting point of the two waves travels along the line $x = 2.5$ mm. If the glial coupling is greater in the y direction, we find that once the two waves merge, the greatest magnitude for the DC shift occurs along $x = 2.5$ mm, where the two waves connect. Fig. 7.7 shows the extracellular potential for the simulation with $d_x = 0.125$ and $d_y = 0.25$ after 30 seconds, when the two waves are just starting to merge, and after 60 seconds, when the two waves have fully merged. The same times are shown in Fig. 7.8 for $d_x = 0$ and $d_y = 0.25$.

A simulation with $d_x = 0.25$ and $d_y = 0.125$ was also run with two points triggered. In this case, the larger magnitude for the DC shift is traveling along the x-axis, while the smaller magnitude travels in the y-direction. The DC shift along $x = 2.5$ mm has a slightly larger magnitude than the neighboring points, as in the other simulations, but is still much smaller than the leading edge in the x-direction. The extracellular potential for this simulation after 30 and 60 seconds is shown in Fig. 7.9.

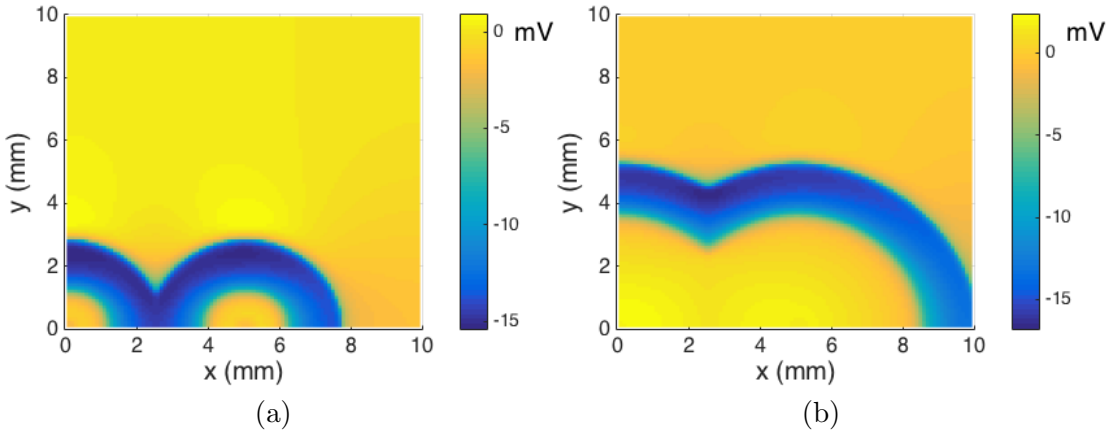

Figure 7.7: The extracellular potential during a two-dimensional simulation (a) 30 and (b) 60 seconds after SD was triggered in two locations, with $d_x = 0.125$ and $d_y = 0.25$. The direction with larger glial coupling shows a greater DC shift magnitude, as evidenced by the darker region near the y-axis.

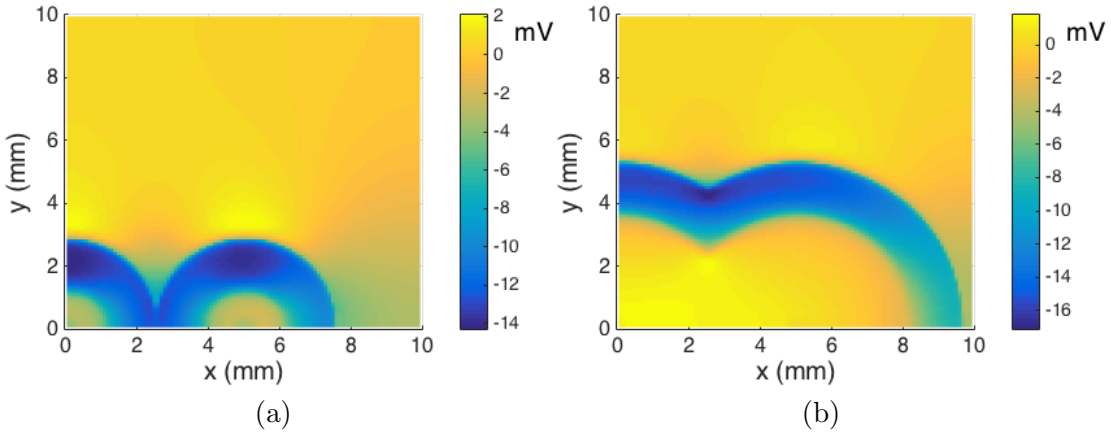

Figure 7.8: The extracellular potential during a two-dimensional simulation (a) 30 and (b) 60 seconds after SD was triggered in two locations, with $d_x = 0$ and $d_y = 0.25$. The direction with larger glial coupling shows a greater DC shift magnitude, as evidenced by the darker region near the y-axis.

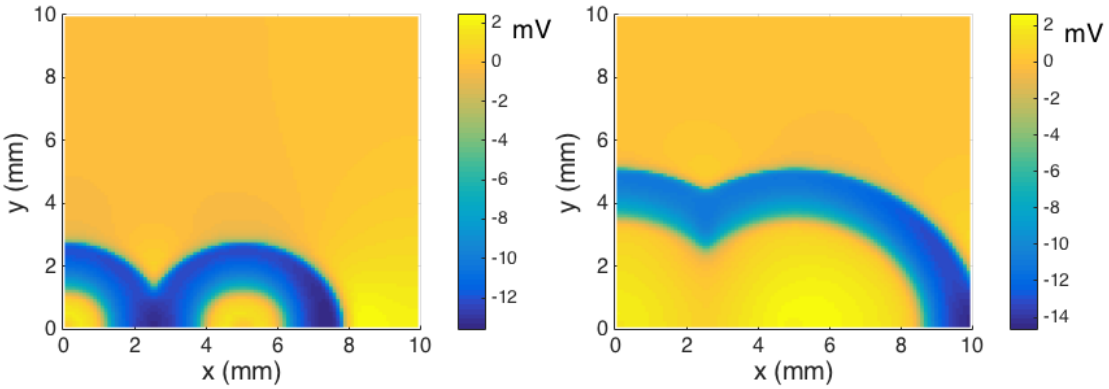

Figure 7.9: The extracellular potential during a two-dimensional simulation (a) 30 and (b) 60 seconds after SD was triggered in two locations, with $d_x = 0.25$ and $d_y = 0.125$. The direction with larger glial coupling shows a greater DC shift magnitude, as evidenced by the darker region near the x-axis.

Chapter 8

Conclusion and Discussion

We have examined four different variations on a physiologically detailed model of SD. In Chapter 4, we looked at a version with two compartments incorporating intracompartmental fluid flow. With these simulations, we found that incorporating intracompartmental fluid flow with expected physiological values had only a small effect on the features of SD, while varying the stiffness constant could have a significant effect on the extent of cell swelling and, by extension, the recovery of the concentrations. In Chapter 5, we studied the effects of several parameters controlling K^+ dynamics in a version with neuronal, glial, and extracellular compartments. These simulations showed that the glial compartment has a major effect on the DC shift and propagation speed of SD. In Chapter 6, we split the neuronal compartment into two separate compartments, creating a four-compartment model, and added the NMDA receptor to the collection of ion channels on the neuronal membrane. We found that the NMDA receptor and the persistent Na^+ channel could play similar roles in the initiation and propagation of SD, and that the NMDA receptor could have a significant impact on the shape of both the DC shift and the membrane potential traces. In addition, incorporating cell overlap resulted in an increased speed of propagation, especially with the NMDA receptor involved. Chapter 7 expanded the three-compartment model to two spatial dimensions

and examined the spatial properties of SD as a result of triggering SD at multiple points and anisotropic glial gap-junctional coupling, providing further evidence that the glial compartment has a significant impact on the DC shift.

Our computational results show that the propagation speed of SD is dependent on many factors, including intracompartmental flow rates, the glial compartment, the magnitude of channel permeabilities, and the proximity of cells to each other. Propagation occurs as each cell is affected by its environment in such a way as to reach the threshold of depolarization, and an increase in propagation speed corresponds to a change that either decreases the threshold for cells to depolarize (for instance, a reduction in the Na^+/K^+ ATPase strength, which raises the resting membrane potential) or causes cells to reach that threshold faster (for instance, increasing the permeability of a neuronal ion channel). Most of our simulations involve the latter. Intracompartmental flow in the neurons moves in the direction of propagation, carrying ions with it and therefore causing the intracellular concentrations to begin changing slightly earlier than without intracompartmental flow. Increasing glial gap-junctional coupling causes the DC shift to propagate ahead of the neuronal depolarization, which we hypothesize leads to the cell reaching the threshold faster. Increasing glial K^+ permeability slows propagation with low gap-junctional coupling, as it draws K^+ out of the extracellular space. The reduced extracellular K^+ results in the cell taking longer to reach the threshold. While this may happen with greater gap-junctional coupling as well, the increase in K^+ in the glial cells causes the DC shift, with its close connection to the glial depolarization, to propagate even faster. Finally, having cell overlap in the four-compartment model means that each cell is affected more immediately by the previous cell's depolarization. Specifically, the rapid depolarization of both parts of one cell happens simultaneously, so that K^+ and glutamate are released directly into the extracellular space of the next cell, rather than having to diffuse into that space.

SD is a highly complex phenomenon, and the tight coupling of ion concentrations, electrostatic potential, and cell volume results in subtleties that may be difficult to

predict. Exploring the roles of fluid flow, glial cells, the NMDA receptor, and cell proximity, we find that a physiologically detailed mathematical model can reveal some of these subtleties.

References

[1] George G. Somjen. *Ions in the Brain*. Oxford University Press, 2004.

[2] A. Charles and K.C. Brennan. Cortical spreading depression – new insights and persistent questions. *Cephalalgia*, 29:1115–1124, 2009.

[3] J.P. Dreier. The role of spreading depression, spreading depolarization and spreading ischemia in neurological disease. *Nat Med*, 17(4):439–447, 2011.

[4] Alfred Lehmenkühler and PG Aitken. *Migraine: Basic Mechanisms and Treatment:[Proceedings of the International Symposium Migraine, Basic Mechanisms and Treatment, Held in Münster (Germany) from March 8-11, 1992]*. Urban & Schwarzenberg, 1993.

[5] Nouchine Hadjikhani, Margarita Sanchez del Rio, Ona Wu, Denis Schwartz, Dick Bakker, Bruce Fischl, Kenneth K. Kwong, F. Michael Cutrer, Bruce R. Rosen, Roger B.H. Tootell, A. Gregory Sorensen, and M. A. Moskowitz. Mechanisms of migraine aura revealed by functional MRI in human visual cortex. *P Nat Acad Sci USA*, 98(8):4687–4692, 2001.

[6] PC Tfelt-Hansen. History of migraine with aura and cortical spreading depression from 1941 and onwards. *Cephalalgia*, 2009.

[7] Markus A Dahlem and Nouchine Hadjikhani. Migraine aura: retracting particle-like waves in weakly susceptible cortex. *PLoS One*, 4(4):e5007, 2009.

[8] Martin Lauritzen, Jens Peter Dreier, Martin Fabricius, Jed A Hartings, Rudolf Graf, and Anthony John Strong. Clinical relevance of cortical spreading depression in neurological disorders: migraine, malignant stroke, subarachnoid and intracranial hemorrhage, and traumatic brain injury. *J Cerebr Blood F Met*, 31(1):17–35, 2010.

[9] R.M. Miura, H. Huang, and J.J. Wylie. Cortical spreading depression: An enigma. *Eur Phys J-Spec Top*, 147:287–302, 2007.

[10] Aristides AP Leao. Spreading depression of activity in the cerebral cortex. *J Neurophysiol*, 7(6):359–390, 1944.

[11] Aristides AP Leão. Further observations on the spreading depression of activity in the cerebral cortex. *Journal of neurophysiology*, 10(6):409–414, 1947.

[12] J Bures, O Buresova, and J Krivanek. The meaning and significance of Leão's spreading depression. *Anais da Academia Brasileira de Ciencias*, 56(4):385, 1984.

[13] Ali Gorji, Dieter Scheller, Heidrun Straub, Frank Tegtmeier, Rüdiger Köhling, Jörg-Michael Höhling, Ingrid Tuxhorn, Alois Ebner, Peter Wolf, Hans Werner Panneck, Falk Oppel, and Erwin-Josef Speckmann. Spreading depression in human neocortical slices. *Brain Research*, 906:74–83, 2001.

[14] Hiss Martins-Ferreira, Maiken Nedergaard, and Charles Nicholson. Perspectives on spreading depression. *Brain research reviews*, 32(1):215–234, 2000.

[15] G.G. Somjen. Mechanisms of spreading depression and hypoxic spreading depression-like depolarization. *Physiological reviews*, 81(3):1065, 2001.

[16] Charles Nicholson. Diffusion and related transport mechanisms in brain tissue. *Reports on progress in Physics*, 64(7):815, 2001.

[17] David W Busija, Ferenc Bari, Ferenc Domoki, Takashi Horiguchi, and Katsuyoshi Shimizu. Mechanisms involved in the cerebrovascular dilator effects of cortical spreading depression. *Progress in neurobiology*, 86(4):417–433, 2008.

[18] KC Brennan and Andrew Charles. An update on the blood vessel in migraine. *Current opinion in neurology*, 23(3):266–274, 2010.

[19] Daniela Pietrobon and Michael A Moskowitz. Chaos and commotion in the wake of cortical spreading depression and spreading depolarizations. *Nat Rev Neurosci*, 15(6):379–393, 2014.

[20] Bas-Jan Zandt, Bennie ten Haken, Michel JAM van Putten, and Markus A Dahlem. How does spreading depression spread? physiology and modeling. *Rev Neuroscience*, 26(2):183–198, 2015.

[21] Jens P Dreier and Clemens Reiffurth. The stroke-migraine depolarization continuum. *Neuron*, 86(4):902–922, 2015.

[22] Yina Wei, Ghanim Ullah, and Steven J. Schiff. Unification of neuronal spikes, seizures, and spreading depression. *Neurobiology of Disease*, 34(35):11733–11743, 2014.

[23] RP Kraig and C Nicholson. Extracellular ionic variations during spreading depression. *Neuroscience*, 3(11):1045–1059, 1978.

[24] Takahiro Takano, Guo-Feng Tian, Weiguo Peng, Nanhong Lou, Ditte Lovatt, Anker J Hansen, Karl A Kasischke, and Maiken Nedergaard. Cortical spreading depression causes and coincides with tissue hypoxia. *Nature neuroscience*, 10(6):754–762, 2007.

[25] T Mazel, F Richter, L Vargová, and E Syková. Changes in extracellular space volume and geometry induced by cortical spreading depression in immature and adult rats. *Physiological research*, 51:S85–S94, 2002.

[26] Martin Fabricius, Leif H Jensen, and Martin Lauritzen. Microdialysis of interstitial amino acids during spreading depression and anoxic depolarization in rat neocortex. *Brain research*, 612(1):61–69, 1993.

[27] Trent R Anderson and R David Andrew. Spreading depression: imaging and blockade in the rat neocortical brain slice. *Journal of neurophysiology*, 88(5):2713–2725, 2002.

[28] O. Herreras and George G. Somjen. Analysis of potential shifts associated with recurrent spreading depression and prolonged unstable spreading depression induced by microdialysis of elevated K^+ in hippocampus of anesthetized rats. *Brain Research*, 610:283–294, 1993.

[29] Eiichi Sugaya, Michiaki Takato, and Yukifumi Noda. Neuronal and glial activity during spreading depression in cerebral cortex of cat. *J Neurophysiol*, 38:822–841, 1975.

[30] George G Somjen. Electrogenesis of sustained potentials. *Prog Neurobiol*, 1:199–237, 1973.

[31] S. Canals, I. Marakova, L. López-Aquado, C. Largo, J. M. Ibarz, and O. Herreras. Longitudinal depolarization gradients along the somatadendritic axis of CA1 pyramidal cells: A novel feature of spreading depression. *J Neurophysiol*, 94:943–951, 2005.

[32] Maurizio De Fusco, Roberto Marconi, Laura Silvestri, Luigia Atorino, Luca Rampoldi, Letterio Morgante, Andrea Ballabio, Paolo Aridon, and Giorgio Casari. Haploinsufficiency of ATP1A2 encoding the Na^+/K^+ pump $\alpha 2$ subunit associated with familial hemiplegic migraine type 2. *Nature genetics*, 33(2):192–196, 2003.

[33] Kaate RJ Vanmolkot, Esther E Kors, Ulku Turk, Dylsad Turkdogan, Antoine Keyser, Ludo AM Broos, Sima Kheradmand Kia, Jeroen JMW van den Heuvel,

David F Black, Joost Haan, et al. Two de novo mutations in the na, k-atpase gene atp1a2 associated with pure familial hemiplegic migraine. *Eur J Hum Gen*, 14(5):555–560, 2006.

[34] B. Grafstein. Mechanism of spreading cortical depression. *J Neurophysiol*, 19(2):154–171, 1956.

[35] A Van Harreveld. Compounds in brain extracts causing spreading depression of cerebral cortical activity and contraction of crustacean muscle. *Journal of neurochemistry*, 3(4):300–315, 1959.

[36] A Van Harreveld. Two mechanisms for spreading depression in the chicken retina. *Journal of neurobiology*, 9(6):419–431, 1978.

[37] Kenneth H Reid, Roger Marrannes, and Albert Wauquier. Spreading depression and central nervous system pharmacology. *Journal of pharmacological methods*, 19(1):1–21, 1988.

[38] Carlota Largo, Geoffrey C Tombaugh, Peter G Aitken, Oscar Herreras, and George G Somjen. Heptanol but not fluoroacetate prevents the propagation of spreading depression in rat hippocampal slices. *Journal of neurophysiology*, 77(1):9–16, 1997.

[39] Trent A. Basarsky, Stephen N. Duffy, R. David Andrew, and Brian A. MacVicar. Imaging spreading depression and associated intracellular calcium waves in brain slices. *J Neurosci*, 18(18):7189–7199, September 1998.

[40] Martin Lauritzen and Anker Jon Hansen. The effect of glutamate receptor blockade on anoxic depolarization and cortical spreading depression. *Journal of Cerebral Blood Flow & Metabolism*, 12(2):223–229, 1992.

[41] Roger Marrannes, Roland Willems, Erik De Prins, and Albert Wauquier. Evidence

for a role of the N-methyl-D-aspartate (NMDA) receptor in cortical spreading depression in the rat. *Brain research*, 457(2):226–240, 1988.

[42] Maiken Nedergaard, Arthur J. L. Cooper, and Steven A. Goldman. Gap junctions are required for the propagation of spreading depression. *J Neurobiol*, 28(4):433–444, 1995.

[43] PL Durham and FG Garrett. Neurological mechanisms of migraine: potential of the gap-junction modulator tonabersat in prevention of migraine. *Cephalalgia*, 29(s2):1–6, 2009.

[44] H. Martins-Ferreira and L. J. Ribeiro. Biphasic effects of gap-junctional uncoupling agents on the propagation of retinal spreading depression. *Braz J Med Biol Res*, 28:991–994, 1995.

[45] Martin Theis, Regina Jauch, Lang Zhuo, Dina Speidel, Anke Wallraff, Britta Döring, Christian Frisch, Goran Söhl, Barbara Teubner, Carsten Euwens, Joseph Huston, Christian Steinhäuser, Albee Messing, Uwe Heinemann, and Klaus Willecke. Accelerated hippocampal spreading depression and enhanced locomotory activity in mice with astrocyte-directed inactivation of connexin43. *J Neurosci*, 23(3):766–776, February 2003.

[46] K. Tamura, B. Alessandri, A. Heimann, and O. Kempski. The effect of a gap-junction blocker, carbenoxolone, on ischemic brain injury and cortical spreading depression. *Neuroscience*, 194:262–271, 2011.

[47] H. Kager, W. J. Wadman, and G. G. Somjen. Simulated seizures and spreading depression in a neuron model incorporating interstitial space and ion concentrations. *J Neurophysiol*, 84:495–512, 2000.

[48] H. Kager, W. J. Wadman, and G. G. Somjen. Conditions for the triggering of

spreading depression studied with computer simulations. *Journal of Neurophysiology*, 88:2700–2712, 2002.

[49] H. Kager, W. J. Wadman, and G. G. Somjen. Seizure-like afterdischarges simulated in a model neuron. *Journal of Computational Neuroscience*, 22:105–128, 2007.

[50] DG Fujikawa, JS Kim, AH Daniels, AF Alcaraz, and TB Sohn. In vivo elevation of extracellular potassium in the rat amygdala increases extracellular glutamate and aspartate and damages neurons. *Neuroscience*, 74(3):695–706, 1996.

[51] JM Crowder, MJ Croucher, HF Bradford, and JF Collins. Excitatory amino acid receptors and depolarization-induced Ca^{2+} influx into hippocampal slices. *Journal of neurochemistry*, 48(6):1917–1924, 1987.

[52] Nicholas P Poolos and Jeffery D Kocsis. Elevated extracellular potassium concentration enhances synaptic activation of N-methyl-D-aspartate receptors in hippocampus. *Brain research*, 508(1):7–12, 1990.

[53] Julia Makarova, José M Ibarz, Santiago Canals, and Oscar Herreras. A steady-state model of spreading depression predicts the importance of an unknown conductance in specific dendritic domains. *Biophysical journal*, 92(12):4216–4232, 2007.

[54] Julia Makarova, Valeri A Makarov, and Oscar Herreras. Generation of sustained field potentials by gradients of polarization within single neurons: a macroscopic model of spreading depression. *Journal of neurophysiology*, 103(5):2446–2457, 2010.

[55] John R. Cressman, Ghanim Ullah, Jokubas Ziburkus, Steven J. Schiff, and Ernest Barreto. The influence of sodium and potassium dynamics on excitability, seizures, and the stability of persistent states: I. single neuron dynamics. *Journal of Computational Neuroscience*, 26:159–170, 2009.

[56] Ghanim Ullah, John R. Cressman, Ernest Barreto, and Steven J. Schiff. The influence of sodium and potassium dynamics on excitability, seizures, and the stability

of persistent states: II. network and glial dynamics. *Journal of Computational Neuroscience*, 26:171–183, 2009.

[57] Henry C. Tuckwell and Robert M. Miura. A mathematical model of spreading cortical depression. *Biophys J*, 23:257–276, 1978.

[58] James A Reggia and David Montgomery. A computational model of visual hallucinations in migraine. *Computers in biology and medicine*, 26(2):133–141, 1996.

[59] K. Revett, E. Ruppin, S. Goodall, and J.A. Reggia. Spreading depression in focal ischemia: A computational study. *J Cerebr Blood F Met*, 18(9):998–1007, 1998.

[60] A. C. G. Almeida, H. Z. Texeira, M. A. Duarte, and A. F. C. Infantosi. Modeling extracellular space electrodiffusion during Leão's spreading depression. *IEEE T Bio-med Eng*, 51(3):450–458, 2004.

[61] Hewerson Z. Teixeira, Antônio-Carlos G. Almeida, Antonio F. C. Infantosi, Michelle A. Vasconcelos, and Mário A. Duarte. Simulation of the effect of Na^+ and Cl^- on the velocity of a spreading depression wave using a simplified electrochemical model of synaptic terminals. *Journal of Neural Engineering*, 1:117–126, 2004.

[62] Antônio-Carlos G. Almeida, Antônio M. Rodrigues, Fúlvio A. Scorza, Esper A. Cavalheiro, Hewerson Z. Teixeira, Mário A. Duarte, Gilcélio A. Silveira, and Emerson Z. Arruda. Mechanistic hypotheses for nonsynaptic epileptiform activity induction and its transition from the interictal to ictal state – computational simulation. *Epilepsia*, 49(11):1908–1924, 2008.

[63] Max R. Bennett, Les Farnell, and William G. Gibson. A quantitative model of cortical spreading depression due to purinergic and gap-junction transmission in astrocyte networks. *Biophysical Journal*, 95:5648–5660, December 2008.

[64] Wei Yao, Huaxiong Huang, and Robert M. Miura. A continuum neuronal model for the instigation and propagation of cortical spreading depression. *B Math Biol*, 73:2773–2790, 2011.

[65] JC Chang, KC Brennan, D He, H Huang, RM Miura, PL Wilson, and JJ Wylie. A mathematical model of the metabolic and perfusion effects on cortical spreading depression. *PLoS One*, 8(8):e70469, August 2013.

[66] Bruce Edward Shapiro. *An electrophysiological model of gap-junction mediated cortical spreading depression including osmotic volume changes*. PhD thesis, UNIVERSITY OF CALIFORNIA Los Angeles, 2000.

[67] Bruce E. Shapiro. Osmotic forces and gap junctions in spreading depression: A computational model. *J Comput Neurosci*, 10:99–120, 2001.

[68] Yoichiro Mori. A multidomain model for ionic electrodiffusion and osmosis with an application to cortical spreading depression. *Physica D*, 308:94–108, 2015.

[69] James P Keener and James Sneyd. *Mathematical physiology*, volume 1. Springer, 1998.

[70] Jon Strieter, John L Stephenson, Lawrence G Palmer, and Alan M Weinstein. Volume-activated chloride permeability can mediate cell volume regulation in a mathematical model of a tight epithelium. *The Journal of general physiology*, 96(2):319–344, 1990.

[71] Peter J Basser. Interstitial pressure, volume, and flow during infusion into brain tissue. *Microvascular research*, 44(2):143–165, 1992.

[72] Bertil Hille et al. *Ion channels of excitable membranes*, volume 507. Sinauer Sunderland, MA, 2001.

[73] Charles Nicholson and Eva Syková. Extracellular space structure revealed by diffusion analysis. *Trends in neurosciences*, 21(5):207–215, 1998.

[74] Benjamin Steinberg, YQ Wang, Huaxiong Huang, and R Miura. Spatial buffering mechanism: Mathematical model and computer simulations. *Math. Biosci. Eng*, 2:675–702, 2005.

[75] Eric A Newman. Inward-rectifying potassium channels in retinal glial (Müller) cells. *The Journal of neuroscience*, 13(8):3333–3345, 1993.

[76] A. Lehmenkühler. Spreading depression-reaktionen an der hirnrinde: Störungen des extrazellulären mikromilieus. *EEG-EMG*, 21:1–6, 1990.

[77] F Richter and A. Lehmenkühler. Cortical spreading depression (csd): Ein neurophysiologisches korrelat der migräneaura. *Der Schmerz*, 22:544–550, 2008.

[78] O. Herreras, G. Somjen, and A. Strong. Electrical prodromals of spreading depression void grafstein's potassium hypothesis. *J Neurophysiol*, 94(5):3656–3657, 2005.

[79] Robert M. Dietz, John H. Weiss, and Claude W. Shuttleworth. Zn^{2+} influx is critical for some forms of spreading depression in brain slices influx is critical for some forms of spreading depression in brain slices. *J Neurosci*, 28(32):8014–8024, August 2008.

[80] N Cholet, L Pellerin, PJ Magistretti, and E Hamel. Similar perisynaptic glial localization for the Na^+, K^+-ATPase $\alpha 2$ subunit and the glutamate transporters GLAST and GLT-1 in the rat somatosensory cortex. *Cerebral Cortex*, 12(5):515–525, 2002.

Appendix A

Acronyms

We provide here a table of the acronyms used in this thesis.

Table A.1: Acronyms

Acronym	Meaning
ATP	Adenosine Triphospate
ADP	Adenosine Diphospate
DC Shift	Direct Current Shift (extracellular potential)
Na^+/K^+ ATPase	Sodium-Potassium Adenosine Triphosphatase
NMDA	N-methyl-D-aspartate
ODE	Ordinary Differential Equation
SD	Spreading Depression or Spreading Depolarization